iScience

CellPress

Article

The Body-wide Transcriptome Landscape of Disease Models

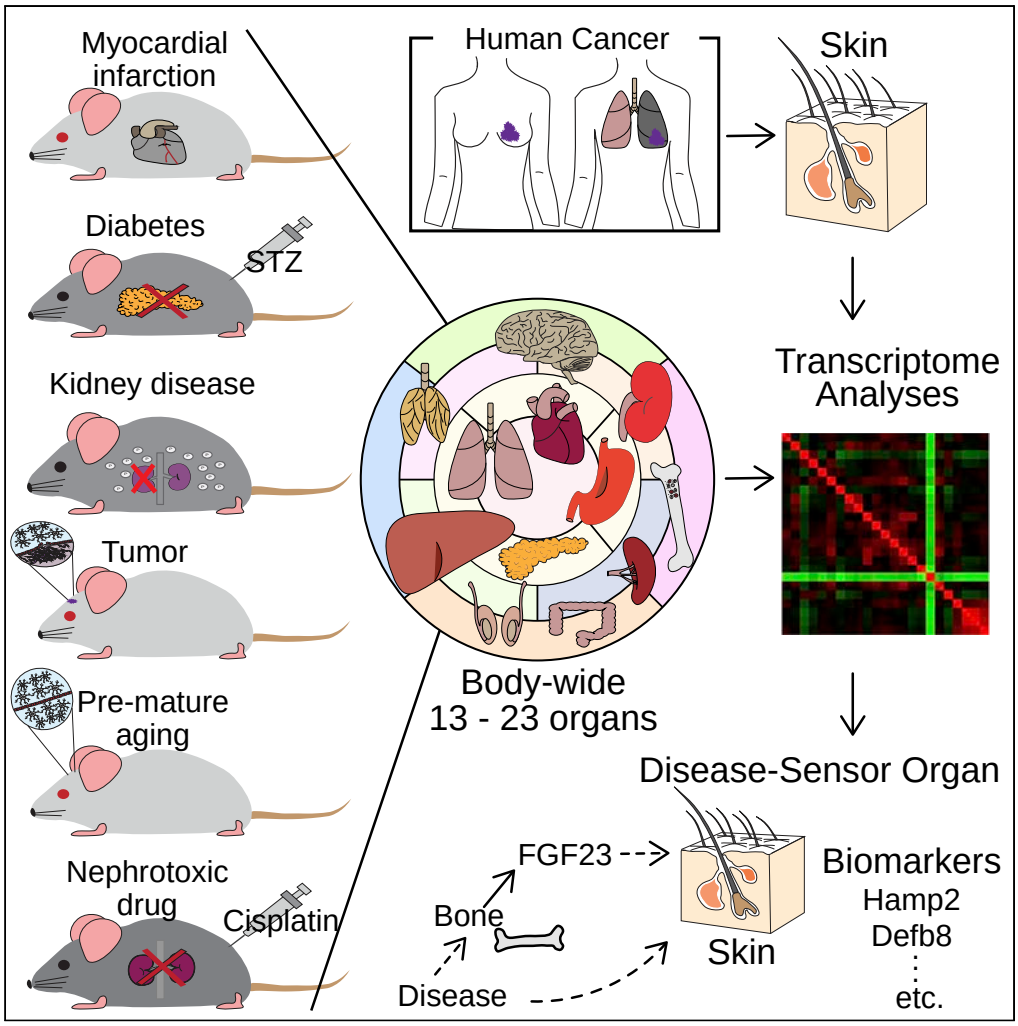

Satoshi Kozawa, Ryosuke Ueda, Kyoji Urayama, ..., Yoshinori Yamashita, Makoto Kuro-o, Thomas N. Sato

island1005@gmail.com

HIGHLIGHTS

Body-wide multi-organ transcriptome datasets encompassing diverse disease models

Skin is a disease-sensor organ, and FGF23 mediates a bone-skin cross talk in diseases

Diverse putative inter-organ cross talk selectively associates with diseases

A cross-species map illustrating the mouse-human relationships

Kozawa et al., iScience 2, 238–268
April 27, 2018
https://doi.org/10.1016/j.isci.2018.03.014

iScience

CellPress

Article

The Body-wide Transcriptome Landscape of Disease Models

Satoshi Kozawa,[1,2,10] Ryosuke Ueda,[1,2,10] Kyoji Urayama,[1,2,10] Fumihiko Sagawa,[1,2,3] Satsuki Endo,[1,2,3] Kazuhiro Shiizaki,[4] Hiroshi Kurosu,[4] Glicia Maria de Almeida,[3] Sharif M. Hasan,[3] Kiyokazu Nakazato,[3] Shinji Ozaki,[5] Yoshinori Yamashita,[6] Makoto Kuro-o,[4,7] and Thomas N. Sato[1,2,3,8,9,11,*]

SUMMARY

Virtually all diseases affect multiple organs. However, our knowledge of the body-wide effects remains limited. Here, we report the body-wide transcriptome landscape across 13–23 organs of mouse models of myocardial infarction, diabetes, kidney diseases, cancer, and pre-mature aging. Using such datasets, we find (1) differential gene expression in diverse organs across all models; (2) skin as a disease-sensor organ represented by disease-specific activities of putative gene-expression network; (3) a bone-skin cross talk mediated by a bone-derived hormone, FGF23, in response to dysregulated phosphate homeostasis, a known risk-factor for kidney diseases; (4) candidates for the signature activities of many more putative inter-organ cross talk for diseases; and (5) a cross-species map illustrating organ-to-organ and model-to-disease relationships between human and mouse. These findings demonstrate the usefulness and the potential of such body-wide datasets encompassing mouse models of diverse disease types as a resource in biological and medical sciences. Furthermore, the findings described herein could be exploited for designing disease diagnosis and treatment.

INTRODUCTION

Diseases are conventionally studied in the context of changes and responses that occur in only one or a few selected organs. For example, in studying heart diseases, the heart is the main focus point. In some cases, a few other organs (e.g., kidney, lung, brain) are included in the studies, as they are known to interact with the heart via circulating hormones and other systemic factors (McGrath et al., 2005). In investigating kidney diseases, multiple organs (e.g., bone, heart, brain, liver) are often studied on the basis of the inter-organ communication (Hu et al., 2013; Ix and Sharma, 2010; Kuro-o, 2010; Vervloet et al., 2014a). Tumorigenesis in a specific organ imposes critical impacts on metabolic organs, eventually causing the whole-body-level condition known as cachexia (Droujinine and Perrimon, 2016). Even in this case, only a few selected organs are the subjects of the studies. Currently, we know very little about exactly to what extent diverse organs in the body are influenced in a specific disease condition.

In an effort to understand the whole-body level biology of the human and non-human model organisms, the multi-organ omics databases have been established and made available to the public. Especially, the Genotype-Tissue Expression (GTEx) (GTEx Consortium, 2013) and The Human Protein Atlas (Uhlen et al., 2015) publish comprehensive transcriptome and transcriptome/proteome datasets of multiple organs of healthy human subjects, respectively. Most recently, an international research project referred to as Human Cell Atlas (Regev et al., 2017) has been initiated and is aiming to have the complete whole-body map of the human at the individual cell level. A similar approach has already generated transcriptome datasets of approximately 6,000 individual cells in Drosophila (Karaiskos et al., 2017), a commonly used model organism in biology and medicine. Recently, we reported comprehensive whole-body transcriptome datasets of normal and several mutant zebrafish (Takada et al., 2017), a vertebrate model frequently used for the study of biology and medicine. Although such comprehensive multi-organ datasets of healthy subjects and developmental models are being generated, comparably comprehensive multi-organ and multi-disease datasets remain limited. The Stockholm-Tartu Atherosclerosis Reverse Network Engineering Task (STARNET) has provided transcriptome datasets of several organs derived from human subjects with coronary artery diseases (CADs) (Franzen et al., 2016). However, diverse organs are yet to be represented. Furthermore, the comparable datasets for other types of diseases are not available, thus disease-to-disease comparisons remain a challenge.

[1]The Thomas N. Sato BioMEC-X Laboratories, Advanced Telecommunications Research Institute International (ATR), 2-2-2 Hikaridai, Seika-cho, Soraku-gun, Kyoto 619-0288, Japan

[2]ERATO Sato Live Bio-Forecasting Project, Japan Science and Technology Agency (JST), Kyoto 619-0288, Japan

[3]Karydo TherapeutiX, Inc., Tokyo 102-0082, Japan

[4]Division of Anti-aging Medicine, Center for Molecular Medicine, Jichi Medical University, Tochigi 329-0498, Japan

[5]Department of Breast Surgery, Kure Medical Center and Chugoku Cancer Center, Hiroshima 737-0023, Japan

[6]Institute for Clinical Research and Department of Chest Surgery, Kure Medical Center and Chugoku Cancer Center, Hiroshima 737-0023, Japan

[7]AMED-CREST, Japan Agency for Medical Research and Development, Tokyo 100-0004, Japan

[8]Department of Biomedical Engineering, Cornell University, Ithaca, NY 14853, USA

[9]Centenary Institute, Newtown, NSW 2042, Australia

[10]These authors contributed equally

[11]Lead Contact

*Correspondence: island1005@gmail.com

https://doi.org/10.1016/j.isci.2018.03.014

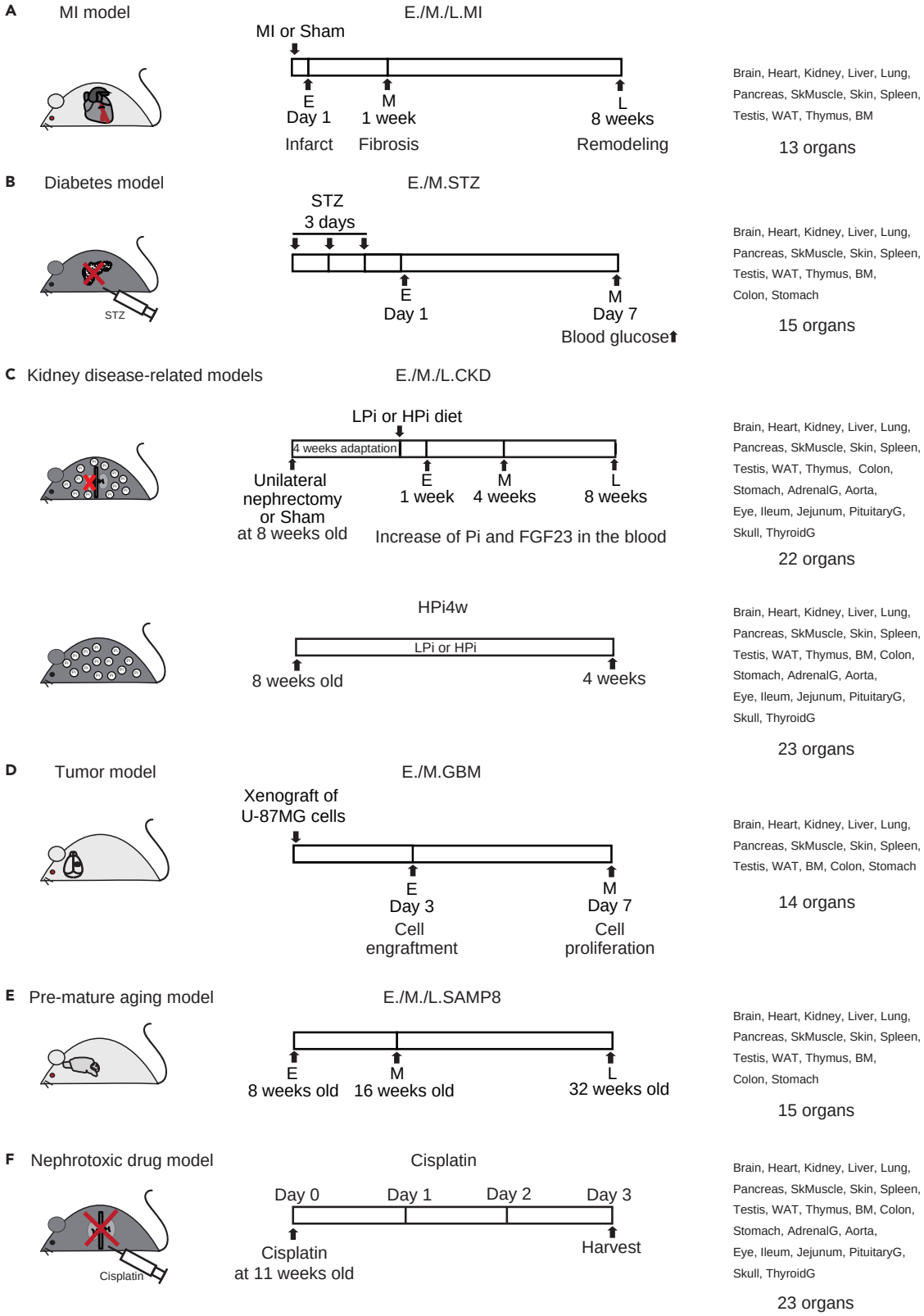

Figure 1. Mouse Models

Each model and the organs analyzed are described (See Transparent Methods for the details).

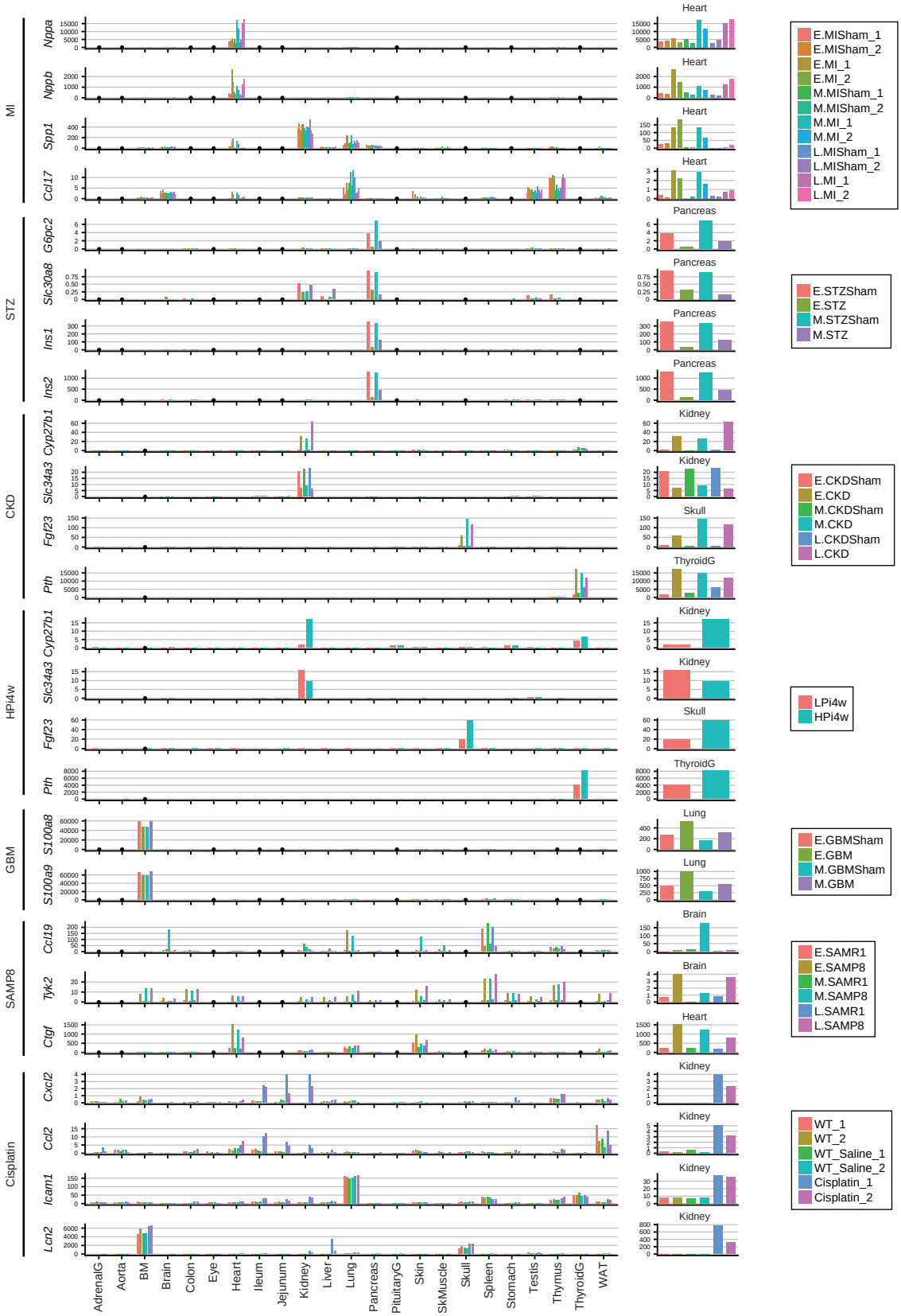
MI
Nppa
Nppb
Spp1
Ccl17
STZ
G6pc2
Slc30a8
Ins1
Ins2
CKD
Cyp27b1
Slc34a3
Fgf23
Pth
HPi4w
Cyp27b1
Slc34a3
Fgf23
Pth
GBM
S100a8
S100a9
SAMP8
Ccl19
Tyk2
Ctgf
Cisplatin
Cxcl2
Ccl2
Icam1
Lcn2
Heart
Pancreas
Kidney
Skull
ThyroidG
Lung
Brain
AdrenalG
Aorta
BM
Brain
Colon
Eye
Heart
Ileum
Jejunum
Kidney
Liver
Lung
Pancreas
PituitaryG
Skin
SkMuscle
Skull
Spleen
Stomach
Testis
Thymus
ThyroidG
WAT
E.MISham_1
E.MISham_2
E.MI_1
E.MI_2
M.MISham_1
M.MISham_2
M.MI_1
M.MI_2
L.MISham_1
L.MISham_2
L.MI_1
L.MI_2
E.STZSham
E.STZ
M.STZSham
M.STZ
E.CKDSham
E.CKD
M.CKDSham
M.CKD
L.CKDSham
L.CKD
LPi4w
HPi4w
E.GBMSham
E.GBM
M.GBMSham
M.GBM
E.SAMR1
E.SAMP8
M.SAMR1
M.SAMP8
L.SAMR1
L.SAMP8
WT_1
WT_2
WT_Saline_1
WT_Saline_2
Cisplatin_1
Cisplatin_2

Figure 2. Differential Expression of Known Regulated Genes in Each Model

FPKM (fragments per kilobase million) of each gene in each organ sample is plotted as bar graph. All organs (left) and the select organs known for the regulated expression of the genes (right) are shown. The model names are according to those shown in Figure 1. The gene name is indicated on the left of each graph. The organs for which the sequence datasets are not available for each model are indicated as ● on the x axis of each graph.

Hence, what is missing is the dataset representing the body-wide diverse organs and multiple diseases. The availability of such datasets allows for the evaluations of molecular changes that occur in diverse organs in each disease model. Such datasets also make it possible to perform direct organ-to-organ comparisons among various disease models and also inter-organ comparisons within the specific model. Such analyses can be effectively used to deduce the body-wide inter-organ communication network. Furthermore, their utility could extend to the identification of disease-specific and/or organ-specific molecular signatures that could serve as biomarkers for diseases and/or molecular targets for therapeutics. Moreover, such body-wide multi-disease model datasets could be used to make organ-to-organ comparisons with human datasets to characterize similarities and dissimilarities between the mouse and human transcriptome landscapes.

In this report, we provide such datasets. We describe comprehensive transcriptome datasets of 13–23 organs from diverse disease models: myocardial infarction, diabetes, kidney diseases, brain tumor, and pre-mature aging. The data are generated from one to three stages representing early to late phases of the progression of each disease condition. For kidney diseases, we provide datasets from multiple different models, each representing overlapping but distinct risk factors for the disease. The analyses of such datasets reveal organ-to-organ similarities and dissimilarities among different disease models. They also show common and distinct features of the transcriptome landscape among distinct organs within each model. These analyses identified the skin as one of the unexpected organs that appears to sense disease-associated pathophysiological condition(s). Experimental validations found 25 genes in the skin that are differentially expressed in the kidney-disease models. We also show that their expression is differentially modulated by a bone-derived systemic factor, FGF23, suggesting a bone-skin interaction in kidney disease or related conditions. More global body-wide network analyses across multiple organs in each model identify candidates for inter-organ cross talk underlying disease-associated pathophysiological changes. The utility of our mouse model datasets is also illustrated by showing the organ-to-organ differences in the degree of similarity in the genome-wide gene expression patterns between human and each mouse model. The comparison of the mouse datasets to an orthologous human disease dataset provides an insight into the degree of the relatedness of the mouse model to human disease. We discuss the utility of such rich body-wide datasets across multiple disease models for the study of disease and also the relevance of the findings to human biology and clinical applications.

RESULTS

Mouse Models of Human Diseases

Comprehensive transcriptome data were generated from mouse models of diverse human diseases and disease-related conditions (Figure 1). We chose seven relatively well-established and widely used mouse models and generated transcriptome datasets from one to three pathophysiological stages for each model (Figure 1). Models for myocardial infarction (MI) (Murakoshi et al., 2013) (Figure 1A), streptozotocin (STZ)-induced diabetes (Graham et al., 2011; Portha et al., 1989) (Figure 1B), kidney diseases and related conditions including chronic kidney disease (CKD), chronic kidney disease mineral and bone disorder (CKD-MBD) (Hu et al., 2013; John et al., 2011; Kuro-o, 2013, 2017; Kuro-o and Moe, 2017; Kuro-o, 2010; Miller et al., 2010; Stubbs et al., 2007; Tani et al., 2017; Watanabe et al., 2017) (Figure 1C), cancer (Kiaris et al., 2000) (Figure 1D), pre-mature aging (Butterfield and Poon, 2005) (Figure 1E), and kidney injury induced by cisplatin (Megyesi et al., 1998) (Figure 1F) were generated (see Transparent Methods) and validated (Figures S1–S5, Tables S1–S9).

Comparative Analyses of the Mouse RNA-Sequence Datasets

From each model and control mice (WT and WT + Saline) (see Transparent Methods), 13–23 organs were harvested and processed for RNA sequence (RNAseq) analyses (see Transparent Methods). The overall quality of the sequence data was demonstrated by the virtually identical gene expression patterns between the control datasets (WT and WT + Saline) and the publicly available wild-type (WT) mouse datasets (Pervouchine et al., 2015) (Figure S6). A subtle difference could be attributed to strain, age, sex, or housing-condition differences (see Transparent Methods). The validity of the datasets was further confirmed

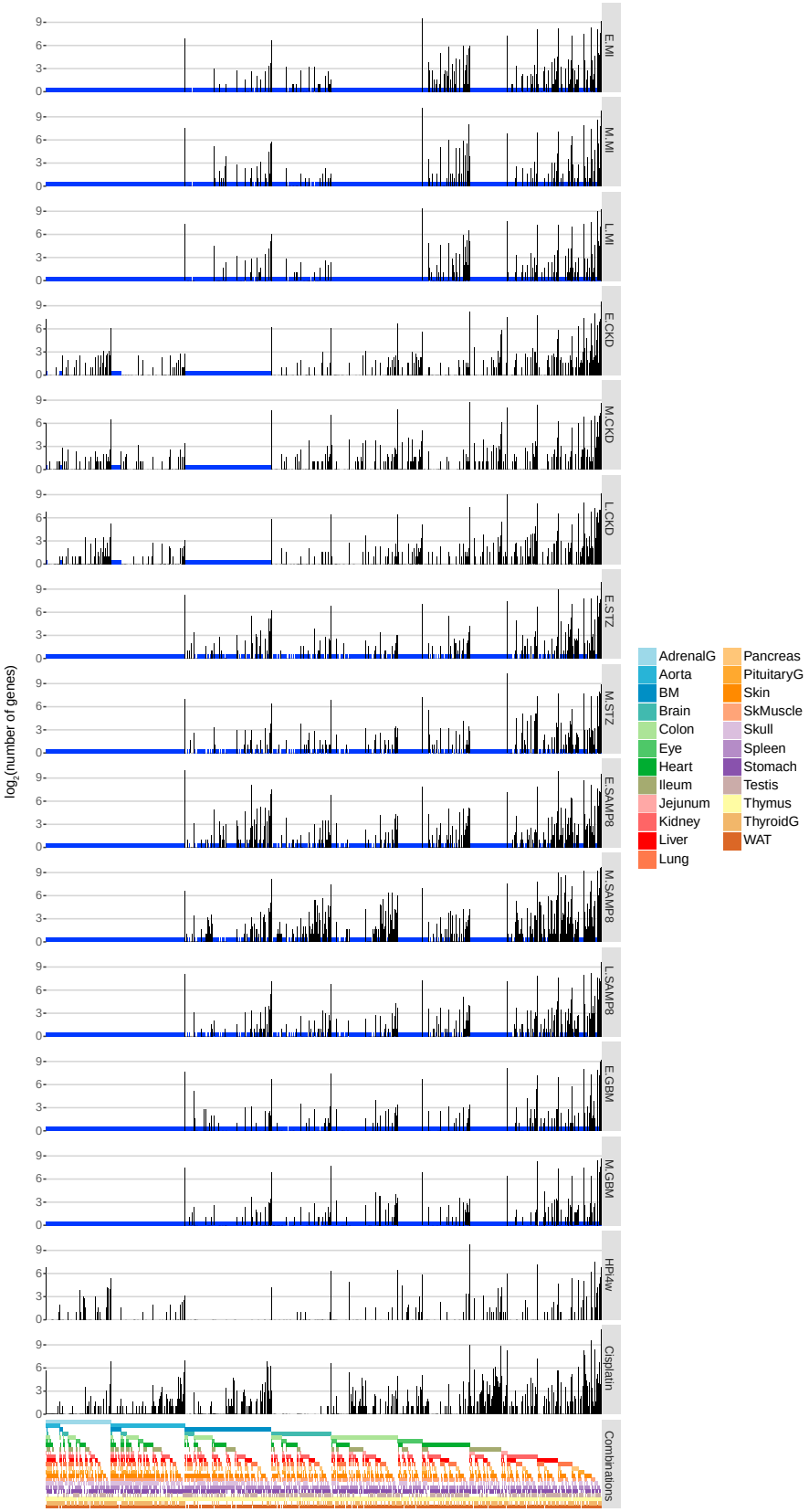
log2(number of genes)
E.MI
M.MI
L.MI
E.CKD
M.CKD
L.CKD
E.STZ
M.STZ
E.SAMP8
M.SAMP8
L.SAMP8
E.GBM
M.GBM
HP4w
Cisplatin
Combinations
AdrenalG
Aorta
BM
Brain
Colon
Eye
Heart
Ileum
Jejunum
Kidney
Liver
Lung
Pancreas
PituitaryG
Skin
SkMuscle
Skull
Spleen
Stomach
Testis
Thymus
ThyroidG
WAT

Figure 3. Organ-to-Organ Comparisons of the Differentially Expressed Genes for Each Model

The color or the colors (the vertical alignment) at the bottom indicate the organ or the combination of the organs, respectively. The differentially expressed genes in each organ/organ combination of each model were identified by comparison with the corresponding dataset of WT. The number (in $\log_2$) of the differentially expressed genes in each organ/organ combination of each disease model, but not in that of the corresponding sham control, was counted and is shown as bar graph for each model. The number (in $\log_2$) of the differentially expressed genes in each organ/organ combination of the cisplatin model, as compared with the corresponding dataset of WT, was counted and is shown as bar graph. It is important to note that the organs analyzed for each model overlap but are not identical (see Figure 1). The organs that are not represented in each model are indicated by blue-color x axis line. Thus the comparison is valid only among the organs that are represented in each organ. The corresponding organ-to-organ comparisons of the GO terms are shown in Figure S7.

by the regulated expressions of the known disease marker genes (Bosworth and de Boer, 2013; Cheng et al., 2015; Hiratsuka et al., 2006; Jarve et al., 2017; Pabla et al., 2015; Port et al., 2011; Ramesh and Reeves, 2002; Reed et al., 2011; Sehl et al., 2000; Suyama et al., 2012; Tonne et al., 2013; Wada et al., 2016) (Figure 2). To evaluate how broadly the gene expressions are altered across various organs, we compared both model and sham control with WT control datasets independently using DESeq2 analysis. For convenience, we used 2-fold change as differentially expressed genes (i.e., $|\log_2(\text{fold-change})| > 1$) with $p < 0.0001$ (Wald test and adjusted by Benjamini-Hochberg method). The number of such differentially expressed genes specifically for one organ in each model, but not in the corresponding sham control, was counted. In addition, the number of the differentially expressed genes in multiple organs for all combinations of the organs in each model, but not in the corresponding sham control, was also counted. The results of such organ-to-organ comparisons for each model are shown in Figure 3. It is important to note that the organs analyzed for each model overlap but are not identical; thus the model-to-model comparison should not be performed using these graphs. Hence, for the model-to-model comparison for each organ, the number of differentially expressed genes in each organ isolated from each model was analyzed (Figure 4). The number of differentially expressed genes specifically in one model or sham control, but not in the other models or sham controls, and also in multiple combinations of the models/sham controls, but not in other combinations was counted. The results of such model-to-model comparisons for each organ are shown in Figure 4.

As expected, the organ(s) that is(are) conventionally known to show pathophysiological responses in each model show a large number of differentially expressed genes. In the MI models, the clusters of taller bars in the heart and the combinations including the heart are obvious (Figure 3). A closer examination found 1,302, 1,891, and 1,178 differentially expressed genes in the heart or the organ combinations, including the heart of E-MI, M-MI, and L-MI, respectively, but not in the corresponding sham-control models (Tables S10 and S11). Furthermore, according to the ranking in the number of differentially expressed genes in the heart, the M-MI model is the first with 629 genes (Figure 4 and Table S12). The second is E−/M-MI models with 261 genes (i.e., 261 genes are differentially expressed in both E− and M-MI models) (Figure 4 and Table S12). The third (253 genes), fourth (133 genes), fifth (105 genes), and sixth (102 genes) were E-MI model, M-/L-MI models, E−/M-/L-MI models, and L-MI model, respectively (Figure 4 and Table S12). The genes that are also regulated in the corresponding sham controls were excluded in this ranking (Figure 4 and Table S12). In the kidney disease models, we found 499, 631, and 1,124 differentially expressed genes in the kidney or the organ combinations, including the kidney of E-CKD, M-CKD, and L-CKD, respectively, but not in the corresponding sham-control models (Figure 3, Tables S10 and S11). In the cisplatin-treated model, the kidney shows 1,482 differentially expressed genes (Figure 3, Tables S10 and S11).

However, the overall landscape of the organ-to-organ and the model-to-model comparisons was more complex than anticipated. It appears that the differential gene expression patterns extend to more diverse organ types than conventionally assumed (Figure 3). Although, in each model, the number of differentially expressed genes varies from organ to organ and also depends on the organ combinations, the differentially expressed genes are broadly distributed across organs and organ combinations (Figure 3). The organ-to-organ comparisons of Gene Ontology (GO) terms of the differentially expressed genes also show the overlapping and distinct distribution pattern for each organ (Figure S7 and Table S13). In the model-to-model comparisons (Figure 4), the differentially expressed genes in each organ can be detected both in a specific model and also are shared among multiple organs, as indicated by the broadly distributed patterns of the bars in each graph (Figure 4). A closer examination also identifies the lack of differentially expressed genes in a certain model(s) and/or a model combination(s), as indicated by the lack of the bars (Figure 4). A common distribution pattern can also be found among the organs, suggesting the possibility that some organs

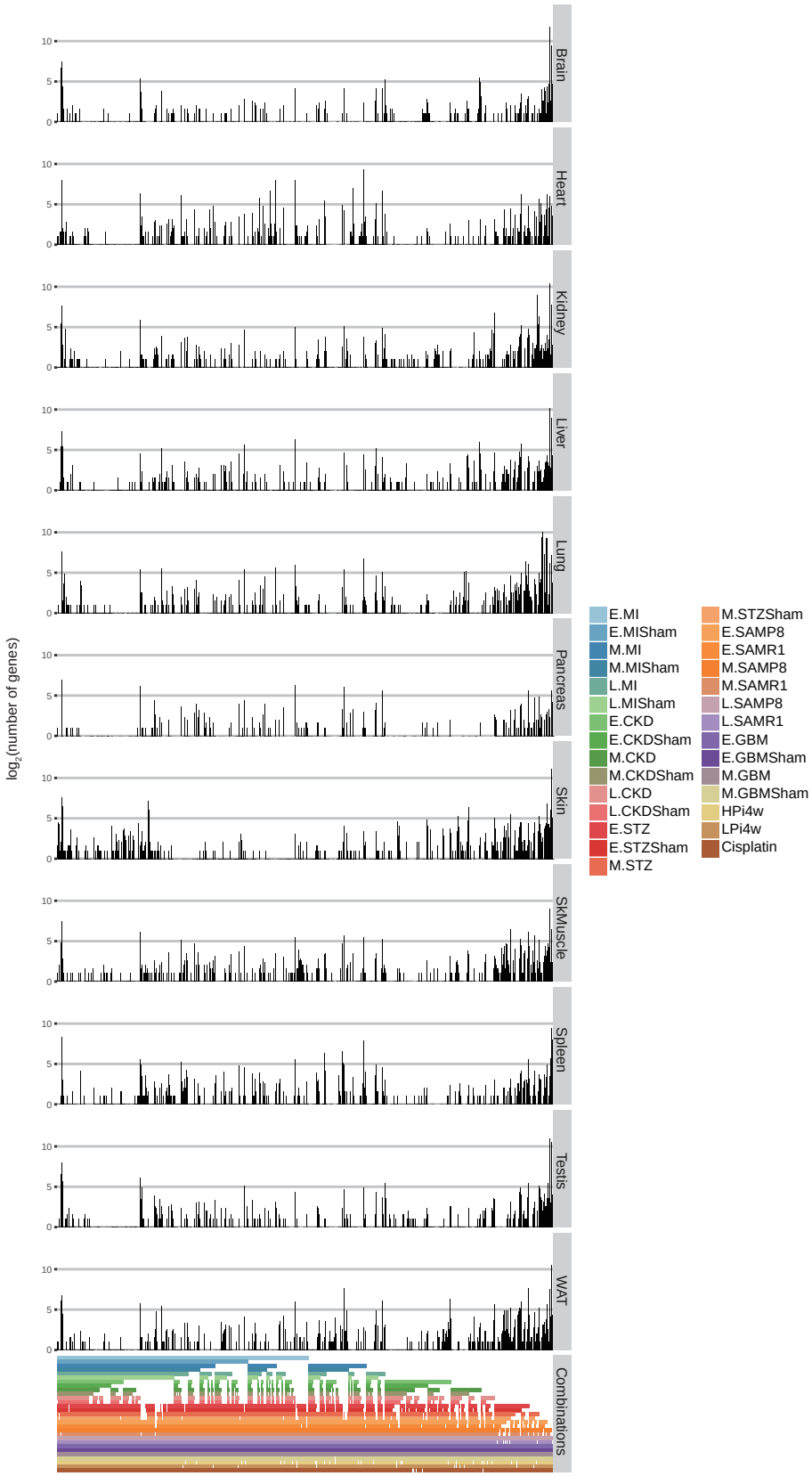
Brain
Heart
Kidney
Liver
Lung
Pancreas
Skin
SkMuscle
Spleen
Testis
WAT
Combinations
log2(number of genes)
10
5
0
E.MI
E.MISham
M.MI
M.MISham
L.MI
L.MISham
E.CKD
E.CKDSham
M.CKD
M.CKDSham
L.CKD
L.CKDSham
E.STZ
E.STZSham
M.STZ
M.STZSham
E.SAMP8
E.SAMR1
M.SAMP8
M.SAMR1
L.SAMP8
L.SAMR1
E.GBM
E.GBMSham
M.GBM
M.GBMSham
HPi4w
LPi4w
Cisplatin

Figure 4. Model-to-Model Comparisons of the Gene Expression for Each Organ

The color or the colors (the vertical alignment) at the bottom indicate the model or the model combinations, respectively. The number (in $\log_2$) of the differentially expressed genes (as compared with the corresponding WT dataset) in each model/model combination of each organ was counted and is shown as bar graph for each model. Only organs that are common to all models are analyzed and shown. The model-to-model comparisons of the GO terms are shown in Figure S8.

respond more robustly than the others (Figure 4). The model-to-model comparisons of GO terms of the differentially expressed genes in each organ also show both the model/model-combination-specific GO terms and those shared by multiple models/model combinations (Figure S8 and Table S13).

The Skin as a Disease Sensor?

We show that differential gene expression can be found broadly across diverse organs (Figure 3). In particular, the skin is one of the most robustly affected organs (Figure 3, Tables S10 and S11). In each model, but not in the corresponding sham control, a large number of genes are differentially expressed in the skin: 337 (E-MI), 378 (M-MI), 248 (L-MI), 477 (E-CKD), 294 (M-CKD), 707 (L-CKD), 361 (E-STZ), 349 (M-STZ), 974 (E-SAMP8), 3,731 (M-SAMP8), 526 (L-SAMP8), 381 (E-GBM), 267 (M-GBM), 79 (HPi4w), 2,011 (Cisplatin) genes (Figure 3, Tables S10 and S11). The model-specific differentially expressed skin genes were also found: 8 (E-MI), 10 (M-MI), 2 (L-MI), 13 (E-CKD), 6 (M-CKD), 28 (L-CKD), 21 (E-STZ), 38 (M-STZ), 110 (E-SAMP8), 2,160 (M-SAMP8), 33 (L-SAMP8), 5 (E-GBM), 25 (M-GBM), 6 (HPi4w), 536 (Cisplatin) genes (Figure 4 and Table S12).

Next, we applied Weighted Gene Co-expression Network Analysis (WGCNA) to identify signature gene expression network activities of the skin that distinguish one pathophysiological condition from the other (Figure 5 and see Transparent Methods). For each model, we found a set of modules consisting of unique GO terms that show relatively stronger positive or negative correlation with a specific pathophysiological condition (e.g., E., M., L.) than with the others (Figure 5 and Table S14).

The WGCNA of the skin of the MI models identified the modules that show relatively strong negative correlations with E.MI or L.MI. The former module consists of GO terms such as "regulation of viral life cycle" and "viral budding" (Figure 5A and Table S14), suggesting that the downregulation of these processes signifies the skin condition of E.MI. The latter module consists of GO terms such as "modulation by virus of host morphology or physiology," "circulatory system," and "vascular development" (Figure 5A and Table S14), suggesting that the suppression of these processes may represent the skin condition of L.MI.

The analysis of the skin of the STZ-induced diabetes model identified one module that shows a strong negative correlation with E.STZ and the other module that exhibits a strong positive correlation with M.STZ (Figure 5B and Table S14). The former consists of GO terms such as "positive regulation of cellular process" and "positive regulation of signal transduction" (Figure 5B and Table S14), suggesting that the downregulation of these processes represents the skin condition of E.STZ. The latter module consists of GO terms such as "positive regulation of type I interferon-mediated signaling pathway" and "cellular response to type I interferon" (Figure 5B and Table S14), suggesting that the enhanced activities of such processes may signify the skin condition of M.STZ.

The WGCNA of the skin of the CKD models found the modules that distinguish L.CKD from the others, and they consist of unique GO terms such as "intracellular protein transport," "response to wounding," "single-organism cellular processes," and "muscle structure development" (Figure 5C and Table S14), suggesting that the upregulation of such processes in the skin represents L.CKD-specific pathophysiological conditions.

The inclusion of the phosphorus-overload models to the CKD models in the analysis resulted in the modular pattern where no modules show outstandingly strong correlations with any models (Figure 5D). This result suggests that the skin conditions of these models are relatively similar.

A comparison of the cisplatin model with the CKD and phosphorus-overload models identified positively and negatively correlating modules with the cisplatin model (Figure 5E and Table S14). The positively

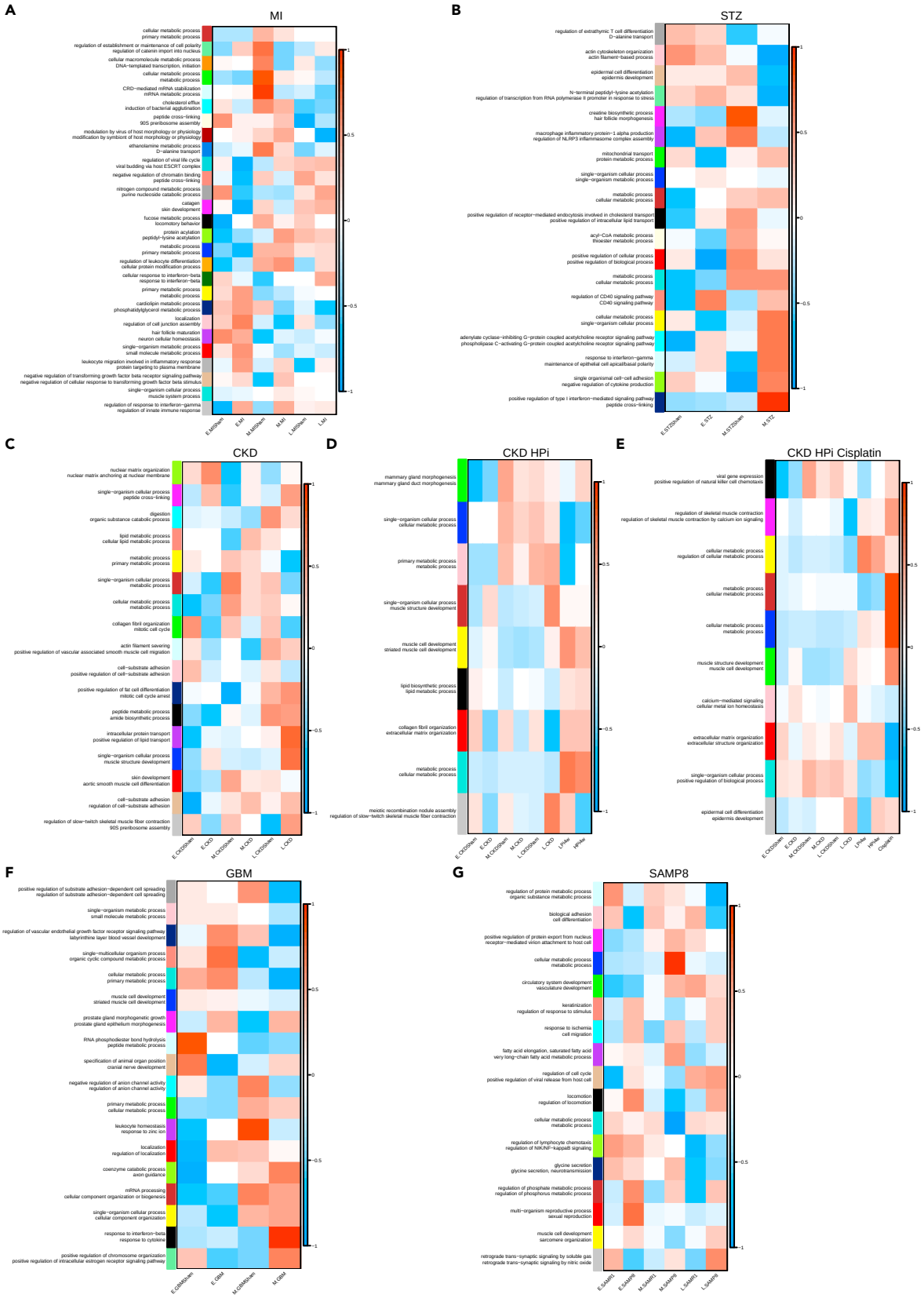
A
MI
B
STZ
C
CKD
D
CKD HPi
E
CKD HPi Cisplatin
F
GBM
G
SAMP8

Figure 5. Signature Gene Expression Network Activities of the Skin

The result of WGCNA using the skin datasets of the MI models (A), the STZ-induced diabetes models (B), the CKD models (C), the CKD and phosphorus-overload models (D), the CKD, the phosphorus-overload, and the cisplatin-induced kidney injury models (E), the tumor models (F), and the pre-mature aging models (G) are shown (see Transparent Methods). The top two GO terms are shown for each module on the left. The correlation coefficient and the p value (Student's asymptotic t test) of each module and the complete list of GO terms with their p values (Fisher's exact test) are shown in Table S14.

correlating modules consist of GO terms such as "metabolic process" and "catabolic process" (Figure 5E and Table S14). The negatively correlating module consists of GO terms such as "extracellular matrix organization," "collagen fibril organization," and "lipid metabolic process" (Figure 5E and Table S14), suggesting that the downregulation of such processes in the skin represents the cisplatin-model-specific condition.

The analysis of the tumor model identified a module that shows strong correlation with M.GBM (Figure 5F). The module consists of GO terms such as "response to interferon-beta" and "response to cytokine" (Figure 5F and Table S14), suggesting that the upregulation of such processes signifies the skin condition of M.GBM but not of E.GBM.

The WGCNA of the pre-mature aging models identified several modules that distinguish one pathophysiological condition from the other (Figure 5G). The modules consisting of GO terms such as "cellular metabolic process" and "organic substance metabolic process". appear to distinguish M.SAMP8 from the others (Figure 5G and Table S14). The module consisting of GO terms such as "regulation of protein metabolic process," "organic substance metabolic process," and "leukocyte migration involved in inflammatory response" shows a strong negative correlation specifically with L.SAMP8 (Figure 5G and Table S14), suggesting that the downregulation of such processes distinguish the L.SAMP8 skin condition from the others.

These and other modules showing relatively stronger correlations and lower p values could be signature activities of the gene expression network in the skin for that specific pathophysiological condition in the model. These results are also in support of the idea that the skin is a disease-sensor organ.

Although a variety of skin pathophysiological conditions are implicated for a variety of non-skin diseases (Brewster, 2008; Duff et al., 2015; Gagnon and Desai, 2013; Gnirs and Prelaud, 2005; Uliasz and Lebwohl, 2008), the evidence remains relatively weak. Furthermore, the molecular mechanism underlying such skin pathologies and/or conditions remains elusive. Our results with the mouse models suggest the existence of unique signature activities of gene expression network in the skin that represent a specific pathophysiological condition of each disease model, providing molecular and system level evidence for the skin as a disease-sensor organ. In fact, such findings are not limited to the mouse models. We performed RNAseq analyses of skin biopsies from eight patients with breast cancer and three patients with lung cancer (Figure 6). These analyses demonstrate that gene expression changes occur in the skin in non-skin diseases such as breast and lung cancer in human (Figure 6). Furthermore, there exist gene expression changes that are conserved and specific to each cancer type and that are common for both (Figure 6).

To further investigate the regulatory mechanisms underlying the gene expression changes in the skin in non-skin diseases, we studied the differential gene expression changes in the skin in our mouse models (Figures 3, 4, and 5). Several pathophysiological skin conditions are observed in renal diseases in human. However, very little is known about the molecular signatures of such skin conditions. Furthermore, the molecular mechanism underlying the emergence of such skin conditions in renal diseases remains enigmatic. Hence, we characterized the gene expression changes found in the models of kidney diseases.

We selected 25 differentially expressed genes in the skin of E-CKD, M-CKD, and L-CKD models, and unilateral nephrectomy followed by phosphate overload was imposed on the mice. The qRT-PCR analysis validated the varying degrees of up- and down-regulation in one or more of the CKD models: 14 were upregulated (Figure 7A and Table S15) and 11 were downregulated (Figure 7B and Table S15).

The Bone-Skin Cross talk and FGF23

Next, we designed an experiment to gain a mechanistic insight into the differential expression of the genes. We hypothesized that a systemic factor derived from a non-skin organ(s) mediates such differential

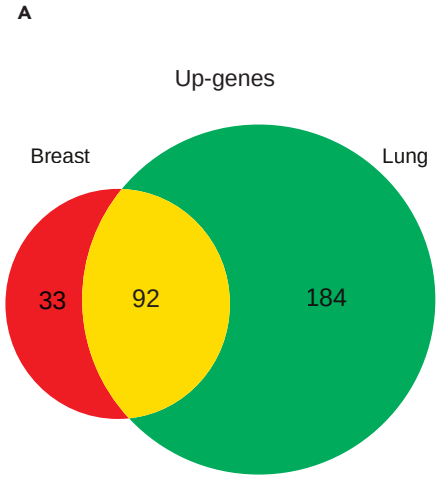
A
Up-genes
Breast
Lung
33
92
184

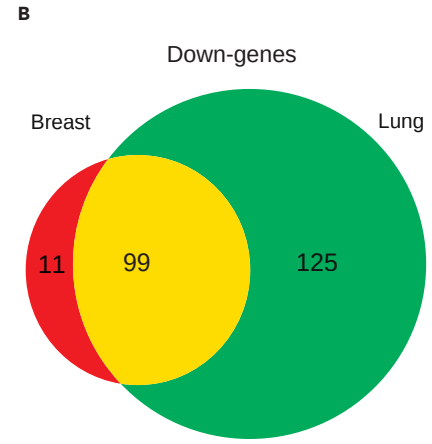
B
Down-genes
Breast
Lung
11
99
125

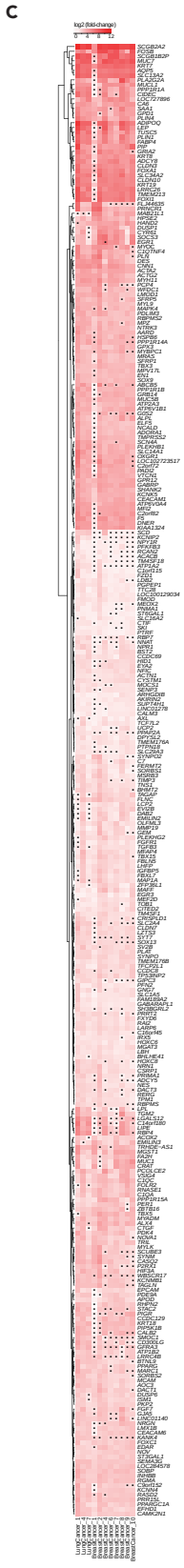
C

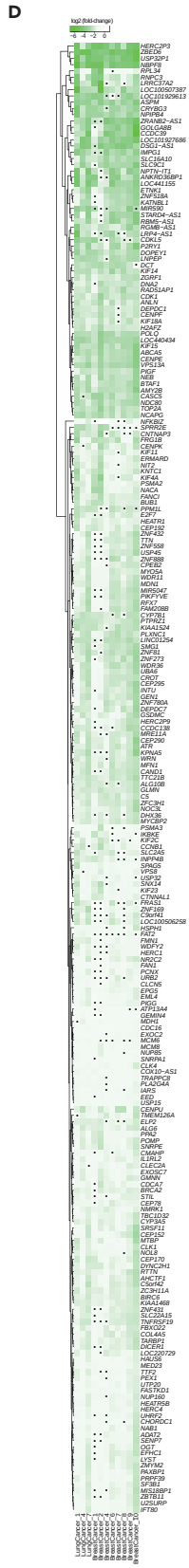
D

Figure 6. Comparison of the Gene Expression Patterns in the Skin Derived from Patients with Cancer

The number of upregulated (Up-genes) (A) and downregulated (Down-genes) (B) genes is indicated in the Venn diagram. The differential expression levels of the upregulated (C) and downregulated (D) genes are shown in the heatmap. Those that are non-significant as defined by $p \geq 0.0001$ are indicated by ■.

gene expression in the skin of CKD models. FGF23 could be a candidate. FGF23 is a bone-derived hormone that regulates phosphate homeostasis and is implicated in kidney diseases (Bergwitz and Juppner, 2010; Blau and Collins, 2015; Guo and Yuan, 2015; Hu et al., 2013; Kuro-o, 2013, 2017; Kuro-o and Moe, 2017; Kuro-o, 2010; Mitsnefes et al., 2017; Portale et al., 2014; Portale et al., 2016; Shimada et al., 2004; Stubbs et al., 2007; Vervloet et al., 2014b; Wesseling-Perry and Salusky, 2013). In fact, we show that the level of the circulating FGF23 is significantly increased in the CKD models (Figure S3C). Therefore, we tested this hypothesis by characterizing FGF23-deficient mice (Figure S9A). FGF23-deficient mice were generated by the CRISPR/Cas9 method (Figure S9A and see Transparent Methods). As FGF23-deficient mice progressively weaken postnatally (Shimada et al., 2004; Stubbs et al., 2007), we developed another phosphate-overload model using mice 3–4 weeks old. WT mice 3 weeks old (they are weaned at 3 weeks old) were fed *ad libitum* with a diet containing low (0.35%), normal (0.54%), or high (2%) levels of inorganic phosphate for 1 week (see Transparent Methods for the details). In this model, both the plasma phosphate (Figure S9B) and FGF23 (Figure S9C) levels increase in the WT mice. FGF23-deficient (FGF23KO) mice at 3 weeks and 1 day old (they are weaned at 3 weeks old) were also fed with the diet containing normal (0.54%) or high (2%) levels of inorganic phosphate for 1 week (see Transparent Methods for the details). In these FGF23KO mice, the plasma FGF23 is barely detectable, confirming the null mutation of the gene (Figure S9C). Furthermore, the plasma phosphate level increases even without the phosphate overload (Figure S9B), corroborating the known function of FGF23 as a hormone facilitating phosphate excretion (Bergwitz and Juppner, 2010; Kuro-o, 2013; Kuro-o, 2010; Stubbs et al., 2007). The FGF23KO mice show the increased plasma phosphate level upon the phosphate overload (FGF23KO1WHP in Figure S9B), confirming that they indeed take in the high-phosphate diet. The expressions of the 25 skin genes were analyzed by qRT-PCR in this model (Figure 8). The expression of each gene in the younger mice loaded with a high-phosphate diet for 1 week (WT1WHP) was compared with that with a low-phosphate diet (WT1WLP). The result showed 5 upregulated (*Hamp2*: ca. x3.6, *Cxcl13*: ca. x2.3, *Ptp4a3*: ca. x1.3, *Serpinb6e*: ca. x2.0, *Il22ra2*: ca. x1.6) (Figure 8A and Table S16) and 10 downregulated genes (*Col15a1*: ca. x0.7, *Aldh1l2*: ca. x0.3, *Clec11a*: ca. x0.3, *Serpinb6d*: ca. x0.3, *Defb8*: ca. x0.01, *Col3a1*: ca. x0.5, *C1qtnf6*: ca. x0.4, *Sparc*: ca. x0.5, *Col1a1*: ca. x0.4, *Col5a1*: ca. x0.6) (Figures 8B, 8D, and Table S16). The expression of Nrap also appears to be downregulated (ca. x0.8), but the p value was only 0.01074 (Figure 8C and Table S16). The expressions of nine genes (*Actn3*, *Asb11*, *Klhl38*, *Atp2a1*, *Myot*, *Pde4dip*, *Rbfox1*, *Lrrc2*, *Col11a1*) show no significant changes (Figure 8C and Table S16).

Next, the effect of FGF23 deficiency was examined using the FGF23-deficient mice (Figure 8). The comparisons were made as follows: WT with the normal diet (WT1WND) vs. FGF23KO with the normal diet (FGF23KO1WND), WT with the high-phosphate diet (WT1WHP) vs. FGF23KO with the high-phosphate diet (FGF23KO1WHP), and WT with the high-phosphate diet (WT1WHP) vs. FGF23KO with the normal-phosphate diet (FGF23KO1WND). The plasma phosphate level in the WT mice fed with the high phosphate shows an increase in the blood phosphate level that is comparable with that of the FGF23KO mice fed with the normal diet (Figure S9B). Therefore, the comparison between WT1WHP and FGF23KO1WND was made to account for the influence of the high phosphate level in the blood. These analyses show that the upregulated expression of all five genes (*Hamp2*, *Cxcl13*, *Ptp4a3*, *Serpinb6e*, *Il22ra2*) is further upregulated in the FGF23KO mice (Figure 8A and Table S16). The downregulated expression of five genes (*Col15a1*, *Aldh1l2*, *Clec11a*, *Serpinb6d*, *Defb8*) is further downregulated in the FGF23KO mice (Figure 8B and Table S16). Although the expression of *Actn3*, *Asb11*, *Klhl38*, *Atp2a1*, *Myot*, *Pde4dip*, *Rbfox1*, *Lrrc2*, and *Nrap* is merely unaffected by the phosphate overload (WT1WLP vs. WT1WHP), their expression is significantly upregulated by the FGF23 deficiency (Figure 8C and Table S16). In contrast, the expression of *Col11a1*, the other gene that is unaffected by the phosphate overload, is downregulated by the FGF23 deficiency (Figure 8C and Table S16). These results suggest that, upon phosphate overload the concurrent upregulation of FGF23 suppresses the excessive upregulation (*Hamp2*, *Cxcl13*, *Ptp4a3*, *Serpinb6e*, *Il22ra2*) (Figure 8A) and downregulation (*Col15a1*, *Aldh1l2*, *Clec11a*, *Serpinb6d*, *Defb8*) of the gene expression in the skin (Figure 8B). For *Actn3*, *Asb11*, *Klhl38*, *Atp2a1*, *Myot*, *Pde4dip*, *Rbfox1*, *Lrrc2*, *Col11a1*, and *Nrap*, the phosphate-overload-induced FGF23 upregulation suppresses and maintains the expression level even with the phosphate overload (Figure 8C), i.e., the phosphate-overload-induced FGF23 upregulation functions as a break for their otherwise upregulated

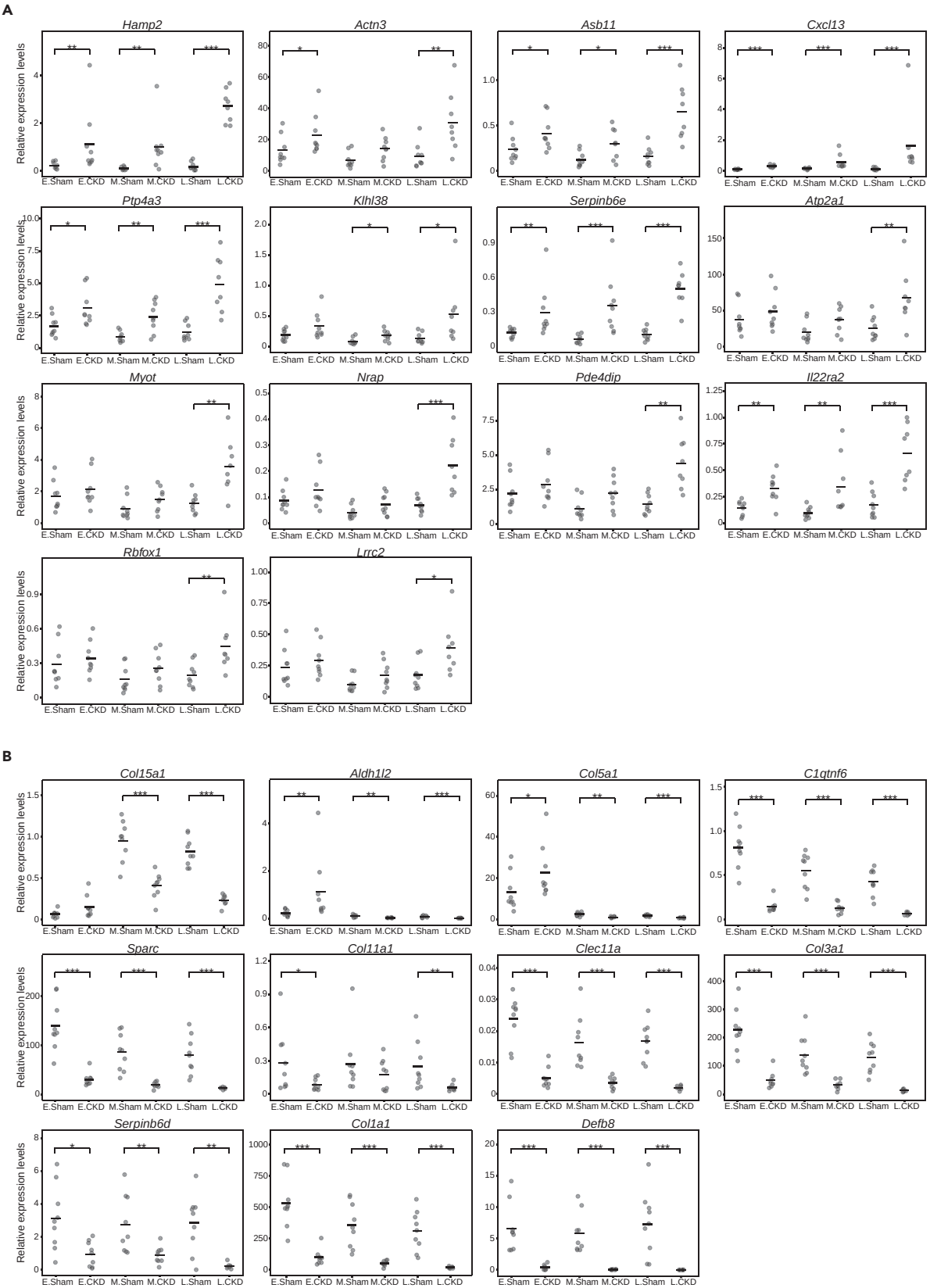
A
Hamp2
Actn3
Asb11
Cxcl13
Ptp4a3
Klhl38
Serpinb6e
Atp2a1
Myot
Nrap
Pde4dip
Il22ra2
Rbfox1
Lrrc2
B
Col15a1
Aldh1l2
Col5a1
C1qtnf6
Sparc
Col11a1
Clec11a
Col3a1
Serpinb6d
Col1a1
Defb8
Relative expression levels
E.Sham E.CKD M.Sham M.CKD L.Sham L.CKD

Figure 7. Differentially Expressed Skin Genes in the CKD Models

The qRT-PCR results for each upregulated (A) and downregulated (B) gene are shown. n = 9 (E.Sham), n = 9 (E.CKD), n = 9 (M.Sham), n = 9 (M.CKD), n = 9 (L.Sham), n = 8 (L.CKD).

*p < 0.05, **p < 0.01, and ***p < 0.001, Mann Whitney U-test. The mean is indicated by a horizontal line.

(*Actn3*, *Asb11*, *Klhl38*, *Atp2a1*, *Myot*, *Pde4dip*, *Rbfox1*, *Lrrc2*, *Nrap*) or downregulated (*Col11a1*) expression (Figure 8C).

The analyses also found evidence for a pathway that is less dependent on FGF23. For *Col3a1*, *C1qtnf6*, *Sparc*, and *Col1a1*, only slight downregulation is detected in the WT1WHP vs. FGF23KO1WHP comparison (Figure 8D), but not in the WT1WHP vs. FGF23KO1WND one (Figure 8D), despite the comparable increase in the blood phosphate level (Figure S9B). For *Col5a1*, neither WT1WND vs. FGF23KO1WND nor WT1WHP vs. FGF23KO1WHP comparison found statistically significant differences in the *Col5a1* expression (Figure 8D and Table S16). The WT1WHP vs. FGF23KO1WND comparison shows only marginal, if any, upregulation (ca. x1.7), with the p value of 0.0132 (Figure 8D and Table S16). These results suggest that the increased FGF23 level upon the phosphate overload influences very little, if any, of the phosphate-overload-mediated downregulation of these five skin genes.

The signaling by FGF23 is mediated by a cell surface receptor complex consisting of α-Klotho and FGFRs (Hu et al., 2013; John et al., 2011; Shen et al., 2016). To gain further insight into this bone-skin cross talk mediated by FGF23, we examined the body-wide expression patterns of *αKlotho* and *Fgfrs* (Figure 9). The expression of *αKlotho* is most abundant in the kidney as previously described (Kuro-o et al., 1997), but very little, if any, expression was detected in the skin (Figure 9). The transcripts for the co-receptors, *Fgfrs*, are more ubiquitously expressed (Figure 9). As αKlotho is the requisite receptor component for the FGF23 signaling (Chen et al., 2018; Hu et al., 2013; John et al., 2011; Lee et al., 2018; Shen et al., 2016), it is unlikely that FGF23 acts directly on the skin. Instead, the FGF23 effects are mediated by yet another factor(s) that is(are) regulated by FGF23.

Putative Inter-Organ Cross talk Network

The characterization of the skin gene expressions in the disease models led us to identify the bone-skin cross talk mediated by the bone-derived hormone FGF23 and its regulation by phosphate homeostasis (Figures 7 and 8). Hence, we next took advantage of the rich multi-organ datasets across multiple disease models to identify more signature activities of inter-organ cross talk for the disease models. WGCNA was applied to the datasets for each disease model (Figures 10, 11, 12, 13, 14, 15, and 16 and see Transparent Methods). This analysis identified modules consisting of multiple organ GO term units in each model (Figures 10, 11, 12, 13, 14, 15, and 16). We found several modules in each disease model that exhibit a relatively stronger correlation with a specific pathophysiological condition than with the others (Figures 10, 11, 12, 13, 14, 15, and 16, Tables S17–S23).

For example, in the MI model (Figure 10), the "red" module shows the strongest correlation (correlation coefficient, 0.87786; p value, 2.06×10^{-12}) with E.MI. The top-ranked organ GO term units for each organ in this module are "bone marrow (BM) regulation of viral budding via host ESCRT complex (ID: 1084)," "brain transport (ID: 1258)," "heart cellular metabolic process (ID: 129)," "kidney small molecule metabolic process (ID: 1192)," "liver metabolic process (ID: 477)," "lung immune response (ID: 365)," "pancreas cellular amino acid metabolic process (ID: 120)," "skeletal muscle (SkMuscle) macromolecule catabolic process (ID: 445)," "spleen metabolic process (ID: 477)," "testis negative regulation of response to DNA damage stimulus (ID: 652)," "thymus cellular response to epidermal growth factor stimulus (ID: 148)," and "white adipose tissue (WAT) regulation of I-κB kinase/NF-κB signaling (ID: 999)" (Figure 10 and Table S17).

In the CKD model (Figure 12), the "paleturquoise" module shows the strongest correlation (correlation coefficient, 0.968783; p value: 2.22×10^{-7}) with E.CKD (Figure 12 and Table S19). The top-ranked organ GO terms for each organ in this module are "adrenal gland (AdrenalG)-female gamete generation (ID: 201)," "aorta positive regulation of B cell apoptotic process (ID: 473)," "brain-intermediate filament organization (ID: 260)," "colon-formation of cytoplasmic translation initiation complex (ID: 205)," "eye chemoattraction of dopaminergic neuron axon (ID: 114)," "heart regulation of platelet-derived growth factor receptor signaling pathway (ID: 664)," "ileum-dihydrobiopterin metabolic process (ID: 148),"

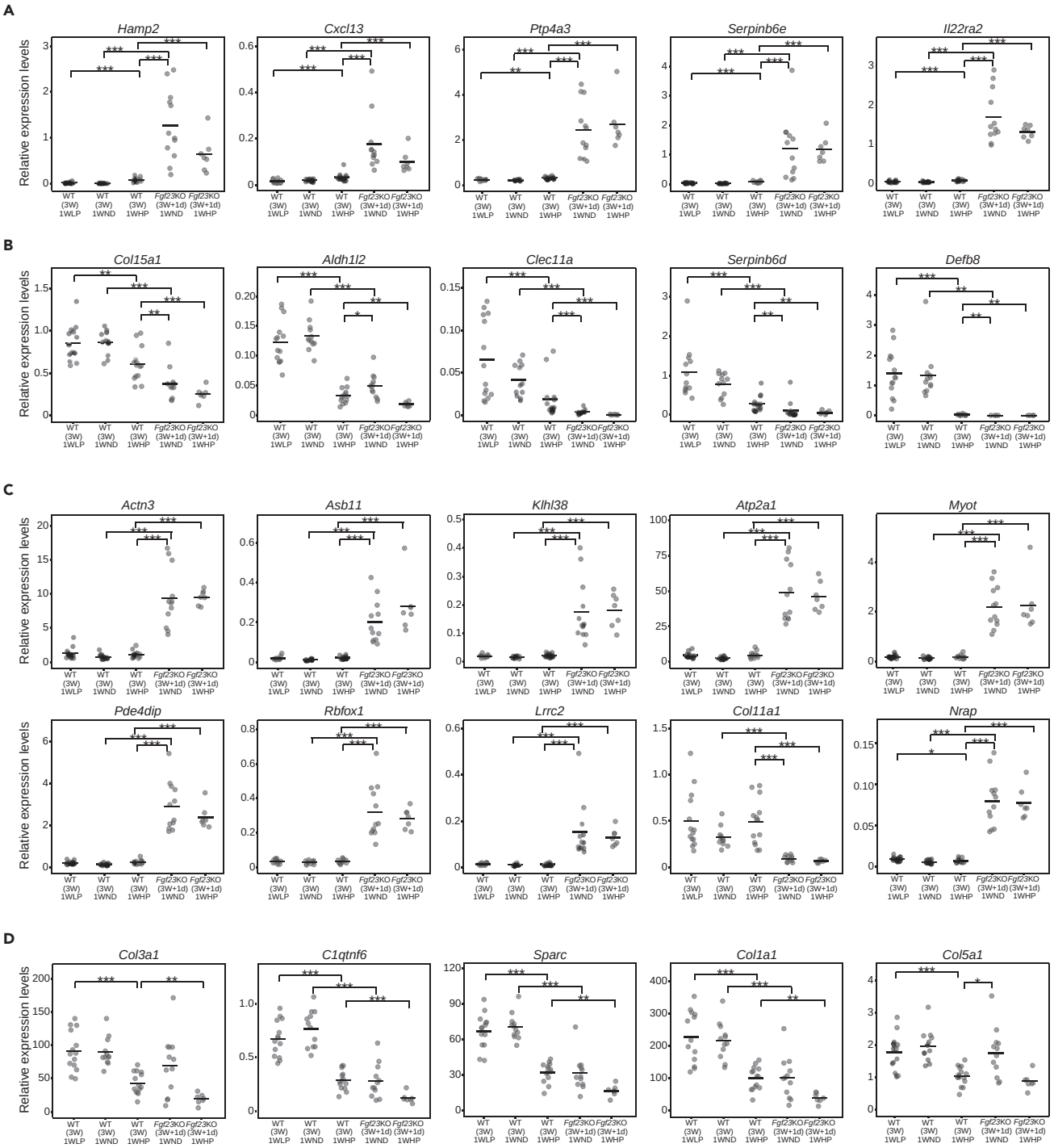

Figure 8. Differentially Expressed Skin Genes in the Phosphorus-Overload Models in Wild Type (WT) and FGF23-Deficient (FGF23KO) Mice

The qRT-PCR results for genes that are upregulated (A), downregulated (B), unaffected (C), and downregulated but relatively less affected by the FGF23KO (D) upon phosphate overload are shown. The phosphate overload was initiated at 3 weeks old for all WT and indicated as WT(3W). For FGF23KO, the phosphate overload was initiated at 3 weeks plus 1 day and indicated as FGF23KO (3W+1d). For all graphs in (A) and the WT(3W)1WHP vs. FGF23KO(3W+1d) 1WND and the WT(3W)1WHP vs. FGF23KO(3W+1d)1WHP comparisons for *Defb8* in (B), it may be difficult to see the upregulation (A) or downregulation even with the statistical significance. This results from accommodating widely distributed dots along the y axis in the same graph. The statistically significant and robust gene expression changes can be confirmed by examining the raw data and statistical analyses shown in Table S16. LP, low-phosphorus diet; ND, normal diet; HP, high-phosphorus diet. n = 13–14 (WT1WLP), n = 12 (WT1WND), n = 14 (WT1WHP), n = 12 (FGF23KO1WND), n = 7 (FGF23KO1WHP). *p < 0.05, **p < 0.01, and ***p < 0.001, Mann Whitney U-test. The mean is indicated by a horizontal line.

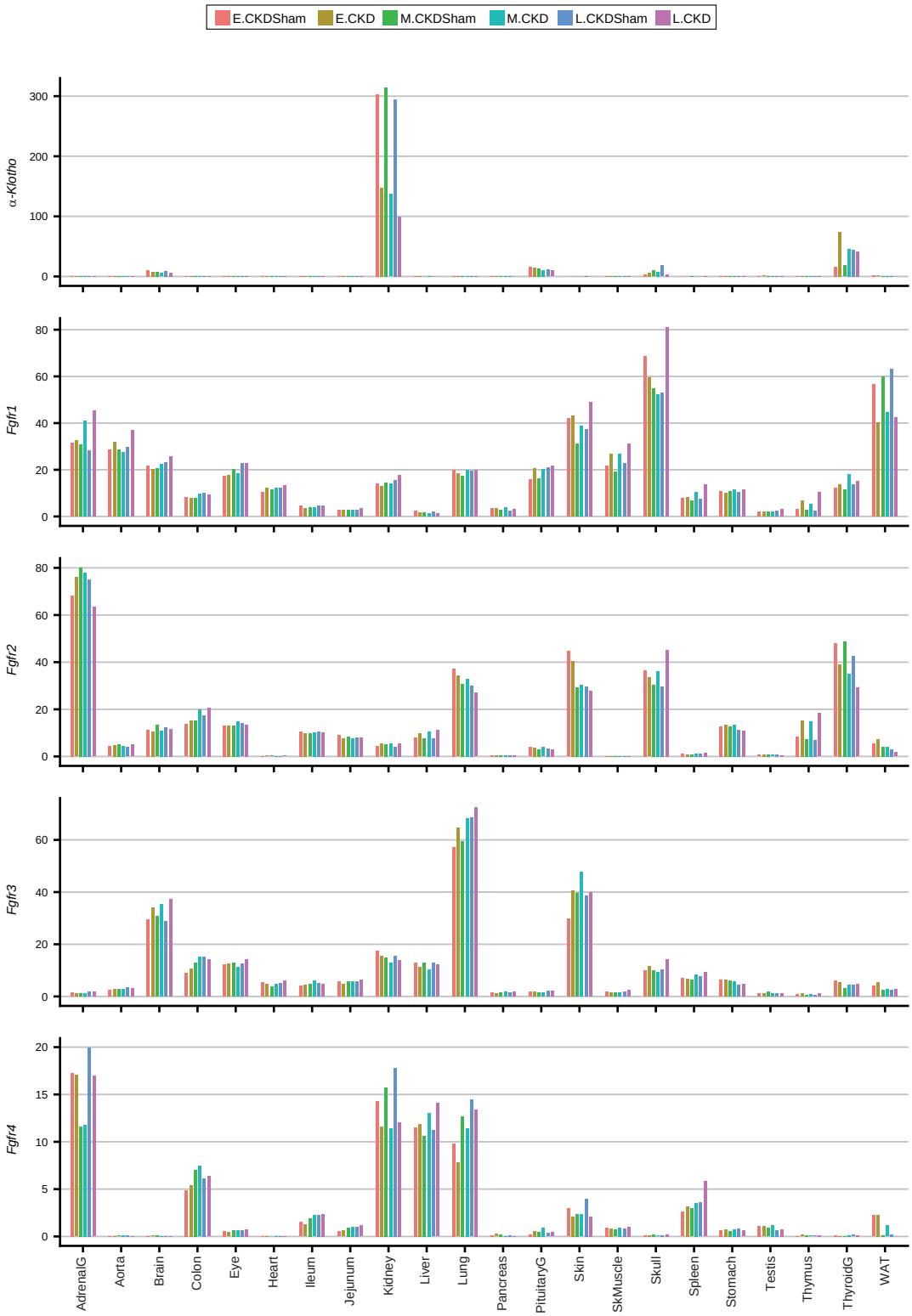

Figure 9. Expression Patterns of *α-Klotho*, *Fgfr1*, *Fgfr2*, *Fgfr3*, and *Fgfr4* across the Organs

The FPKM for each gene in each sample is shown as bar graph. The organ names are indicated at the bottom. Shown are for all CKD models and the sham controls.

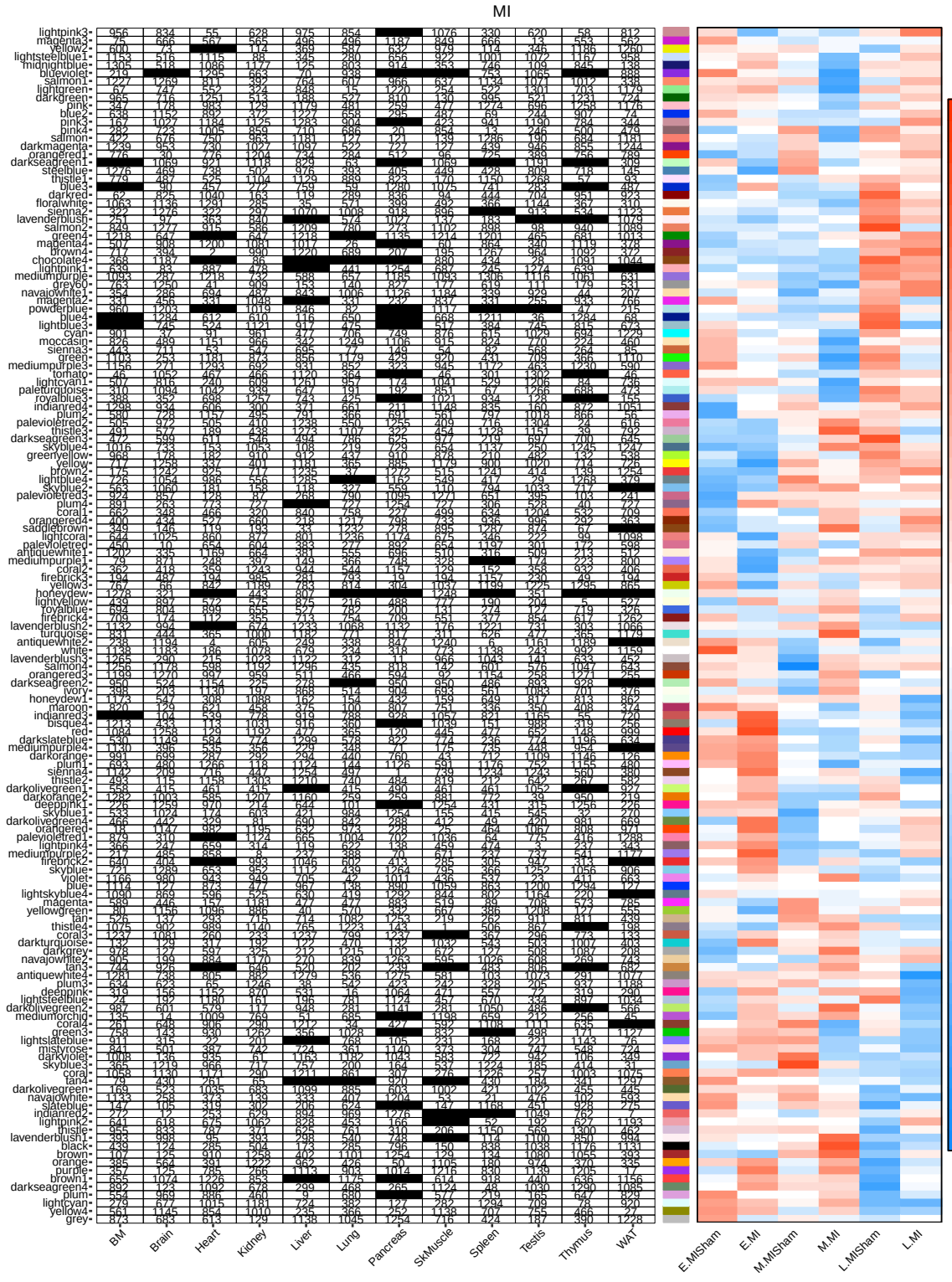

Figure 10. Characterization of Putative Inter-Organ Cross talk in the MI Models

Modules identified by WGCNA using the datasets of the MI models are shown. The top GO term of each organ for each module is indicated by the number and is described in full in Table S17. The organ(s) that is(are) not represented in the module is(are) indicated by ■. The correlation coefficient and the p value (Student's asymptotic t test) of each module and the complete list of GO terms with their p values (Fisher's exact test) are shown in Table S17.

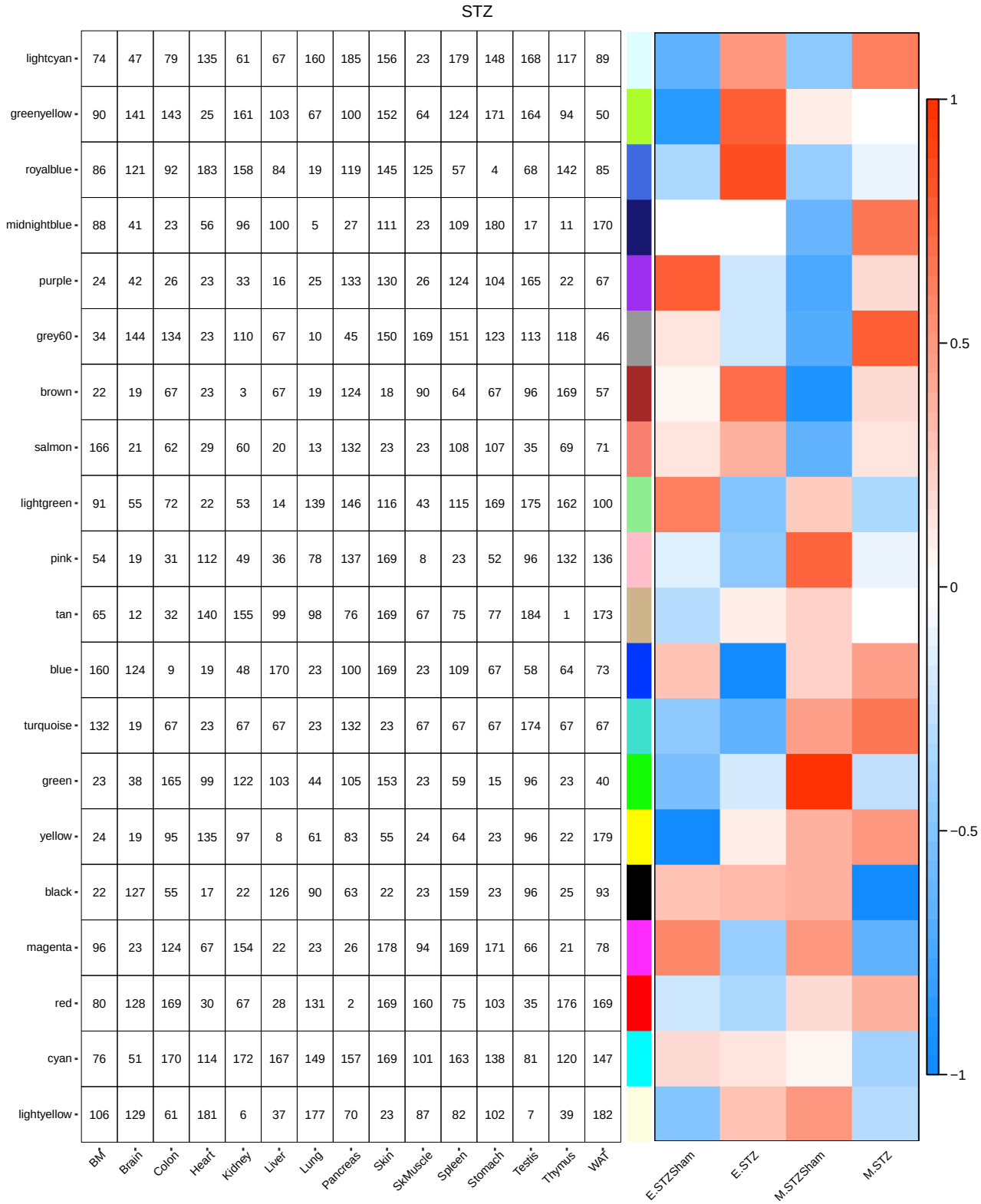

Figure 11. Characterization of Putative Inter-Organ Cross talk in the STZ-Induced Diabetes Models

Modules identified by WGCNA using the datasets of the STZ-induced diabetes models are shown. The correlation coefficient and the p value (Student's asymptotic t test) of each module and the complete list of GO terms with their p values (Fisher's exact test) are shown in Table S18.

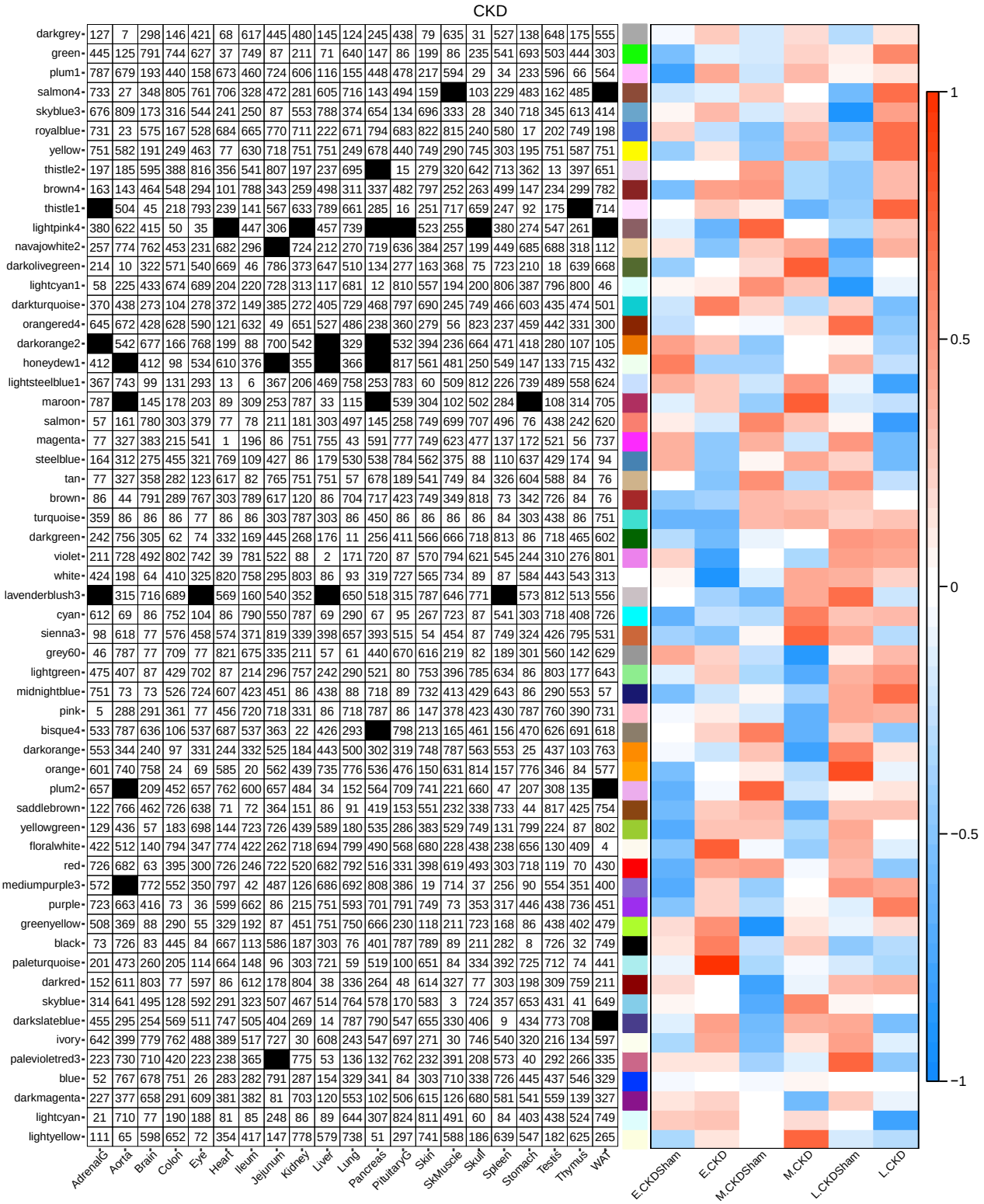

Figure 12. Characterization of Putative Inter-Organ Cross talk in the CKD Models

Modules identified by WGCNA using the datasets of the CKD models are shown. The organ(s) that is(are) not represented in the module is(are) indicated by ■. The correlation coefficient and the p value (Student's asymptotic t test) of each module and the complete list of GO terms with their p values (Fisher's exact test) are shown in Table S19.

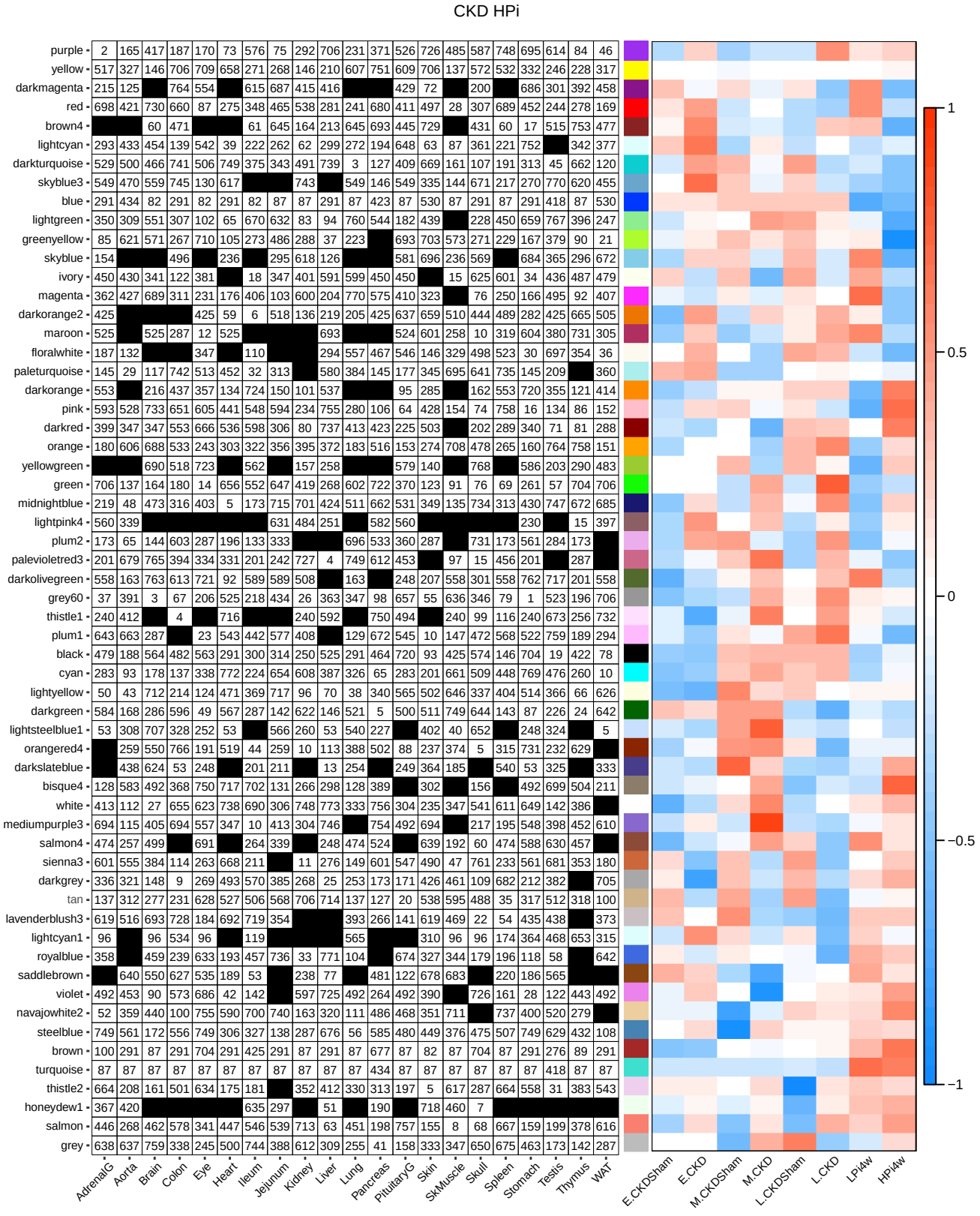
CKD HPi
purple 2 165 417 187 170 73 576 75 292 706 231 371 526 726 485 587 748 695 614 84 46
yellow 517 327 146 706 709 658 271 268 146 210 607 751 609 706 137 572 532 332 246 228 317
darkmagenta 215 125 764 554 615 687 415 416 429 72 200 686 301 392 458
red 698 421 730 660 87 275 348 465 538 281 241 680 411 497 28 307 689 452 244 278 169
brown4 60 471 61 645 164 213 645 693 445 729 431 60 17 515 753 477
lightcyan 293 433 454 139 542 39 222 262 62 299 272 194 648 63 87 361 221 752 342 377
darkturquoise 529 500 466 741 506 749 375 343 491 739 3 127 409 669 161 107 191 313 45 662 120
skyblue3 549 470 559 745 130 617 743 549 146 549 335 144 671 217 270 770 620 455
blue 291 434 82 291 82 291 82 87 87 291 87 423 87 530 87 291 87 291 418 87 530
lightgreen 350 309 551 307 102 65 670 632 83 94 760 544 182 439 228 450 659 767 396 247
greenyellow 85 621 571 267 710 105 273 486 288 37 223 693 703 573 271 229 167 379 90 21
skyblue 154 496 236 295 618 126 581 696 236 569 684 365 296 672
ivory 450 430 341 122 381 18 347 401 591 599 450 450 15 625 601 34 436 487 479
magenta 362 427 689 311 231 176 406 103 600 204 770 575 410 323 76 250 166 495 92 407
darkorange2 425 425 59 6 518 136 219 205 425 637 659 510 444 489 282 425 665 505
maroon 525 525 287 12 525 693 524 601 258 10 319 604 380 731 305
floralwhite 187 132 347 110 294 557 467 546 146 329 498 523 30 697 354 36
paleturquoise 145 29 117 742 513 452 32 313 580 384 145 177 345 695 641 735 145 209 360
darkorange 553 216 437 357 134 724 150 101 537 95 285 162 553 720 355 121 414
pink 593 528 733 651 605 441 548 594 234 755 280 106 64 428 154 74 758 16 134 86 152
darkred 399 347 347 553 666 536 598 306 80 737 413 423 225 503 202 289 340 71 81 288
orange 180 606 688 533 243 303 322 356 395 372 183 516 153 274 708 478 265 160 764 758 151
yellowgreen 690 518 723 562 157 258 579 140 768 586 203 290 483
green 706 137 164 180 14 656 552 647 419 268 602 722 370 123 91 76 69 261 57 704 706
midnightblue 219 48 473 316 403 5 173 715 701 424 511 662 531 349 135 734 313 430 747 672 685
lightpink4 560 339 631 484 251 582 560 230 15 397
plum2 173 65 144 603 287 196 133 333 696 533 360 287 731 173 561 284 173
palevioletred3 201 679 765 394 334 331 201 242 727 4 749 612 453 97 15 456 201 287
darkolivegreen 558 163 763 613 721 92 589 589 508 163 248 207 558 301 558 762 717 201 558
grey60 37 391 3 67 206 525 218 434 26 363 347 98 657 55 636 346 79 1 523 196 706
thistle1 240 412 4 716 240 592 750 494 240 99 116 240 673 256 732
plum1 643 663 287 23 543 442 577 408 129 672 545 10 147 472 568 522 759 189 294
black 479 188 564 482 563 291 300 314 250 525 291 464 720 93 425 574 146 704 19 422 78
cyan 283 93 178 137 338 772 224 654 608 387 326 65 283 201 661 509 448 769 476 260 10
lightyellow 50 43 712 214 124 471 369 717 96 70 38 340 565 502 646 337 404 514 366 66 626
darkgreen 584 168 286 596 49 567 287 142 622 146 521 5 500 511 749 644 143 87 226 24 642
lightsteelblue1 53 308 707 328 252 53 566 260 53 540 227 402 40 652 248 324 5
orangered4 259 550 766 191 519 44 259 10 113 388 502 88 237 374 5 315 731 232 629
darkslateblue 438 624 53 248 201 211 13 254 249 364 185 540 53 325 333
bisque4 128 583 492 368 750 717 702 131 266 298 128 389 302 156 492 699 504 211
white 413 112 27 655 623 738 690 306 748 773 333 756 304 235 347 541 611 649 142 386
mediumpurple3 694 115 405 694 557 347 10 413 304 746 754 492 694 217 195 548 398 452 610
salmon4 474 257 499 691 264 339 248 474 524 639 192 60 474 588 630 457
sienna3 601 555 384 114 263 668 211 11 276 149 601 547 490 47 761 233 561 681 353 180
darkgrey 336 321 148 9 269 493 570 385 268 25 253 173 171 426 461 109 682 212 382 705
tan 137 312 277 231 628 527 506 568 706 714 137 127 20 538 595 488 35 317 512 318 100
lavenderblush3 619 516 693 728 184 692 719 354 393 266 141 619 469 22 54 435 438 373
lightcyan1 96 96 534 96 119 565 310 96 96 174 364 468 653 315
royalblue 358 459 239 633 193 457 736 33 771 104 674 327 344 179 196 118 58 642
saddlebrown 640 550 627 535 189 53 238 77 481 122 678 683 220 186 565
violet 492 453 90 573 686 42 142 597 725 492 264 492 390 726 161 28 122 443 492
navajowhite2 52 359 440 100 755 590 700 740 163 320 111 486 468 351 711 737 400 520 279
steelblue 749 561 172 556 749 306 327 138 287 676 56 585 480 449 376 475 507 749 629 432 108
brown 100 291 87 291 704 291 425 291 87 291 87 677 87 82 87 704 87 291 276 89 291
turquoise 87 87 87 87 87 87 87 87 87 87 87 434 87 87 87 87 87 87 418 87 87
thistle2 664 208 161 501 634 175 181 352 412 330 313 197 5 617 287 664 558 31 383 543
honeydew1 367 420 635 297 51 190 718 460 7
salmon 446 268 462 578 341 447 546 539 713 63 451 198 757 155 8 68 667 159 199 378 616
grey 638 637 759 338 245 500 744 388 612 309 255 41 158 333 347 650 675 463 173 142 287
AdrenalG Aorta Brain Colon Eye Heart Ileum Jejunum Kidney Liver Lung Pancreas PituitaryG Skin SkMuscle Skull Spleen Stomach Testis Thymus WAT
E.CKDSham E.CKD M.CKDSham M.CKD L.CKDSham L.CKD LPi4w HPi4w
1
0.5
0
−0.5
−1

Figure 13. Characterization of Putative Inter-Organ Cross talk in the CKD and Phosphorus-Overload Models

Modules identified by WGCNA using the datasets of the CKD and phosphorus-overload models are shown. The organ(s) that is(are) not represented in the module is(are) indicated by ■. The correlation coefficient and the p value (Student's asymptotic t test) of each module and the complete list of GO terms with their p values (Fisher's exact test) are shown in Table S20.

"jejunum-cellular response to interferon-gamma (ID: 96)," "kidney-metabolic process (ID:303)," "liver-ribosomal small subunit biogenesis (ID: 721)," "lung-cell competition in a multicellular organism (ID: 59)," "pancreas-positive regulation of respiratory burst involved in inflammatory response (ID: 519)," "pituitary gland (PituitaryG)-cellular response to nutrient (ID: 100)," "skin-regulation of mitophagy (ID: 651)," "skeletal muscle (SkMuscle)-cellular macromolecule metabolic process (ID: 84)," "skull-mRNA transcription from RNA polymerase II promoter (ID: 334)," "spleen-negative regulation of muscle adaptation (ID: 392)," "stomach-RNA phosphodiester bond hydrolysis (ID: 725)," "testis-response to TNF agonist (ID: 712)," "thymus-cellular component disassembly (ID: 74)," and "white adipose tissue (WAT)-organic substance transport (ID: 441)" (Figure 12 and Table S19).

Similarly, in these and other models, there are many more modules, each of which shows a uniquely strong correlation to a specific pathophysiological condition (Figures 10, 11, 12, 13, 14, 15, and 16). In such modules, each of the organs are linked to not only the top-ranked GO term but also multiple other GO terms (see Tables S17–S23 for the complete list). This suggests that each of these organs forms an inter-organ cross talk network via biological functions expressed by their corresponding GO terms within the module. Hence, each of such modules may represent the signature activity of the inter-organ cross talk for the specific pathophysiological condition.

Human-Mouse Comparisons

Another utility of such body-wide multi-organ and multi-model datasets was also examined. The similarities and dissimilarities between experimental animal models and the human have been a subject of long-standing discussion. Herein, we provide the body-wide multi-organ and multi-model RNAseq datasets of the mouse, one of the most commonly used experimental animal models. Several multi-organ human RNAseq datasets are publicly available (GTEx Consortium, 2013; Franzen et al., 2016; Uhlen et al., 2015). Hence, the comparison between our mouse datasets and such human datasets could provide an insight into the questions about the mouse-human relatedness. The gene expression pattern in each organ of each mouse model reported herein was compared with that in the corresponding organ of human subjects. The comparison was conducted by calculating Spearman's rank correlation coefficients between the mouse and human data (Figures 17 and 18 and see Transparent Methods). The human data are derived from The Human Protein Atlas (https://www.proteinatlas.org) and represent those of relatively healthy human subjects.

The comparison between mouse and human was first made for each organ (Figure 17). The results suggest that the heart, the pancreas, the skeletal muscle (SKMuscle), and the spleen show a higher degree of similarity between the mouse and the human (Figure 17). In contrast, the testis data of the mouse and the human show the lowest similarity (Figure 17). Next, the comparison among all organs of both mouse and human was made (Figure 18). The result shows that both brain and testis exhibit far distinctive patterns among all organs in both mouse and human (Figure 18). For each of these two organs, the mouse-to-human difference is much less than the brain/testis-to-the other organs differences (Figure 18). The heart pattern appears to be closely related to that of the skeletal muscle in both mouse and human (Figure 18), suggesting that the relatedness of these two organs offset the species difference to some extent (Figure 18).

In addition, we compared the mouse heart datasets of the MI models with those derived from a patient with heart failure with ischemic heart disease (Figure 19 and see Transparent Methods). The WGCNA of the mouse heart datasets of the MI models identified 13 modules (Figure 19). A uniquely strong correlation with M.MI (the fibrosis stage) was found with "turquoise (correlation coefficient, −0.72763; p value, 5.59×10^{-5})," "blue (correlation coefficient, 0.719743; p value, 7.35×10^{-5})," and "green (correlation coefficient, 0.812496; p value, 1.42×10^{-6})" modules. In all of these three modules, there are several GO terms that rank among the top 20 GO terms in the human sample (Figure 19). In particular, the GO term "carbohydrate derivative biosynthetic process" shows the p values of 7.00×10^{-4}, 5.50×10^{-7}, and 8.60×10^{-6} in the human ischemic heart, "turquoise" module of the mouse M.MI heart, and "blue" module of the mouse M.MI heart, respectively (Figure 19 and Table S24). This and other signature GO

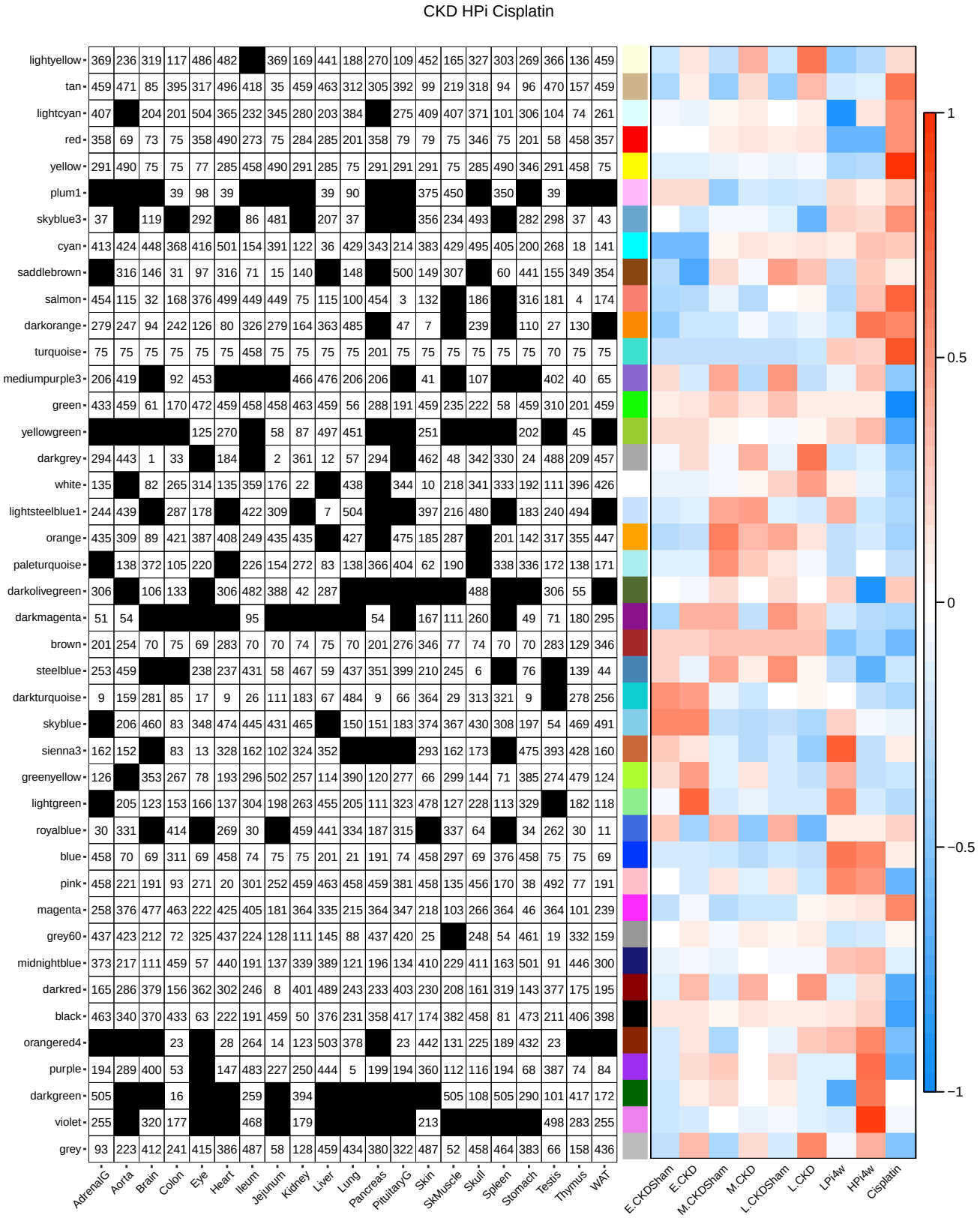
CKD HPi Cisplatin
lightyellow 369 236 319 117 486 482 369 169 441 188 270 109 452 165 327 303 269 366 136 459
tan 459 471 85 395 317 496 418 35 459 463 312 305 392 99 219 318 94 96 470 157 459
lightcyan 407 204 201 504 365 232 345 280 203 384 275 409 407 371 101 306 104 74 261
red 358 69 73 75 358 490 273 75 284 285 201 358 79 79 75 346 75 201 58 458 357
yellow 291 490 75 75 77 285 458 490 291 285 75 291 291 291 75 285 490 346 291 458 75
plum1 39 98 39 39 90 375 450 350 39
skyblue3 37 119 292 86 481 207 37 356 234 493 282 298 37 43
cyan 413 424 448 368 416 501 154 391 122 36 429 343 214 383 429 495 405 200 268 18 141
saddlebrown 316 146 31 97 316 71 15 140 148 500 149 307 60 441 155 349 354
salmon 454 115 32 168 376 499 449 449 75 115 100 454 3 132 186 316 181 4 174
darkorange 279 247 94 242 126 80 326 279 164 363 485 47 7 239 110 27 130
turquoise 75 75 75 75 75 75 458 75 75 75 75 201 75 75 75 75 75 75 70 75 75
mediumpurple3 206 419 92 453 466 476 206 206 41 107 402 40 65
green 433 459 61 170 472 459 458 458 463 459 56 288 191 459 235 222 58 459 310 201 459
yellowgreen 125 270 58 87 497 451 251 202 45
darkgrey 294 443 1 33 184 2 361 12 57 294 462 48 342 330 24 488 209 457
white 135 82 265 314 135 359 176 22 438 344 10 218 341 333 192 111 396 426
lightsteelblue1 244 439 287 178 422 309 7 504 397 216 480 183 240 494
orange 435 309 89 421 387 408 249 435 435 427 475 185 287 201 142 317 355 447
paleturquoise 138 372 105 220 226 154 272 83 138 366 404 62 190 338 336 172 138 171
darkolivegreen 306 106 133 306 482 388 42 287 488 306 55
darkmagenta 51 54 95 54 167 111 260 49 71 180 295
brown 201 254 70 75 69 283 70 70 74 75 70 201 276 346 77 74 70 70 283 129 346
steelblue 253 459 238 237 431 58 467 59 437 351 399 210 245 6 76 139 44
darkturquoise 9 159 281 85 17 9 26 111 183 67 484 9 66 364 29 313 321 9 278 256
skyblue 206 460 83 348 474 445 431 465 150 151 183 374 367 430 308 197 54 469 491
sienna3 162 152 83 13 328 162 102 324 352 293 162 173 475 393 428 160
greenyellow 126 353 267 78 193 296 502 257 114 390 120 277 66 299 144 71 385 274 479 124
lightgreen 205 123 153 166 137 304 198 263 455 205 111 323 478 127 228 113 329 182 118
royalblue 30 331 414 269 30 459 441 334 187 315 337 64 34 262 30 11
blue 458 70 69 311 69 458 74 75 75 201 21 191 74 458 297 69 376 458 75 75 69
pink 458 221 191 93 271 20 301 252 459 463 458 459 381 458 135 456 170 38 492 77 191
magenta 258 376 477 463 222 425 405 181 364 335 215 364 347 218 103 266 364 46 364 101 239
grey60 437 423 212 72 325 437 224 128 111 145 88 437 420 25 248 54 461 19 332 159
midnightblue 373 217 111 459 57 440 191 137 339 389 121 196 134 410 229 411 163 501 91 446 300
darkred 165 286 379 156 362 302 246 8 401 489 243 233 403 230 208 161 319 143 377 175 195
black 463 340 370 433 63 222 191 459 50 376 231 358 417 174 382 458 81 473 211 406 398
orangered4 23 28 264 14 123 503 378 23 442 131 225 189 432 23
purple 194 289 400 53 147 483 227 250 444 5 199 194 360 112 116 194 68 387 74 84
darkgreen 505 16 259 394 505 108 505 290 101 417 172
violet 255 320 177 468 179 213 498 283 255
grey 93 223 412 241 415 386 487 58 128 459 434 380 322 487 52 458 464 383 66 158 436
AdrenalG Aorta Brain Colon Eye Heart Ileum Jejunum Kidney Liver Lung Pancreas PituitaryG Skin SkMuscle Skull Spleen Stomach Testis Thymus WAT
E.CKDSham E.CKD M.CKDSham M.CKD L.CKDSham L.CKD LPi4w HPi4w Cisplatin
1
0.5
0
−0.5
−1

Figure 14. Characterization of Putative Inter-Organ Cross talk in the CKD, the Phosphorus-Overload, and the Cisplatin-Induced Kidney Injury Models

Modules identified by WGCNA using the datasets of the CKD, the phosphorus-overload, and the cisplatin-induced kidney injury models are shown. The organ(s) that is(are) not represented in the module is(are) indicated by ■. The correlation coefficient and the p value (Student's asymptotic t test) of each module and the complete list of GO terms with their p values (Fisher's exact test) are shown in Table S21.

terms shared by the human ischemic heart and the mouse MI heart (the full list can be explored using Table S24) may represent common features between the human ischemic heart and the mouse MI model heart.

DISCUSSION

Herein we report the transcriptome landscape of the body-wide multi-organ across multi-disease and disease-related models. The mining of such comprehensive datasets provided evidence for more diverse and complex organ-to-organ and also model-to-model similarities and dissimilarities than conventionally assumed. In particular, we found the skin to be a unique organ that appears to sense and respond to disease and disease-related conditions in other non-skin organs.

The experimental validation of the inference derived from such data mining led to the uncovering of a previously less recognized cross-talk pathway between bone and skin, whereby a bone-derived systemic factor, FGF23, appears to function as a suppressor (Figures 8A–8C). In addition, we show evidence for a sensor function of the skin that is less dependent on FGF23 (Figure 8D).

Such differential gene expression in the skin could serve as biomarkers for detecting signs of diseases involving dysfunctional phosphate homeostasis, such as CKD and CKD-MBD (Hu et al., 2013; John et al., 2011; Kuro-o, 2013, 2017; Kuro-o and Moe, 2017; Kuro-o, 2010; Shen et al., 2016). In fact, an association of dermatological conditions with CKD has been reported (Brewster, 2008; Gagnon and Desai, 2013). They could also serve as biomarkers to determine whether a disease involves the FGF23 pathways. Furthermore, they could be used to determine the effects of therapeutics manipulating the FGF23 pathways (Aono et al., 2009; Degirolamo et al., 2016). With the recent development of a new non-invasive skin biopsy method using a micro-needle (http://www.minderadx.com/wp-content/uploads/2015/03/MiNDERA-SID-2017-Poster-.pdf), the utility of such skin biomarkers could be readily applicable to human subjects.

The signature activities of the inter-organ cross talk for diseases appear not to be limited to the bone-skin cross talk in phosphate homeostasis or kidney diseases. By applying WGCNA to the mouse datasets, we identified several modules consisting of multiple organ GO term (gene) units, each of which exhibits a strong correlation with a specific pathophysiological condition in each disease model (Figures 10, 11, 12, 13, 14, 15, and 16). Each of such modules may represent a putative inter-organ cross talk activity that signifies a specific pathophysiological condition of each disease model. Experimental validations of this finding in the future may prove such activities useful for disease diagnosis and/or selecting an effective treatment(s) for a particular disease.

The availability of such datasets also allowed us to gain insight into the relatedness between the human and animal models (Figures 17, 18, and 19). We found evidence for organ-to-organ variations in the degree of relatedness between the human and the mouse (Figure 17). Among the organs we studied, the testis exhibits the highest difference between the two. This finding may reflect species specificity for fertilization (Figure 17). The overall higher relatedness of certain organs, such as the heart, pancreas, skeletal muscle (SkMuscle), and spleen, than the others may reflect the evolutional conservation in the anatomical organization, cellular compositions, and/or physiological functions of these organs between the mouse and the human.

The heart appears to be highly related to the skeletal muscle, and the mouse-human difference for these two organs are relatively less (Figure 18). As both are contractile tissues, it is possible that cardiac and skeletal muscles retain highly conserved molecular and/or functional features through evolution. It is also possible that this reflects evolutionarily conserved molecular and/or functional features of peri-muscular cells, such as fibroblasts and fibroblastic cells. Alternatively, it is equally possible that the relatedness of these two organs across the different species reflect the highly conserved cell-type compositions in these two organs.

The comparison of the mouse MI models with the human ischemic heart derived from a patient with heart failure indicates several conserved features (Figure 19). Although more human subjects across various ages,

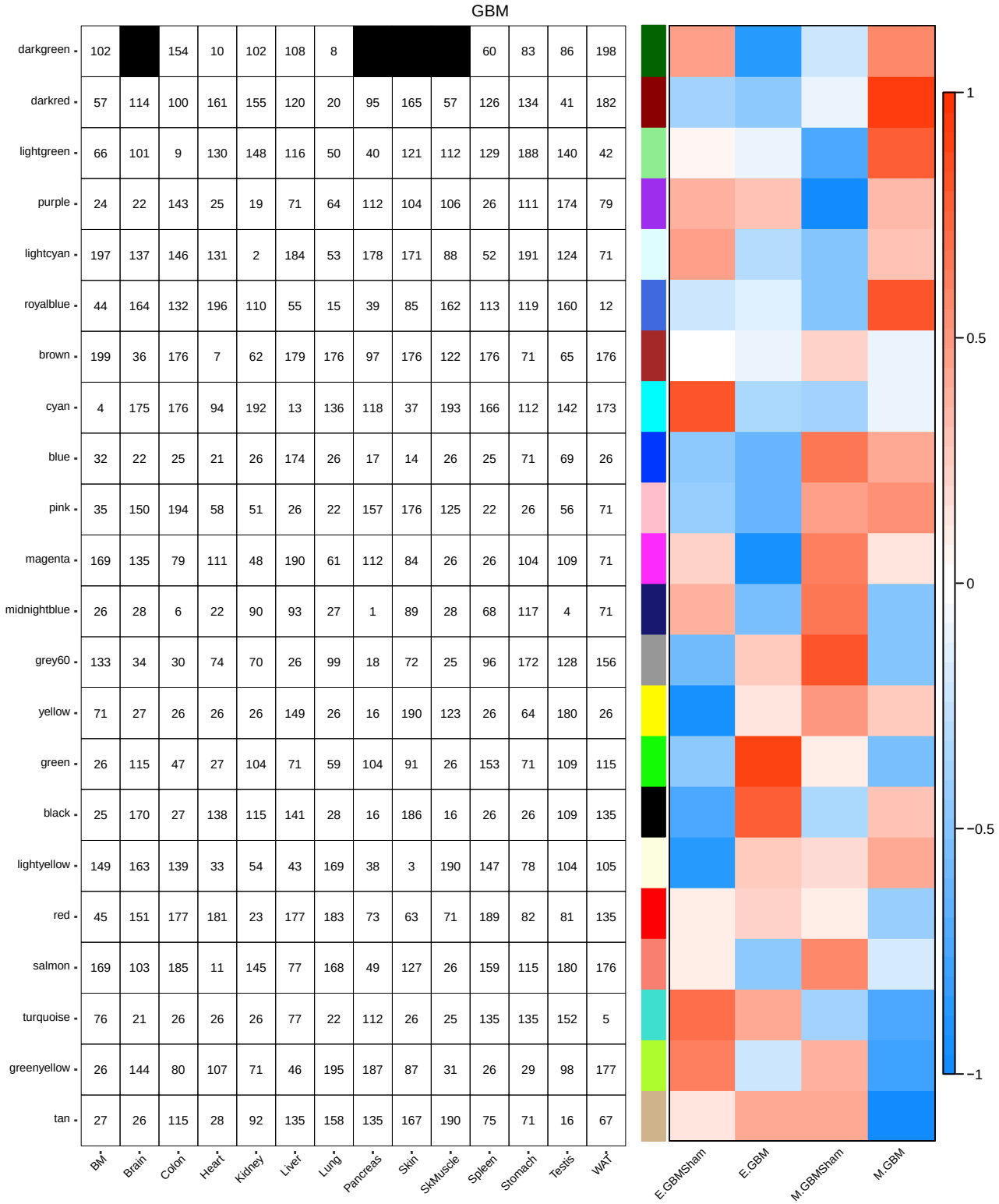

Figure 15. Characterization of Putative Inter-Organ Cross talk in the Tumor Models

Modules identified by WGCNA using the datasets of the tumor models are shown. The organ(s) that is(are) not represented in the module is(are) indicated by ■. The correlation coefficient and the p value (Student's asymptotic t test) of each module and the complete list of GO terms with their p values (Fisher's exact test) are shown in Table S22.

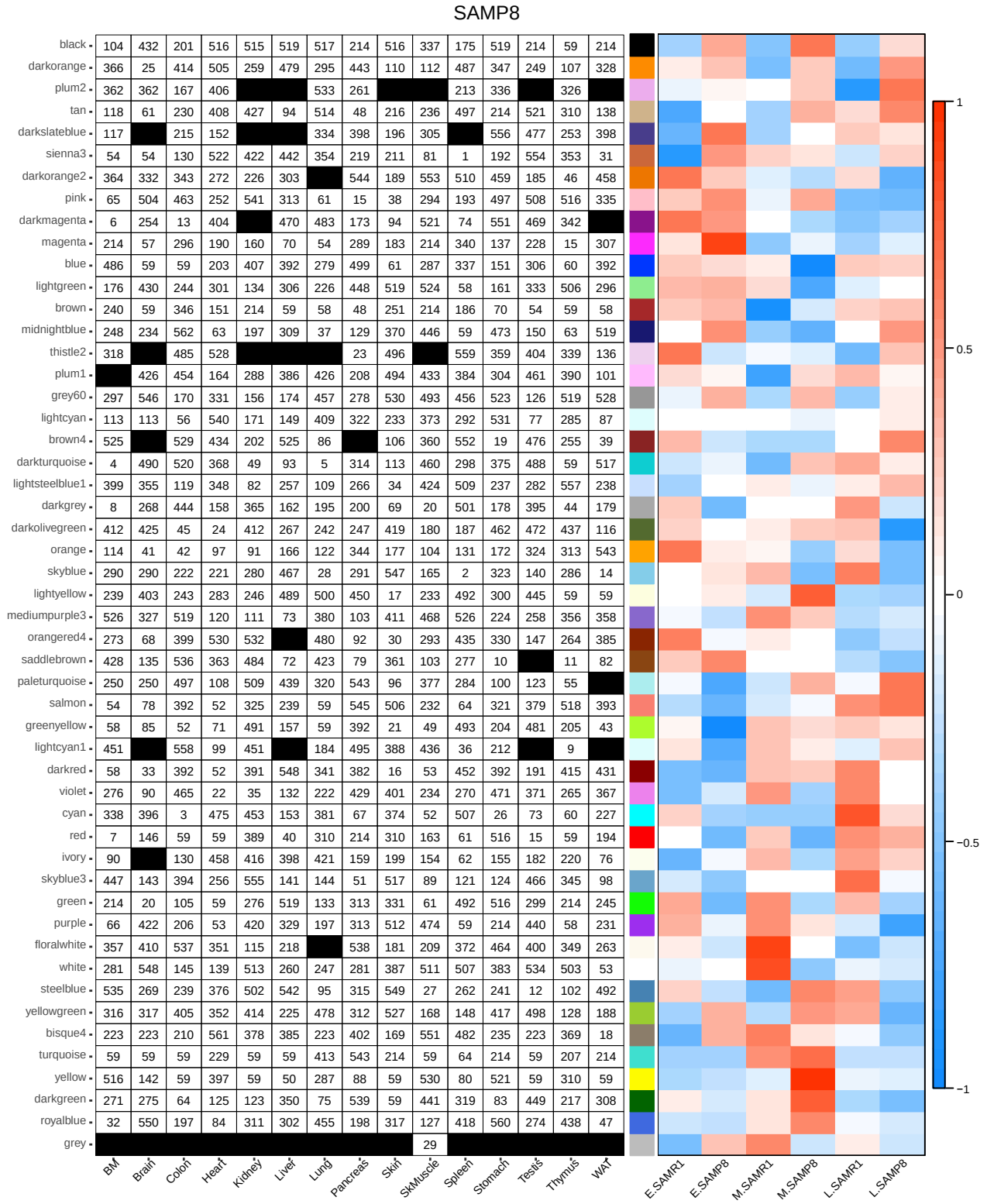

Figure 16. Characterization of Putative Inter-Organ Cross talk in the Pre-Mature Aging Models

Modules identified by WGCNA using the datasets of the premature-aging models are shown. The organ(s) that is(are) not represented in the module is(are) indicated by ■. The correlation coefficient and the p value (Student's asymptotic t test) of each module and the complete list of GO terms with their p values (Fisher's exact test) are shown in Table S23.

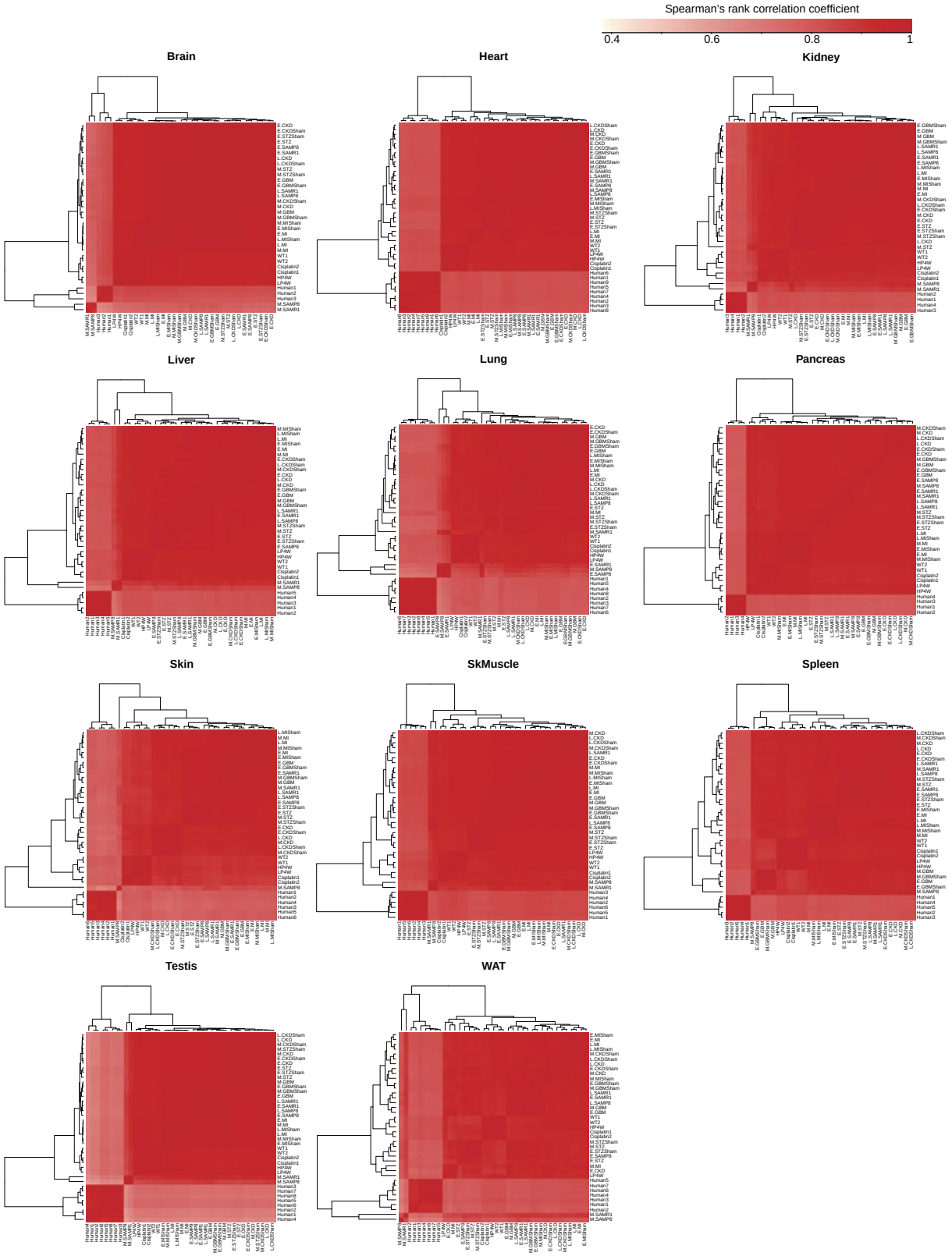

Figure 17. Heatmap of the Spearman's Correlation Coefficient between the Human and Mouse Models for Each Organ

The Spearman's correlation coefficients between the human and mouse models are calculated based on the FPKM of each gene.

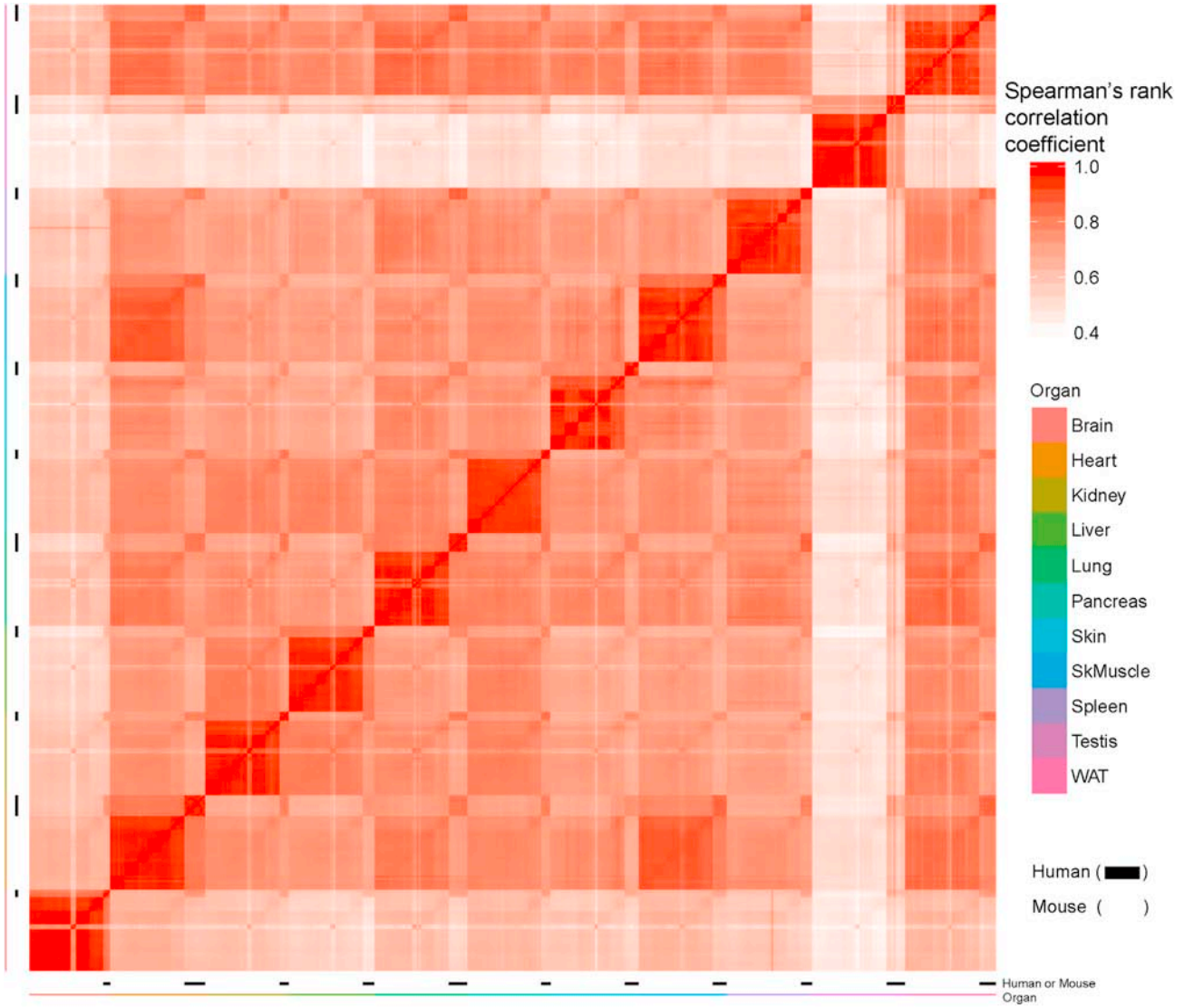

Figure 18. Heatmap of the Spearman's Correlation Coefficient between the Human and Mouse Models for All Organs

The Spearman's correlation coefficients between all human and mouse models across all organs are calculated based on the FPKM of each gene and are shown as heatmap.

sex, races, genetic backgrounds, and other accompanying conditions must be studied, the results suggest that the mouse MI models studied here reflect at least some features of human heart diseases. Further analyses of human subjects across more diverse backgrounds and their comparisons with the mouse MI models and other heart-disease-related models using the approach introduced here and other methods could facilitate better understanding of human heart diseases. Such cross-species studies could also help us select the most appropriate model to use to validate/test candidate therapeutics and also to make more appropriate interpretations of the results.

We took advantage of the comprehensive nature of the multi-organ and multi-model datasets reported herein to explore a possibility of uncovering more potential diagnostic biomarkers and candidate molecules for therapeutic treatments. Such possibilities were explored by applying a couple of other informatics tool. Likelihood analysis was conducted to make an overall multi-organ comparison rather than the conventional organ-to-organ comparison (Figure S10 and see Transparent Methods for the details). Partial least square discriminant analysis (PLS-DA) was applied to the datasets to characterize gene-organ unit(s) that

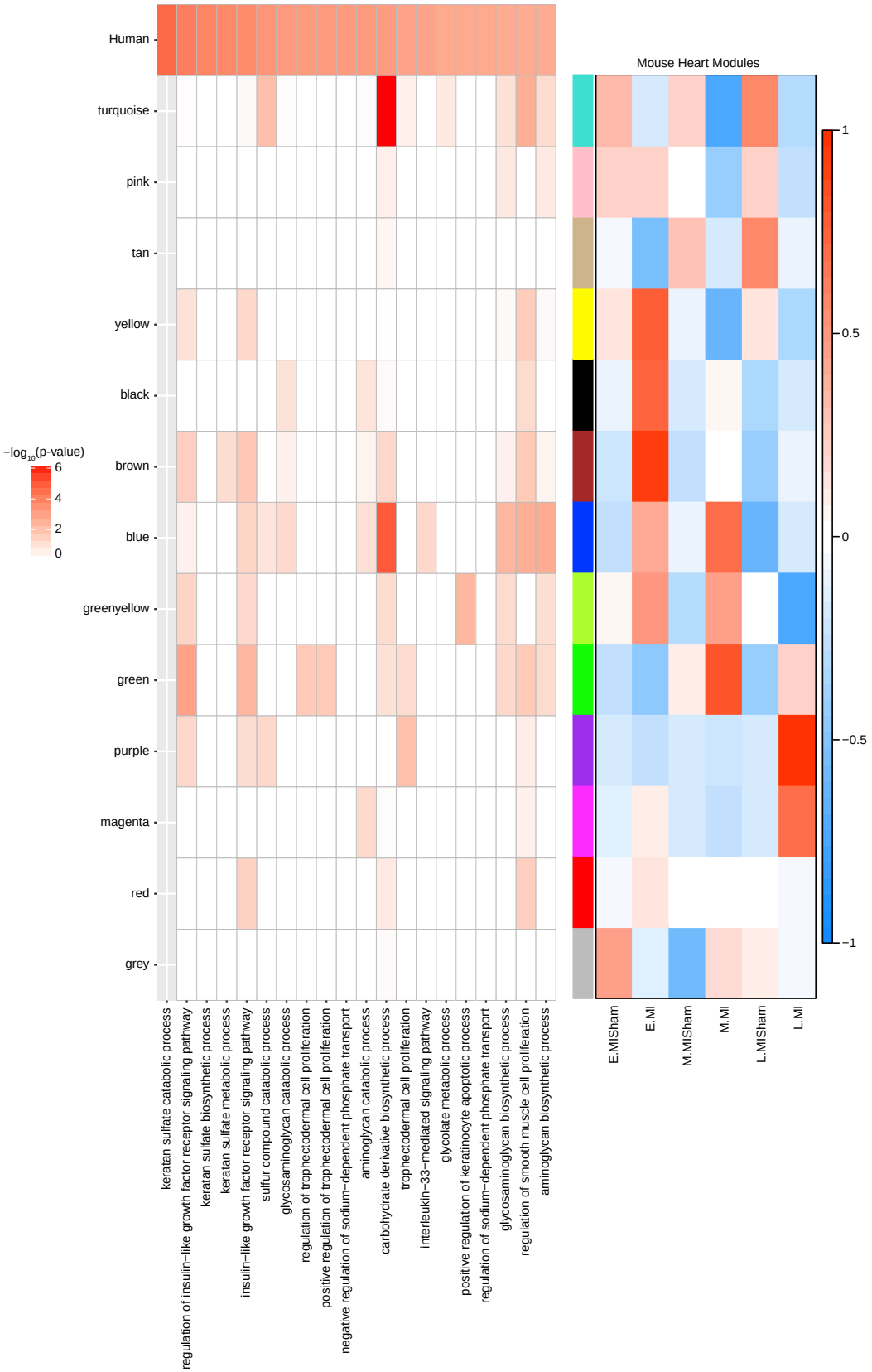
Human
turquoise
pink
tan
yellow
black
brown
blue
greenyellow
green
purple
magenta
red
grey
−log10(p-value)
6
4
2
0
keratan sulfate catabolic process
regulation of insulin−like growth factor receptor signaling pathway
keratan sulfate biosynthetic process
keratan sulfate metabolic process
insulin−like growth factor receptor signaling pathway
sulfur compound catabolic process
glycosaminoglycan catabolic process
regulation of trophectodermal cell proliferation
positive regulation of trophectodermal cell proliferation
negative regulation of sodium−dependent phosphate transport
aminoglycan catabolic process
carbohydrate derivative biosynthetic process
trophectodermal cell proliferation
interleukin−33−mediated signaling pathway
glycolate metabolic process
positive regulation of keratinocyte apoptotic process
regulation of sodium−dependent phosphate transport
glycosaminoglycan biosynthetic process
regulation of smooth muscle cell proliferation
aminoglycan biosynthetic process
Mouse Heart Modules
E.MISham
E.MI
M.MISham
M.MI
L.MISham
L.MI
1
0.5
0
−0.5
−1

Figure 19. Comparison of the Mouse MI Model Heart with the Human Heart of a Patient with Ischemic Heart Disease

The modules identified by WGCNA of the mouse MI model datasets (see Transparent Methods) are shown. The previously published (Liu et al., 2015) publicly available human heart RNAseq datasets (GSE57344) of healthy (non-failing) subjects and of a patient with heart failure with ischemic heart disease are analyzed. The p value (Fisher's exact test) of each human GO term in each mouse module is shown as heatmap. See Transparent Methods for the details. The correlation coefficient and the p value (Student's asymptotic t test) of each module and the complete list of GO terms with their p values (Fisher's exact test) are shown in Table S24.

could discriminate one disease model from the others (Figure S11 and see Transparent Methods for the details). The results appear to vary depending on which datasets are combined and analyzed. Although such analyses provided some signs of usefulness, experimental validations are required to confirm the utility of such findings. Furthermore, the reliability of such statistical analyses is critically dependent on the data size. Therefore, it is necessary to increase the sample size to the order of tens or hundreds or even more for each model. Although further work remains, the current analyses provide an initial foundation for the future studies.

Here we report the body-wide transcriptome landscape of diverse types of disease models and show its usefulness for the identification of candidate molecular signatures for disease diagnosis and treatments. We also illustrate another utility of such rich datasets by providing insights into the relationship between human and mouse models. The datasets reported herein could serve as a useful resource for the study of biology and medicine. The application of other analytical tools to these datasets and also expanding the dataset size and diversity in the future could facilitate better understanding of human biology and its applications to disease prevention and treatments.

METHODS

All methods can be found in the accompanying Transparent Methods supplemental file.

SUPPLEMENTAL INFORMATION

Supplemental Information includes Transparent Methods, 11 figures and 28 tables and can be found with this article online at https://doi.org/10.1016/j.isci.2018.03.014.

ACKNOWLEDGMENTS

We thank T. Ninomiya, T. Kuroda, and H. Anabuki for technical assistance; R. Takahashi and E. Kojima for administrative assistance; and T. Morie for managing the laboratory's daily operations. M.K., K.S., and H.K. thank K. Akiyama for his preparation of mouse organs from CKD models. J.H. Neale and S. Kawaoka read the initial draft versions and provided critical and constructive comments on the manuscript. We are also grateful to the Sato laboratory members for advice and discussion throughout the course of this work. This work was supported by JST ERATO Grant Number JPMJER1303 (T.N.S.), JSPS KAKENHI S Grant Number 22229007 (T.N.S.), AMED Grant Number JP17gm0610012 (M.K.), Society for the Promotion of Science Grant Number 16H05302 & 16K15470 (M.K.).

AUTHOR CONTRIBUTIONS

T.N.S. conceived the idea of the project, designed the overall experiments and *in silico* analyses and supervised the overall research project. S.K. performed the *in silico* analyses. R.U. and K.U. contributed to designing the experiments and performed the experiments. F.S., S.E., G.M.A., S.M.H., and K.N. contributed to the experiments. M.K. brought up the idea of using CKD mouse models for the study and contributed to the design of the experiments using the CKD mouse model. M.K., K.S., and H.K. developed the CKD mouse model and collected the organs from this model. Y.Y. and S.O. supervised and coordinated the clinical research and collected human tissue biopsies. T.N.S., S.K., R.U., and K.U. wrote the manuscript.

DECLARATION OF INTERESTS

T.N.S. is the inventor of several patents filed on aspects of the work presented herein and is the founder of and holds shares of Karydo TherapeutiX, Inc., which has exclusive rights to these patents. F.S., S.E., G.M.A., S.M.H., and K.N. are employees of Karydo TherapeutiX, Inc. Other authors declare no competing financial interests.

Received: January 23, 2018
Revised: March 9, 2018
Accepted: March 14, 2018
Published: March 29, 2018

REFERENCES

Aono, Y., Yamazaki, Y., Yasutake, J., Kawata, T., Hasegawa, H., Urakawa, I., Fujita, T., Wada, M., Yamashita, T., Fukumoto, S., et al. (2009). Therapeutic effects of anti-FGF23 antibodies in hypophosphatemic rickets/osteomalacia. J. Bone Miner. Res. *24*, 1879–1888.

Bergwitz, C., and Juppner, H. (2010). Regulation of phosphate homeostasis by PTH, vitamin D, and FGF23. Annu. Rev. Med. *61*, 91–104.

Blau, J.E., and Collins, M.T. (2015). The PTH-Vitamin D-FGF23 axis. Rev. Endocr. Metab. Disord. *16*, 165–174.

Bosworth, C., and de Boer, I.H. (2013). Impaired vitamin D metabolism in CKD. Semin. Nephrol. *33*, 158–168.

Brewster, U.C. (2008). Dermatological disease in patients with CKD. Am. J. Kidney Dis. *51*, 331–344.

Butterfield, D.A., and Poon, H.F. (2005). The senescence-accelerated prone mouse (SAMP8): a model of age-related cognitive decline with relevance to alterations of the gene expression and protein abnormalities in Alzheimer's disease. Exp. Gerontol. *40*, 774–783.

Chen, G., Liu, Y., Goetz, R., Fu, L., Jayaraman, S., Hu, M.C., Moe, O.W., Liang, G., Li, X., and Mohammadi, M. (2018). alpha-Klotho is a non-enzymatic molecular scaffold for FGF23 hormone signalling. Nature *553*, 461–466.

Cheng, Y., Kang, H., Shen, J., Hao, H., Liu, J., Guo, Y., Mu, Y., and Han, W. (2015). Beta-cell regeneration from vimentin+/MafB+ cells after STZ-induced extreme beta-cell ablation. Sci. Rep. *5*, 11703.

Degirolamo, C., Sabba, C., and Moschetta, A. (2016). Therapeutic potential of the endocrine fibroblast growth factors FGF19, FGF21 and FGF23. Nat. Rev. Drug Discov. *15*, 51–69.

Droujinine, I.A., and Perrimon, N. (2016). Interorgan communication pathways in physiology: focus on Drosophila. Annu. Rev. Genet. *50*, 539–570.

Duff, M., Demidova, O., Blackburn, S., and Shubrook, J. (2015). Cutaneous manifestations of diabetes mellitus. Clin. Diabetes *33*, 40–48.

Franzen, O., Ermel, R., Cohain, A., Akers, N.K., Di Narzo, A., Talukdar, H.A., Foroughi-Asl, H., Giambartolomei, C., Fullard, J.F., Sukhavasi, K., et al. (2016). Cardiometabolic risk loci share downstream cis- and trans-gene regulation across tissues and diseases. Science *353*, 827–830.

Gagnon, A.L., and Desai, T. (2013). Dermatological diseases in patients with chronic kidney disease. J. Nephropathol. *2*, 104–109.

Gnirs, K., and Prelaud, P. (2005). Cutaneous manifestations of neurological diseases: review of neuro-pathophysiology and diseases causing pruritus. Vet. Dermatol. *16*, 137–146.

Graham, M.L., Janecek, J.L., Kittredge, J.A., Hering, B.J., and Schuurman, H.J. (2011). The streptozotocin-induced diabetic nude mouse model: differences between animals from different sources. Comp. Med. *61*, 356–360.

GTEx Consortium (2013). The Genotype-tissue expression (GTEx) project. Nat. Genet. *45*, 580–585.

Guo, Y.C., and Yuan, Q. (2015). Fibroblast growth factor 23 and bone mineralisation. Int. J. Oral Sci. *7*, 8–13.

Hiratsuka, S., Watanabe, A., Aburatani, H., and Maru, Y. (2006). Tumour-mediated upregulation of chemoattractants and recruitment of myeloid cells predetermines lung metastasis. Nat. Cell Biol. *8*, 1369–1375.

Hu, M.C., Shiizaki, K., Kuro-o, M., and Moe, O.W. (2013). Fibroblast growth factor 23 and Klotho: physiology and pathophysiology of an endocrine network of mineral metabolism. Annu. Rev. Physiol. *75*, 503–533.

Ix, J.H., and Sharma, K. (2010). Mechanisms linking obesity, chronic kidney disease, and fatty liver disease: the roles of fetuin-A, adiponectin, and AMPK. J. Am. Soc. Nephrol. *21*, 406–412.

Jarve, A., Muhlstedt, S., Qadri, F., Nickl, B., Schulz, H., Hubner, N., Ozcelik, C., and Bader, M. (2017). Adverse left ventricular remodeling by glycoprotein nonmetastatic melanoma protein B in myocardial infarction. FASEB J. *31*, 556–568.

John, G.B., Cheng, C.Y., and Kuro-o, M. (2011). Role of Klotho in aging, phosphate metabolism, and CKD. Am. J. Kidney Dis. *58*, 127–134.

Karaiskos, N., Wahle, P., Alles, J., Boltengagen, A., Ayoub, S., Kipar, C., Kocks, C., Rajewsky, N., and Zinzen, R.P. (2017). The Drosophila embryo at single-cell transcriptome resolution. Science *358*, 194–199.

Kiaris, H., Schally, A.V., Nagy, A., Sun, B., Szepeshazi, K., and Halmos, G. (2000). Regression of U-87 MG human glioblastomas in nude mice after treatment with a cytotoxic somatostatin analog AN-238. Clin. Cancer Res. *6*, 709–717.

Kuro-o, M. (2010). A potential link between phosphate and aging–lessons from Klotho-deficient mice. Mech. Ageing Dev. *131*, 270–275.

Kuro-o, M. (2013). A phosphate-centric paradigm for pathophysiology and therapy of chronic kidney disease. Kidney Int. Suppl. (2011) *3*, 420–426.

Kuro-o, M. (2017). The FGF23 and Klotho system beyond mineral metabolism. Clin. Exp. Nephrol. *21*, 64–69.

Kuro-o, M., and Moe, O.W. (2017). FGF23-alphaKlotho as a paradigm for a kidney-bone network. Bone *100*, 4–18.

Kuro-o, M., Matsumura, Y., Aizawa, H., Kawaguchi, H., Suga, T., Utsugi, T., Ohyama, Y., Kurabayashi, M., Kaname, T., Kume, E., et al. (1997). Mutation of the mouse klotho gene leads to a syndrome resembling ageing. Nature *390*, 45–51.

Lee, S., Choi, J., Mohanty, J., Sousa, L.P., Tome, F., Pardon, E., Steyaert, J., Lemmon, M.A., Lax, I., and Schlessinger, J. (2018). Structures of beta-klotho reveal a 'zip code'-like mechanism for endocrine FGF signalling. Nature *553*, 501–505.

Liu, Y., Morley, M., Brandimarto, J., Hannenhalli, S., Hu, Y., Ashley, E.A., Tang, W.H., Moravec, C.S., Margulies, K.B., Cappola, T.P., et al. (2015). RNA-Seq identifies novel myocardial gene expression signatures of heart failure. Genomics *105*, 83–89.

McGrath, M.F., de Bold, M.L., and de Bold, A.J. (2005). The endocrine function of the heart. Trends Endocrinol. Metab. *16*, 469–477.

Megyesi, J., Safirstein, R.L., and Price, P.M. (1998). Induction of p21WAF1/CIP1/SDI1 in kidney tubule cells affects the course of cisplatin-induced acute renal failure. J. Clin. Invest. *101*, 777–782.

Miller, R.P., Tadagavadi, R.K., Ramesh, G., and Reeves, W.B. (2010). Mechanisms of cisplatin nephrotoxicity. Toxins (Basel) *2*, 2490–2518.

Mitsnefes, M.M., Betoko, A., Schneider, M.F., Salusky, I.B., Wolf, M.S., Juppner, H., Warady, B.A., Furth, S.L., and Portale, A.A. (2017). FGF23 and left ventricular hypertrophy in children with CKD. Clin. J. Am. Soc. Nephrol. *13*, 45–52.

Murakoshi, M., Saiki, K., Urayama, K., and Sato, T.N. (2013). An anthelmintic drug, pyrvinium pamoate, thwarts fibrosis and ameliorates myocardial contractile dysfunction in a mouse model of myocardial infarction. PLoS One *8*, e79374.

Pabla, N., Gibson, A.A., Buege, M., Ong, S.S., Li, L., Hu, S., Du, G., Sprowl, J.A., Vasilyeva, A., Janke, L.J., et al. (2015). Mitigation of acute kidney injury by cell-cycle inhibitors that suppress both CDK4/6 and OCT2 functions. Proc. Natl. Acad. Sci. USA *112*, 5231–5236.

Pervouchine, D.D., Djebali, S., Breschi, A., Davis, C.A., Barja, P.P., Dobin, A., Tanzer, A., Lagarde, J., Zaleski, C., See, L.H., et al. (2015). Enhanced transcriptome maps from multiple mouse tissues reveal evolutionary constraint in gene expression. Nat. Commun. *6*, 5903.

Port, J.D., Walker, L.A., Polk, J., Nunley, K., Buttrick, P.M., and Sucharov, C.C. (2011). Temporal expression of miRNAs and mRNAs in a mouse model of myocardial infarction. Physiol. Genomics *43*, 1087–1095.

Portale, A.A., Wolf, M., Juppner, H., Messinger, S., Kumar, J., Wesseling-Perry, K., Schwartz, G.J., Furth, S.L., Warady, B.A., and Salusky, I.B. (2014). Disordered FGF23 and mineral metabolism in children with CKD. Clin. J. Am. Soc. Nephrol. *9*, 344–353.

Portale, A.A., Wolf, M.S., Messinger, S., Perwad, F., Juppner, H., Warady, B.A., Furth, S.L., and Salusky, I.B. (2016). Fibroblast growth factor 23 and risk of CKD progression in children. Clin. J. Am. Soc. Nephrol. *11*, 1989–1998.

Portha, B., Blondel, O., Serradas, P., McEvoy, R., Giroix, M.H., Kergoat, M., and Bailbe, D. (1989). The rat models of non-insulin dependent diabetes induced by neonatal streptozotocin. Diabete Metab. *15*, 61–75.

Ramesh, G., and Reeves, W.B. (2002). TNF-alpha mediates chemokine and cytokine expression and renal injury in cisplatin nephrotoxicity. J. Clin. Invest. *110*, 835–842.

Reed, A.L., Tanaka, A., Sorescu, D., Liu, H., Jeong, E.M., Sturdy, M., Walp, E.R., Dudley, S.C., Jr., and Sutliff, R.L. (2011). Diastolic dysfunction is associated with cardiac fibrosis in the senescence-accelerated mouse. Am. J. Physiol. Heart Circ. Physiol. *301*, H824–H831.

Regev, A., Teichmann, S.A., Lander, E.S., Amit, I., Benoist, C., Birney, E., Bodenmiller, B., Campbell, P.J., Carninci, P., Clatworthy, M., et al. (2017). Science Forum: the human cell Atlas. Elife *6*, https://doi.org/10.7554/eLife.27041.

Sehl, P.D., Tai, J.T., Hillan, K.J., Brown, L.A., Goddard, A., Yang, R., Jin, H., and Lowe, D.G. (2000). Application of cDNA microarrays in determining molecular phenotype in cardiac growth, development, and response to injury. Circulation *101*, 1990–1999.

Shen, Z.J., Hu, J., Shiizaki, K., Kuro-o, M., and Malter, J.S. (2016). Phosphate-induced renal fibrosis requires the prolyl isomerase pin1. PLoS One *11*, e0150093.

Shimada, T., Kakitani, M., Yamazaki, Y., Hasegawa, H., Takeuchi, Y., Fujita, T., Fukumoto, S., Tomizuka, K., and Yamashita, T. (2004). Targeted ablation of Fgf23 demonstrates an essential physiological role of FGF23 in phosphate and vitamin D metabolism. J. Clin. Invest. *113*, 561–568.

Stubbs, J.R., Liu, S., Tang, W., Zhou, J., Wang, Y., Yao, X., and Quarles, L.D. (2007). Role of hyperphosphatemia and 1,25-dihydroxyvitamin D in vascular calcification and mortality in fibroblastic growth factor 23 null mice. J. Am. Soc. Nephrol. *18*, 2116–2124.

Suyama, T., Okada, S., Ishijima, T., Iida, K., Abe, K., and Nakai, Y. (2012). High phosphorus diet-induced changes in NaPi-IIb phosphate transporter expression in the rat kidney: DNA microarray analysis. PLoS One *7*, e29483.

Takada, N., Omae, M., Sagawa, F., Chi, N.C., Endo, S., Kozawa, S., and Sato, T.N. (2017). Re-evaluating the functional landscape of the cardiovascular system during development. Biol. Open *6*, 1756–1770.

Tani, T., Orimo, H., Shimizu, A., and Tsuruoka, S. (2017). Development of a novel chronic kidney disease mouse model to evaluate the progression of hyperphosphatemia and associated mineral bone disease. Sci. Rep. *7*, 2233.

Tonne, J.M., Sakuma, T., Deeds, M.C., Munoz-Gomez, M., Barry, M.A., Kudva, Y.C., and Ikeda, Y. (2013). Global gene expression profiling of pancreatic islets in mice during streptozotocin-induced beta-cell damage and pancreatic Glp-1 gene therapy. Dis. Model. Mech. *6*, 1236–1245.

Uhlen, M., Fagerberg, L., Hallstrom, B.M., Lindskog, C., Oksvold, P., Mardinoglu, A., Sivertsson, A., Kampf, C., Sjostedt, E., Asplund, A., et al. (2015). Proteomics. Tissue-based map of the human proteome. Science *347*, 1260419.

Uliasz, A., and Lebwohl, M. (2008). Cutaneous manifestations of cardiovascular diseases. Clin. Dermatol. *26*, 243–254.

Vervloet, M.G., Adema, A.Y., Larsson, T.E., and Massy, Z.A. (2014a). The role of klotho on vascular calcification and endothelial function in chronic kidney disease. Semin. Nephrol. *34*, 578–585.

Vervloet, M.G., Massy, Z.A., Brandenburg, V.M., Mazzaferro, S., Cozzolino, M., Urena-Torres, P., Bover, J., and Goldsmith, D.; CKD-MBD Working Group of ERA-EDTA (2014b). Bone: a new endocrine organ at the heart of chronic kidney disease and mineral and bone disorders. Lancet Diabetes Endocrinol. *2*, 427–436.

Wada, N., Yamanaka, S., Shibato, J., Rakwal, R., Hirako, S., Iizuka, Y., Kim, H., Matsumoto, A., Kimura, A., Takenoya, F., et al. (2016). Behavioral and omics analyses study on potential involvement of dipeptide balenine through supplementation in diet of senescence-accelerated mouse prone 8. Genom. Data *10*, 38–50.

Watanabe, R., Fujita, N., Sato, Y., Kobayashi, T., Morita, M., Oike, T., Miyamoto, K., Kuro-o, O.M., Michigami, T., Fukumoto, S., et al. (2017). Enpp1 is an anti-aging factor that regulates Klotho under phosphate overload conditions. Sci. Rep. *7*, 7786.

Wesseling-Perry, K., and Salusky, I.B. (2013). Chronic kidney disease: mineral and bone disorder in children. Semin. Nephrol. *33*, 169–179.

ISCI, Volume *2*

Supplemental Information

The Body-wide Transcriptome

Landscape of Disease Models

Satoshi Kozawa, Ryosuke Ueda, Kyoji Urayama, Fumihiko Sagawa, Satsuki Endo, Kazuhiro Shiizaki, Hiroshi Kurosu, Glicia Maria de Almeida, Sharif M. Hasan, Kiyokazu Nakazato, Shinji Ozaki, Yoshinori Yamashita, Makoto Kuro-o, and Thomas N. Sato

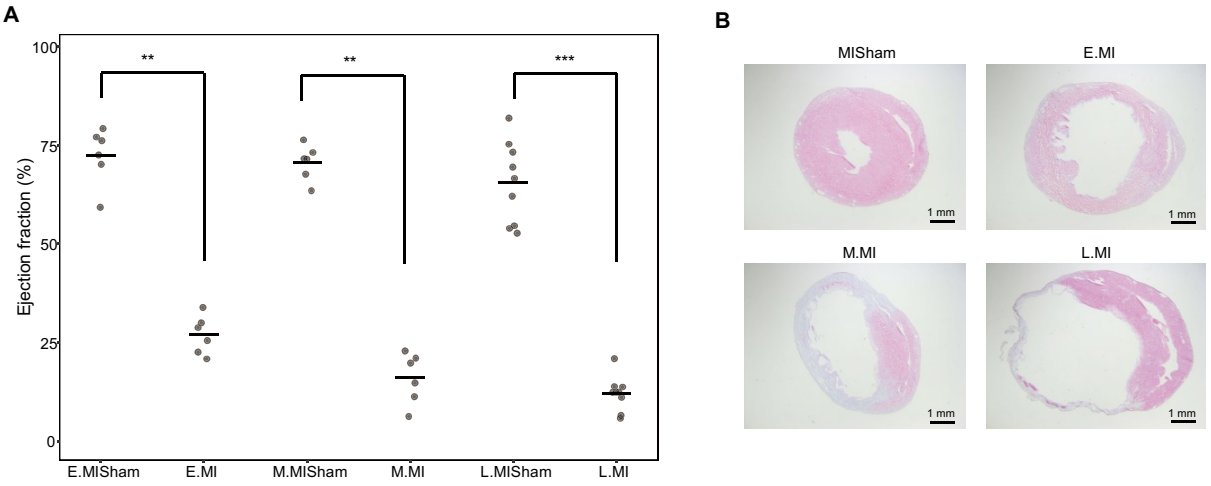

Figure S1. Characterization of the MI Models. Related to Figure 1.
(A) Ejection fraction of the MI models. n=6 (E, M), n=9 (L). ** $p < 0.01$ and *** $p < 0.001$, Mann Whitney U-test. The mean is indicated by a horizontal line. (B) Histology of the heart of sham and MI mice. Hematoxylin-eosin stained sections are shown. Scale bars, 1 mm.

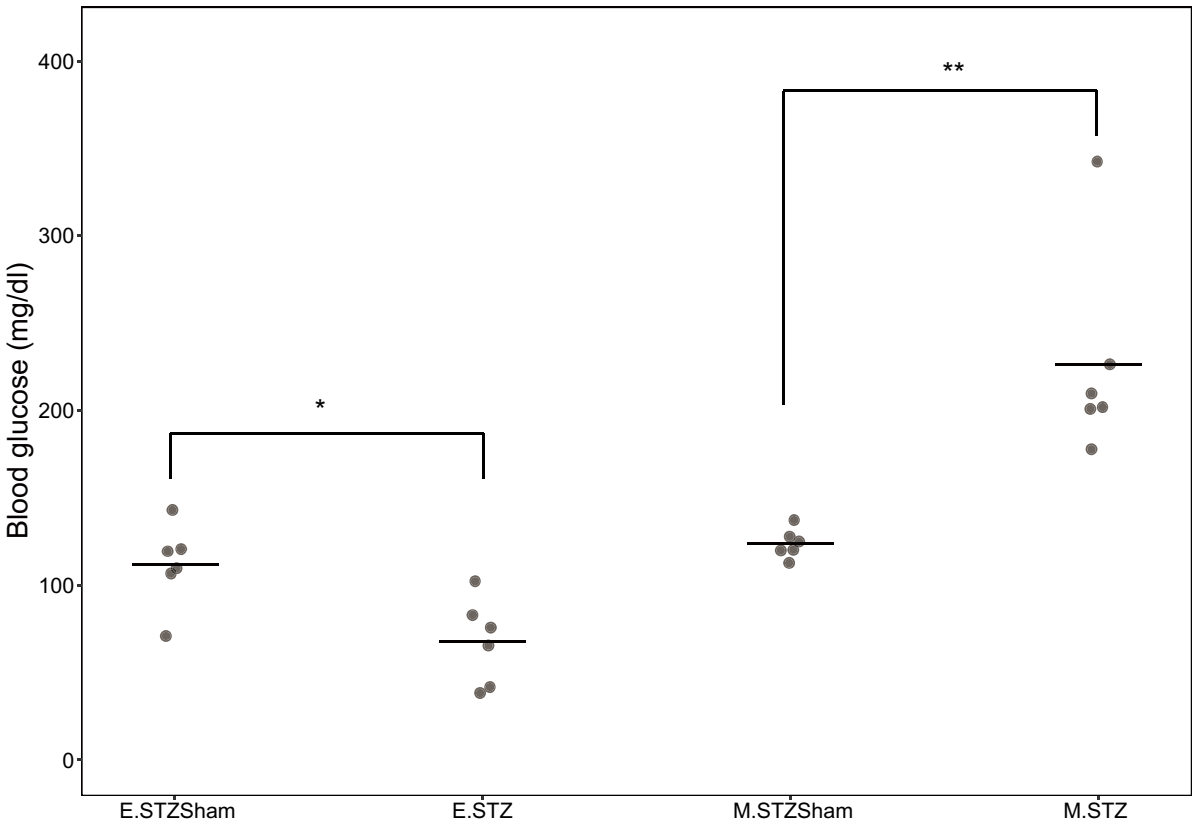

Figure S2. Blood Glucose Level in the Diabetes Model. Related to Figure 1.
The blood glucose levels for E.STZ Sham (n=6), E.STZ (n=6), M.STZ Sham (n=6) and M.STZ (n=6) models are shown in mg/dl. * $p < 0.05$ and ** $p < 0.01$, Mann Whitney U-test. The mean is indicated by a horizontal line.

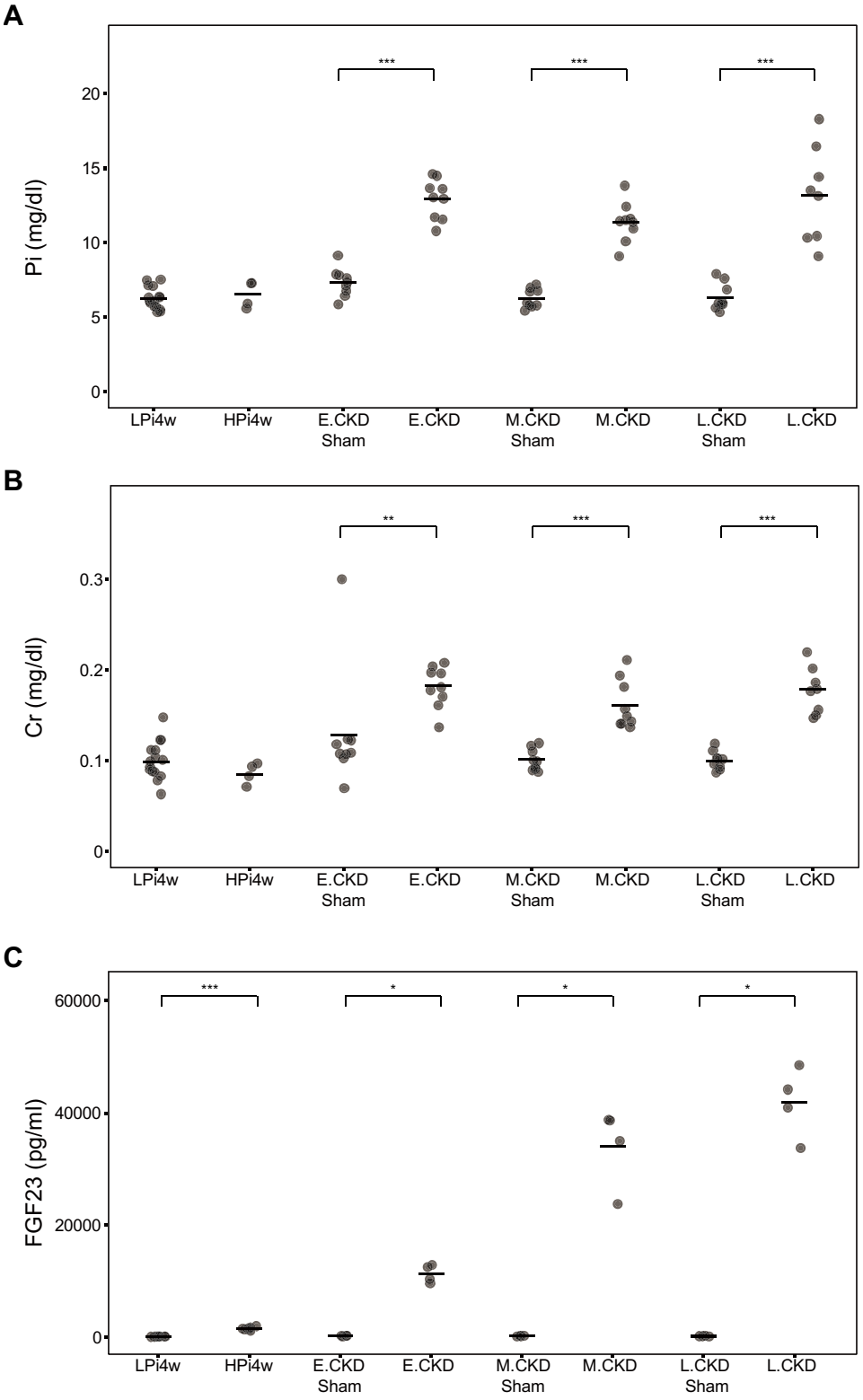

Figure S3. Blood Analyses of the CKD and CKD-Related Models. Related to Figure 1.
Blood inorganic phosphorus (Pi) (A), Creatinine (Cr) (B) and FGF23 (C) concentrations for each model are shown. n=15 (LPi4w), n=4 (HPi4w), n=9 (E.CKD Sham), n=9 (E.CKD), n=9 (M.CKD Sham), n=9 (M.CKD), n=9 (L.CKD Sham), n=8 (L.CKD) for (A) and (B). n=8 (LPi4w), n=8 (HPi4w), n=4 (E.CKD Sham), n=4 (E.CKD), n=4 (M.CKD Sham), n=4 (M.CKD), n=4 (L.CKD Sham), n=4 (L.CKD) for (C). * $p < 0.05$, ** $p < 0.01$, and *** $p < 0.001$, Mann Whitney U-test. The mean is indicated by a horizontal line.

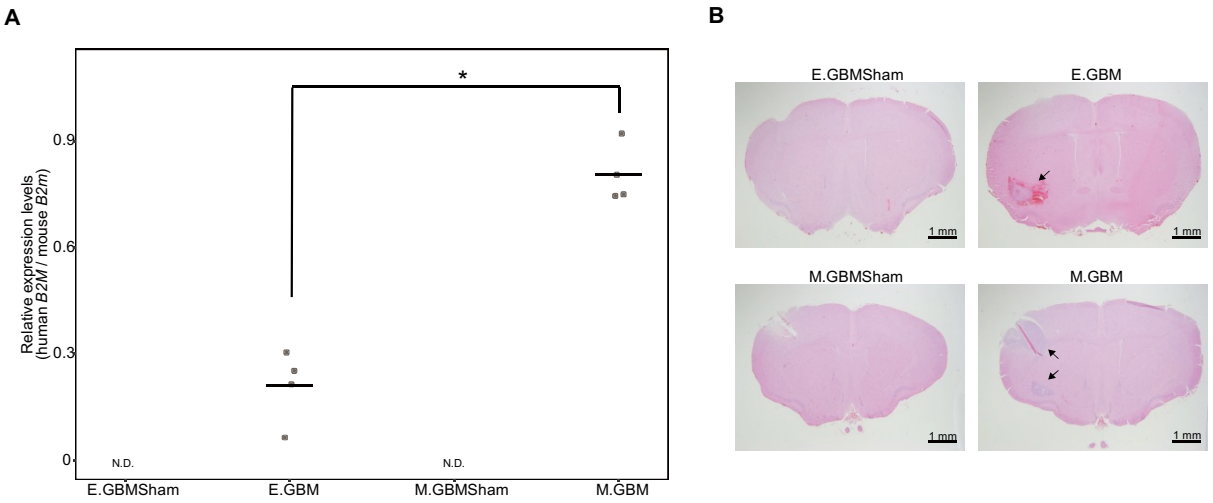

Figure S4. Characterization of the GBM Models. Related to Figure 1.
(A) qRT-PCR for human *B2M* and mouse *B2m* gene expression. n=3 (E.GBM Sham), n=4 (E.GBM), n=3 (M.GBM Sham), n=4 (M.GBM), * $p < 0.05$, Mann Whitney U-test. The mean is indicated by a horizontal line. N.D.: not detectable. (B) Histology of the tumor cell-transplanted brain sections. Hematoxylin-eosin stained sections are shown. Transplanted tumor cells are indicated by arrows. Scale bars, 1 mm.

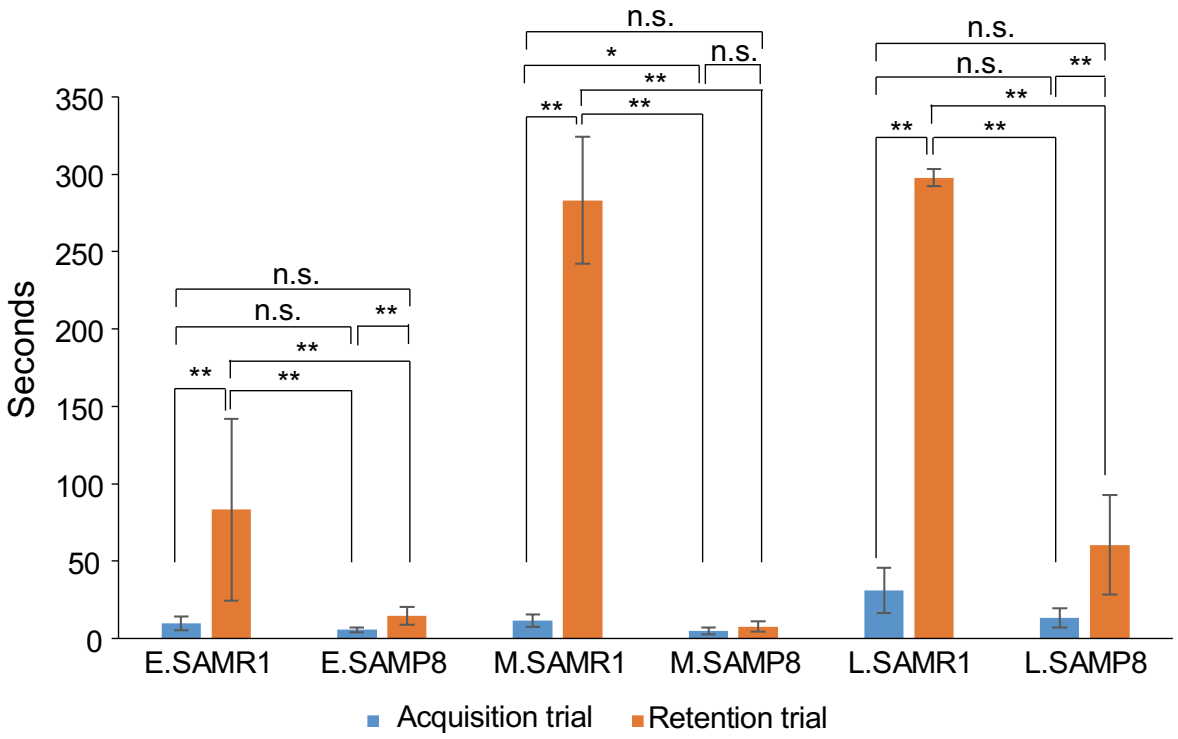

Figure S5. Behavioral Test of the SAMP8 Models. Related to Figure 1.
Step-Through test results of SAMP8 mice. The time each mouse spent in memory-acquisition trial (blue bars) and memory-retention trial (orange bars) is shown in second for control (SAMR1) and SAMP8 at each stage (E., M., L.) is shown. n=6. *p < 0.05 and **p < 0.01, Mann Whitney U-test. Bars are shown as mean±S.D. n.s.: Not significant.

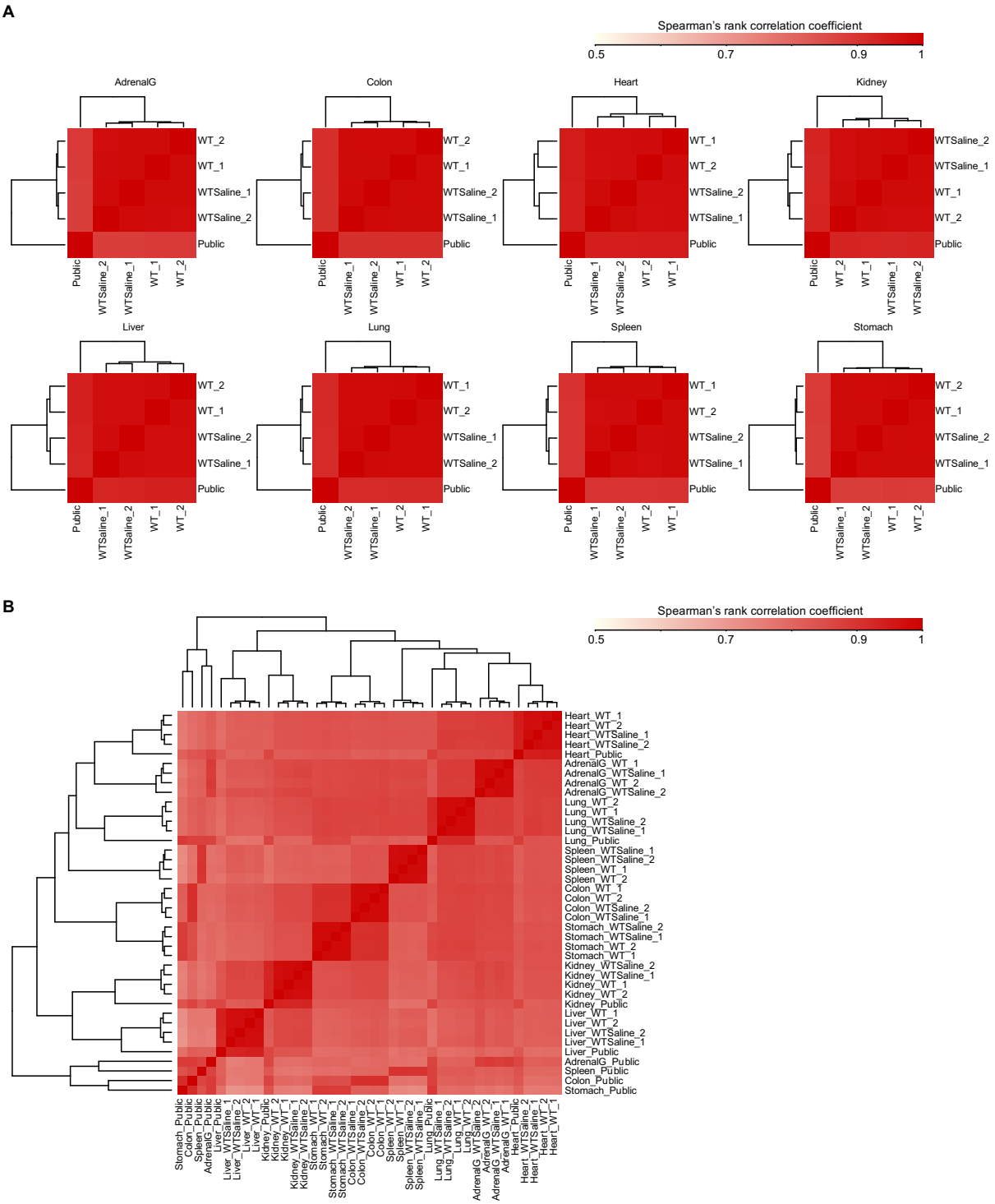

Figure S6. Comparisons of the RNAseq Datasets of the Control Mice to Publicly Available Mouse Datasets. Related to Figure 1.

The RNAseq datasets of the control mice (WT and WT+Saline) are compared to the previously published publicly available multi-organ mouse RNAseq datasets (GSE36025) (Pervouchine et al., 2015). The WT and WT+Saline are C57BL/6N Jcl male mice of 11 weeks old and 15 weeks old, respectively. The publicly available datasets are from C57BL/6J mice of 8 weeks old (the sex is unknown). The result is shown as heat-map of the Spearman's correlation coefficients for each organ (A) and for all organs (B).

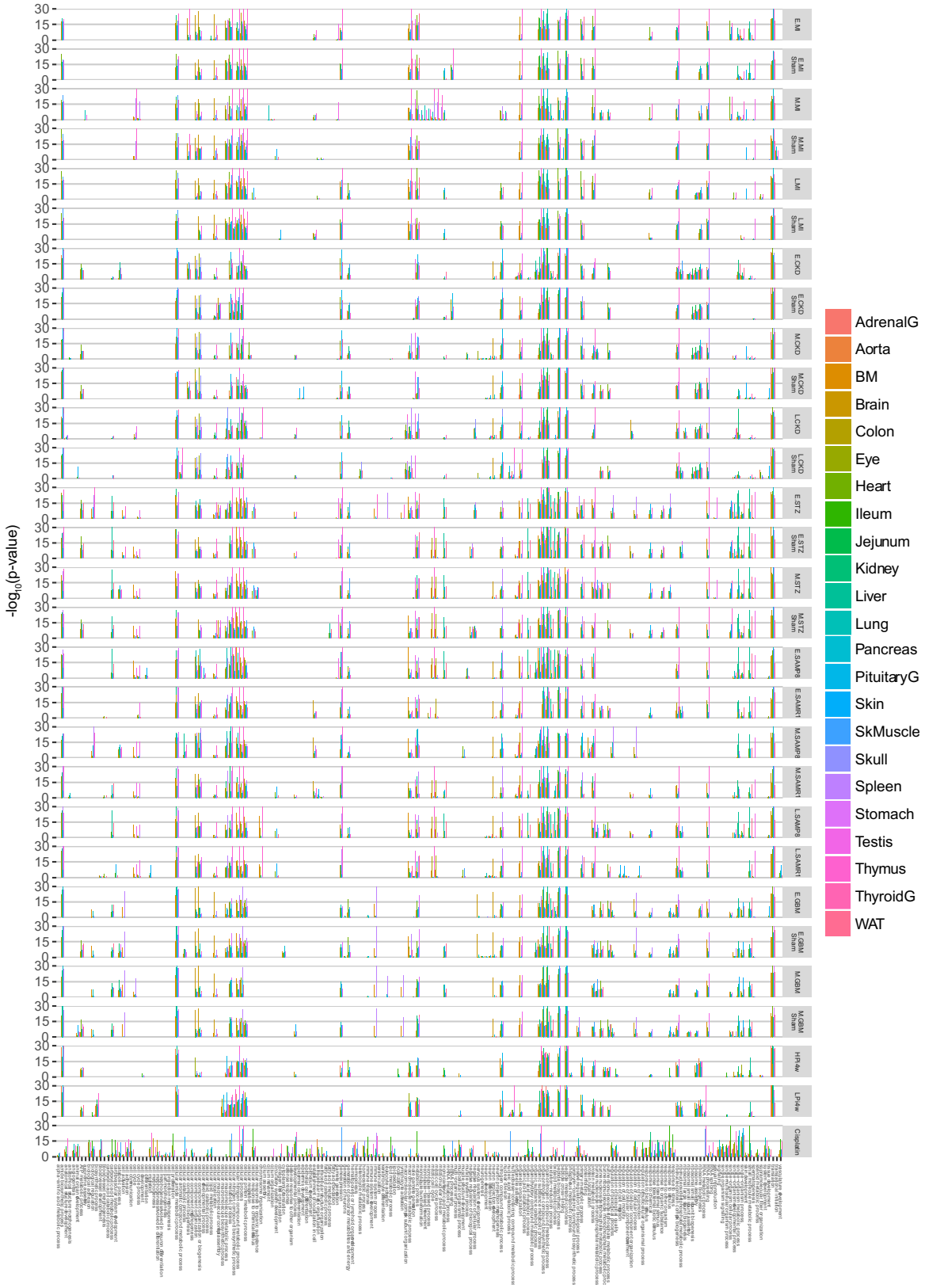

Figure S7. Organ-to-Organ Comparisons of the GO Terms of the Differentially Expressed Genes in Each Organ. Related to Figure 3.

The p-values are shown in log10 for each GO term. The top 10 GO terms in one or more of the models are shown. The complete list of the GO terms is shown in Table S13.

The p-values are shown in log10 for each GO term. The top 10 GO terms in one or more of the models are shown. The complete list of the GO terms are shown in Table S13.

Figure S8. Model-to-Model Comparisons of the GO Terms of the Differentially Expressed Genes in Each Model. Related to Figure 4.

The p-values are shown in log10 for each GO term. The top 10 GO terms in one or more of the organs are shown. The complete list of the GO terms is shown in Table S13.

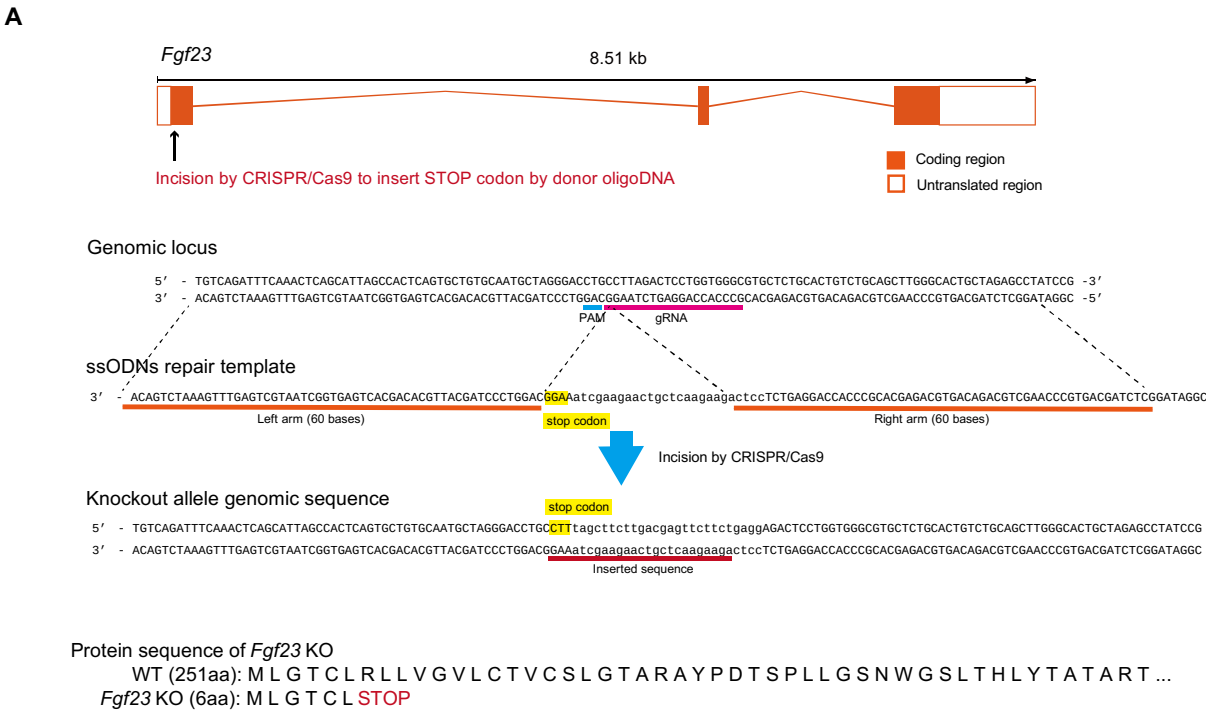

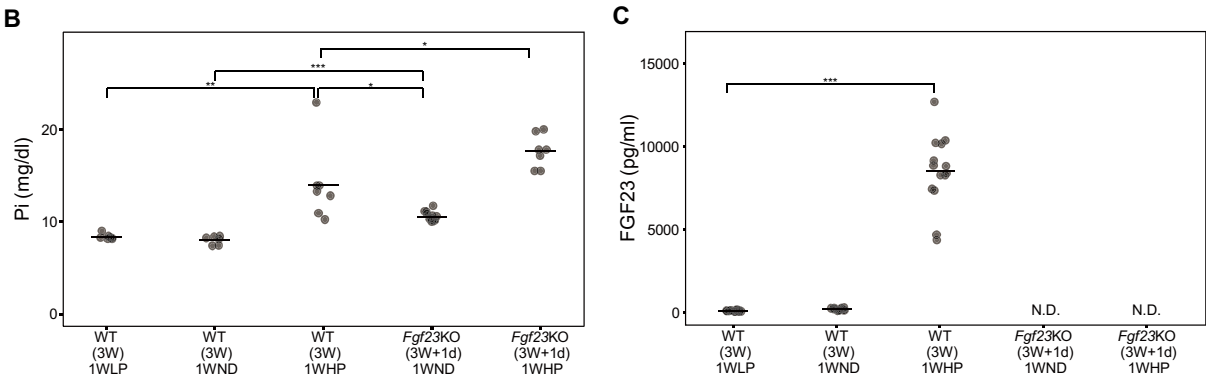

Figure S9. Generation and Characterizations of the FGF23 Mutant. Related to Figure 8.
(A) Schematic diagram describing the mutation in FGF23 gene. The sequence of the mutant FGF23 protein is described. The plasma inorganic phosphate (Pi) (B) and FGF23 (C) concentrations are shown. LP: low-phosphorus diet, ND: normal diet, HP: high-phosphorus diet. n=7 (WT1WLP), n=6 (WT1WND), n=7 (WT1WHP), n=12 (FGF23KO1WND), n=7 (FGF23KO1WHP) for Pi (B). n=14 (WT1WLP), n=12 (WT1WND), n=14 (WT1WHP), n=10 (FGF23KO1WND), n=7 (FGF23KO1WHP) for FGF23 (C). * $p < 0.05$, ** $p < 0.01$, and *** $p < 0.001$, Mann Whitney U-test. The mean is indicated by a horizontal line. N.D.: not detectable.

A

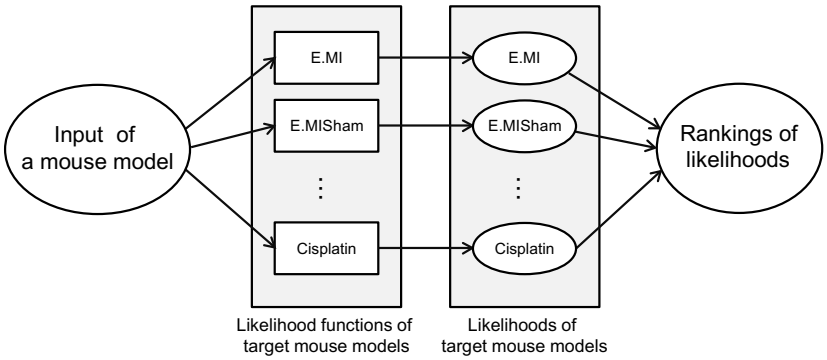

B

Input \ Target	E.MI	E.MISham	M.MI	M.MISham	L.MI	L.MISham	E.CKD	E.CKDSham	M.CKD	M.CKDSham	L.CKD	L.CKDSham	E.STZ	E.STZSham	M.STZ	M.STZSham	E.SAMP8	E.SAMR1	M.SAMP8	M.SAMR1	L.SAMP8	L.SAMR1	E.GBM	E.GBMSham	M.GBM	M.GBMSham	HPi4w	LPi4w	Cisplatin
E.MI	1	3	9	10	24	12	26	21	17	19	29	20	8	2	15	13	28	18	22	27	14	23	16	11	25	7	6	4	5
E.MISham	3	1	8	2	21	4	26	22	9	19	29	20	17	16	14	12	28	7	24	27	15	23	11	13	25	18	10	6	5
M.MI	2	4	1	7	22	10	28	24	16	20	29	18	9	14	13	17	26	19	25	27	15	21	11	5	23	12	8	6	3
M.MISham	7	2	11	1	24	5	26	22	16	20	29	19	14	3	15	18	28	12	23	27	13	21	9	8	25	17	10	6	4
L.MI	3	2	10	7	1	4	27	24	5	19	29	21	20	23	14	11	22	12	26	28	16	13	18	15	25	17	9	8	6
L.MISham	3	7	10	2	21	1	25	23	5	16	29	18	19	14	12	13	28	11	26	24	22	20	17	15	27	6	9	8	4
E.CKD	23	11	20	19	24	13	1	4	2	22	29	5	14	17	15	16	26	21	25	28	12	7	8	9	27	6	18	10	3
E.CKDSham	22	10	13	19	8	9	6	1	2	14	29	3	21	23	11	18	26	24	25	27	15	5	20	12	28	17	16	7	4
M.CKD	20	6	12	10	24	9	22	7	1	8	29	2	11	23	14	18	26	13	25	28	5	21	19	16	27	17	15	4	3
M.CKDSham	18	7	8	9	20	11	24	12	2	1	29	3	16	21	10	19	26	22	25	27	5	23	15	17	28	14	13	6	4
L.CKD	22	15	19	14	26	10	5	8	2	23	1	6	11	9	20	16	27	24	25	29	21	3	18	13	28	7	17	12	4
L.CKDSham	22	8	13	14	25	9	20	3	2	7	27	1	19	18	10	17	24	23	26	28	11	12	21	16	29	6	15	5	4
E.STZ	6	3	15	11	23	19	22	21	14	13	29	20	1	2	12	10	28	17	24	27	16	26	9	7	25	18	5	4	8
E.STZSham	5	2	11	10	24	17	23	21	16	12	29	19	8	1	14	15	28	18	25	27	13	26	9	3	22	20	4	6	7
M.STZ	11	2	9	10	22	17	23	20	14	15	29	19	16	12	1	13	26	21	24	27	7	25	8	3	28	18	4	6	5
M.STZSham	3	2	13	15	21	18	24	22	9	17	29	19	10	4	6	1	25	20	23	27	12	26	14	11	28	16	5	8	7
E.SAMP8	9	11	18	15	20	12	24	23	4	17	29	21	22	19	14	10	1	3	26	28	13	25	6	16	27	8	7	5	2
E.SAMR1	6	2	11	16	22	7	24	23	5	15	29	21	20	12	14	13	26	1	25	27	10	18	17	19	28	9	8	4	3
M.SAMP8	8	9	16	18	25	12	24	21	5	11	29	10	13	23	17	20	27	22	1	26	14	19	3	6	28	15	7	4	2
M.SAMR1	6	8	11	7	26	9	20	23	4	14	29	16	13	24	15	22	27	19	25	1	18	12	17	10	28	21	3	5	2
L.SAMP8	11	4	16	15	8	3	26	20	2	6	29	19	18	23	12	14	25	17	24	27	1	21	10	13	28	22	9	7	5
L.SAMR1	11	3	12	13	15	6	24	22	2	4	29	17	20	23	14	18	25	19	26	27	8	1	10	16	28	21	9	7	5
E.GBM	7	3	10	14	20	11	23	22	18	13	29	19	12	21	8	17	26	15	25	28	4	24	1	2	27	16	9	6	5
E.GBMSham	6	2	9	11	17	14	23	22	15	13	29	19	10	20	5	16	27	18	24	28	7	26	12	1	25	21	8	4	3
M.GBM	9	6	10	5	20	11	26	23	18	12	29	19	17	24	14	22	27	16	25	28	2	21	15	7	1	4	13	8	3
M.GBMSham	9	3	10	8	21	12	26	22	18	13	29	19	16	7	14	20	23	17	25	28	5	27	15	2	24	1	11	6	4
HPi4w	6	5	12	8	26	17	23	19	10	16	29	15	7	18	14	13	27	22	21	24	9	25	11	3	28	20	1	4	2
LPi4w	7	4	15	13	26	9	24	19	14	11	29	12	10	21	17	16	28	18	22	25	8	20	6	5	27	23	3	1	2
Cisplatin	8	4	11	14	26	16	21	20	7	6	29	18	13	22	12	17	27	24	19	15	10	25	9	5	28	23	2	3	1

Figure S10. Likelihood between a Pair of the Models. Related to Figures 10 - 16.
(A) Schematic diagram describing the likelihood analysis (see Transparent Methods for the details). (B) The likelihood map. The rankings of the likelihood are indicated. The top 5 are highlighted in light-red color.

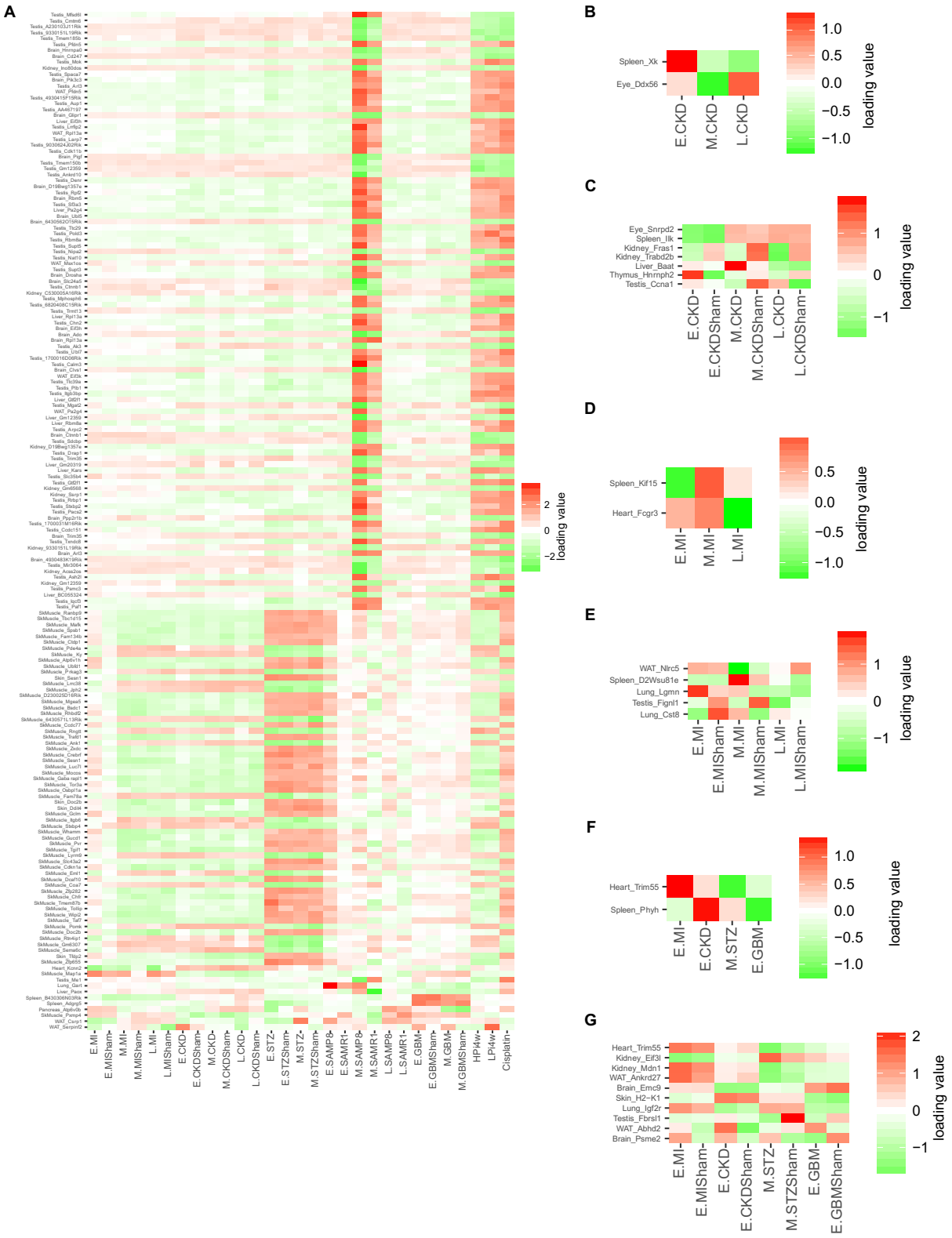

Figure S11. PLS-DA of the Datasets. Related to Figures 10 - 16.
All (A), E.CKD/M.CKD/L.CKD (B), E.CKD/E.CKD Sham/M.CKD/M.CKD Sham/L.CKD/L.CKD Sham (C), E.MI/M.MI/L.MI (D), E.MI/E.MI Sham/M.MI/M.MI Sham/L.MI/L.MI Sham (E), E.MI/E.CKD/M.STZ/E.GBM (F) and E.MI/E.MI Sham/E.CKD/E.CKD Sham/M.STZ/M.STZ Sham/E.GBM/E.GBM Sham (G) datasets are analyzed. The results are shown as heat-maps.

Transparent Methods

Animals

All animal protocols were approved by the Animal Care and Use Committee of Advanced Telecommunications Research Institute International (Approved Number: A1406, A1504, A1604, A1607, A1609, A1704, A1707, and A1709) for myocardial infarction (MI) model and phosphorus diet model, Jichi Medical University (Approved Number: 15065) for unilateral nephrectomy and high phosphorus diet (CKD) model, New Drug Research Center, Inc. (Approved Number: 150515C and 150604B) for SAMP8 and diabetes model, KAC Co., Ltd (Approved Number 15-0903) for glioblastoma multiforme (GBM) model, and Karydo TherapeutiX, Inc (Approved Number: AN20170014KTX, AN20170001KTX, AN20170010KTX) for cisplatin model, wild type mouse without any treatment, and wild type mouse treated with saline. All experiments were conducted with ICR (CD1), C57BL/6NCrSlc, SAMR1/Ta Slc, SAMP8/Ta Slc (Japan SLC, Inc., Shizuoka, Japan), C57BL/6J (Charles River Laboratories Japan, Inc., Kanagawa, Japan), C57BL/6N Jcl and NOD/ShiJic-scid Jcl (CLEA Japan, Inc., Tokyo, Japan). Control mice are wild type (WT) and wild type injected with saline (WT+Saline). WT are C57BL/6N Jcl male mice of 11 weeks old and WT+Saline are C57BL/6N Jcl male mice injected with Saline of 15 weeks old. All animals were housed in a temperature controlled room at around 25°C with 12 h light/dark cycle and allowed free access to water and normal foods (CE-2, CLEA Japan, Inc., Tokyo, Japan).

Myocardial infarction (MI models)

Male CD1 mice at 10 weeks old were used to produce myocardial infarction (MI) by ligation of left anterior descending coronary artery (LAD) (Murakoshi et al., 2013). Mice were anaesthetized by inhalation of 2 - 2.5% vaporized isoflurane (Wako Pure Chemical Industries, Ltd., Osaka, Japan) and intubated with a 20-gauge intravenous catheter. Mice were ventilated with a volume-controlled respirator (Harvard Apparatus, MA, USA) with 200 μl per cycle at a respiratory rate of 110 cycles/min. After thoracotomy, the third intercostal space was dissected to see the LAD under the stereoscope. The LAD was ligated with an 8-0 nylon suture 1-2 mm below the tip of the left auricle. Occlusion was confirmed by the change of color (pallor) of the anterior wall of the left ventricle. The chest cavity was closed with 5-0 silk sutures. The skin was closed by 9 mm autoclips. After the mice were awaken, the intravenous catheter was extubated from trachea. Sham-operated mice were produced by the same operation without ligating the suture, but passing it under the LAD. The mice were allowed to recover from the operation on a warm plate for 30 minutes. The following organs were harvested and frozen in liquid nitrogen after euthanasia at 1 day, 1 week, and 8 weeks post-surgery: Bone marrow cells (BM), the brain, the skin (from the ear), the heart, the kidney, the liver, the lung, the pancreas, the skeletal muscle (SkMuscle), the spleen, the testis, the thymus, and the gonadal white adipose tissue (WAT). These organs were stored at -80°C until further analyses.

Echocardiography

Echocardiography to assess a systolic and diastolic function was performed on MI or Sham-operated mice before the surgery and also at 1 day, 1 week, and 8 weeks post-surgery with Toshiba Diagnostic Ultrasound System Machine (Aplio MX SSA-780A, TOSHIBA Medical Systems Corporation, Tochigi, Japan) or VisualSonics Vevo2100 imaging system (FUJIFILM VisualSonics Inc., Toronto, Canada). The mice were anaesthetized with 2 - 2.5% isoflurane and parasternal long-axis 2D-mode and M-mode were recorded. The ejection fraction (EF) was calculated as follows: (Left ventricular diastolic volume – Left ventricular systolic volume) / Left ventricular diastolic volume.

Histology

Whole heart was harvested and embedded in OCT compound (Sakura Finetek Japan, Tokyo, Japan). The sample was stored at -80°C. The heart was sectioned at 5 μm thickness by cryostat. Whole brain was harvested and fixed in bouin's fixative. The brain was embedded in paraffin and sectioned at 5 μm thickness by microtome. These sections were processed for hematoxylin and eosin staining. The image of stained sections was captured with Leica M165 FC microscope (Leica, Wetzlar, Germany).

Unilateral nephrectomy and high phosphorus diet model (CKD models)

Phosphate-overload is a critical risk factor for several diseases including renal diseases such as CKD. The phosphate-overload was induced by daily feeding the unilaterally nephrectomized mice with high-phosphorous diet as follows. Male C57BL/6J mice at 8 weeks old underwent unilateral nephrectomy. They were anaesthetized by intraperitoneal (IP) injection of 1.25% Avertin (2,2,2-tribromoethylalcol) at a dose of 250 mg/kg. The right kidney was exposed by a dorsal incision, and then renal pedicle and ureter were ligated with a silk suture. After the ligation of the renal pedicle and ureter, the right kidney was dissected. The retroperitoneum incision was sutured, and the skin was closed by 9 mm autoclips. Sham-operated mice were produced by the same operation without ligating the renal pedicle and ureter and without dissecting the right kidney. After 4 weeks of the surgery, the mice were fed ad libitum with low phosphorus (LPi) diet (0.35% inorganic phosphorus) or high phosphorus (HPi) diet (2% inorganic phosphorus) for 1, 4, and 8 weeks. The composition of each diet is described in Table S25. At the end of the phosphorus diet feeding, the mice were anaesthetized with Avertin and the blood was collected from the orbital sinus into the EDTA-coated blood sampling tube. The plasma fraction was stored at -80°C. The mice were then euthanized and organs were harvested and frozen in liquid nitrogen. The adrenal gland, the aorta, the brain, the colon, the eye, the heart, the ileum, the jejunum, the kidney, the liver, the lung, the pancreas, the pituitary gland, the skin (from the back), SkMuscle, the skull (the bone), the spleen, the stomach, the testis, the thymus, the thyroid gland, and WAT were harvested. These organs were stored at -80°C for further analyses. Inorganic phosphorus and creatinine in plasma were measured by using DeterminerL IP II (Kyowa Medex, Tokyo, Japan) and L type Wako CRE M (Wako Pure Chemical Industries, Ltd., Osaka, Japan) respectively with Hitachi 7180 automatic analyzer (Hitachi, ltd., Tokyo, Japan).

Phosphorus diet model (HPi4w model)
Male C57BL/6NCrSlc mice at 8 weeks old were fed ad libitum with LPi diet (0.35% inorganic phosphorus) or HPi diet (2% inorganic phosphorus) for 4 weeks. The organs described for the CKD models and BM were harvested. The complete compositions of the diet are described in Table S25.

Phosphorus diet model (Young mouse model)
Male C57BL/6NCrSlc mice at 3 weeks old were fed LPi diet (0.35% inorganic phosphorus) or normal diet (ND: 0.54% inorganic phosphorus) or HPi diet (2% inorganic phosphorus) for 1 week. *Fgf23*$^{-/-}$ (C57BL/6NCrSlc background strain) mice at 3 weeks plus 1 day-old were fed normal diet or high phosphorus diet for 1 week. The blood and the skin were harvested as described for the CKD models.

Cisplatin model
Male C57BL/6NJcl mice at 11 weeks old received single intraperitoneal injection of cisplatin (Bristol-Myres Squibb) at 20 mg/kg dosage. Organs were harvested on the 3rd day after the injection. The organs described for the CKD models and BM were harvested.

Diabetes models (STZ models)
Male C57BL/6NCrSlc mice at 4 weeks old were administered Streptozotocin (STZ) (S01310-1G, Sigma-Aldrich, MO, USA) at a dose of 75 mg/kg weight via IP injection for 3 consecutive days. Sham-treated mice were administered 0.01 M citrate buffer (pH 4.5) for 3 consecutive days. Mice were starved overnight one day before they were sacrificed. On day 1 and day 7 after the last STZ administration, organs were harvested and frozen in liquid nitrogen. BM, the brain, the colon, the skin (from the ear), the heart, the kidney, the liver, the lung, the pancreas, SkMuscle, the spleen, the stomach, the testis, the thymus, and WAT were harvested from each mouse. These organs were stored at -80°C for further analyses. The blood glucose level was measured by bleeding the tail vein and using Life Check/Life Check sensor (GUNZE LIMITED, Osaka, Japan).

Human tumor xenograft model (GBM models)
Human glioblastoma multiform cell line, U-87MG (ECACC 89081402), was purchased from DS Pharma biomedical Co. Ltd (Osaka, Japan). The cells were cultured with E-MEM containing 10% fetal bovine serum, 1% non-essential amino acids, and 1 mM Sodium pyruvate at 37°C under 5% CO_2. The cell suspension at 1 x 10^8 cells/ml in PBS was prepared for implantation into right cerebral hemisphere. Male NOD/ShiJic-scid Jcl mice at 7 weeks old were used for the xenograft. The mice were

anaesthetized by a mixture of medetomidine (0.3 mg/kg, Nippon Zenyaku Kogyo Co., Ltd., Fukushima, Japan), midazolam (4.0 mg/kg, Astellas Pharma Inc., Tokyo, Japan), and butorphanol (5.0 mg/kg, Meiji Seika Pharma Co., Ltd., Tokyo, Japan) by IP injection. The anaesthetized mouse's head was fixed with a standard stereotaxic instrument (Cat No: 68012, RWD Life Science Inc., CA, USA), and the scalp was incised to expose the skull. A small hole was made on the skull with a dental drill to implant 2 μl of the cell suspension into the right brain with micro-syringe (Cat No. 80300, Hamilton Company, NV, USA). The implanted place was fixed at the anterior of 0.1 mm and right side of 2.2 mm from Bregma, and 3 mm depth of dura mater. After the cell suspension was injected at speed of 1 μl/min, the incision on scalp was sutured with a nylon suture. The implanted mouse was awaken by IP injection of atipamezole (0.3 mg/kg, Nippon Zenyaku Kogyo Co., Ltd., Fukushima, Japan). Sham-operated mice were produced by the same operation with PBS injection instead of the cell suspension. On the 3rd and 7th days post-surgery, the mice were starved for overnight prior to harvesting the organs. BM, the brain, the colon, the skin (from the ear), the heart, the kidney, the liver, the lung, the pancreas, SkMuscle, the spleen, the stomach, the testis, and WAT were harvested. These organs were stored at -80°C for further analyses. Successful xenograft of U-87MG cells was confirmed by qRT-PCR for human *B2M* mRNA detection in mouse right brain.

SAMP8 model and Step-through test

SAMP8 mice are a genetically established line from a mouse that spontaneously produced amyloid precursor protein and demonstrated oxidative damage in the brain (Butterfield and Poon, 2005). SAMR1 mice, a substrain without such phenotypes, were used as controls. Male SAMR1/Ta Slc mice (control mice for SAMP8) and SAMP8/Ta Slc mice at 8, 16, and 32 weeks old were sacrificed to harvest the organs. The sacrificed mice at 8, 16, and 32 weeks old were selected based on the result of the Step-Through test as follows. Manual Step-Through Test System (Muromachi Kikai Co., Ltd., Tokyo, Japan) was used to test animals' memory retention. The test cage was divided into the two compartments, the light and the dark by the guillotine door. First, a mouse was placed in the light compartment and allowed to explore there for 10 seconds so that the mouse may become familiarized with the environment. Then the door was opened and the mouse tried to get into the dark room since mice prefers a dark place. As soon as the mouse got into the dark, the door was closed without any shock as an adaptation trial. The mouse was kept for 10 seconds in the dark room. Second, in the case of an acquisition trail, the mouse was kept for 10 seconds in the light room, and then the door was opened. The migration time from the light to the dark room was recorded (maximum 300 seconds). As soon as the mouse got into the dark room, an electrical shock (0.2 mA, 3 seconds, once) was given to the mouse in the dark room. If the mouse did not get into the dark room in 300 seconds, the mouse was moved to the dark room by force and the same electrical shock was given to the mouse once. For memory retention test, the trained mouse (through adaptation and acquisition trials) was kept in the light room for 10 seconds, and then the door was opened. The migration time from the light to the dark room was recorded (maximum 300 seconds). SAMP8 mice exhibit shorter memory retention time as compared to the SAMR1 control mice. The SAMP8 mice confirmed for this typical memory-loss phenotype and the SAMR1 control mice at 8, 16, and 32 weeks old were euthanized and the organs were harvested and frozen in liquid nitrogen. BM, the brain, the colon, the skin (from the ear), the heart, the kidney, the liver, the lung, the pancreas, SkMuscle, the spleen, the stomach, the testis, the thymus, and WAT were harvested. The organs were stored at -80°C for further analyses.

Human biopsies

The skin tissue biopsies from 8 breast cancer and 3 lung cancer patients were collected at Kure Medical Center and Chugoku Cancer Center. The information of each patient is available at Table S26. All the patients were negative for HIV, HBV, HCV, HTLV-1, and Syphilis. They had no chemotherapy or radiation therapy treatments prior to the surgery. This study was approved by the independent ethics committee of Kure Medical Center and Chugoku Cancer Center (Approved Number: 27-37) and Advanced Telecommunications Research Institute International (Approved Number: H1501-1602). The detailed information of the subjects is described in Table S26. The human skin RNAseq data from The Human Protein Atlas (https://www.proteinatlas.org) were analyzed as healthy subject controls.

RNAseq and bioinformatics analyses

The RNA purity and integrity were determined by Agilent 2100 Bioanalyzer (Agilent, CA, USA) for total RNA from each organ. RNAseq analyses were performed with either Illumina HiSeq 1500 or 2000 or 2500 or 4000. The details of RNAseq analyses are shown in Table S27. The output data were analyzed by Galaxy (https://usegalaxy.org/). All sequences were mapped on mouse genome (mm10) or human genome (hg19) with Bowtie2 (Langmead et al., 2009). Mapped sequences were calculated as reads per kilobase of exon per million mapped reads (RPKM) or fragments per kilobase of exon per million mapped reads (FPKM) by Cufflinks (Trapnell et al., 2010).

Analyses of differentially expressed genes

To identify differentially expressed genes, the numbers of annotated reads were counted for each transcript by using HTSeq-count version 1.6.0 (with parameters -r pos and -s no) using mapped sequence data with Bowtie2. DESeq2 (Love et al., 2014) analyses version 1.17.33 with the default parameters were performed. E/M/L-MI and the corresponding Sham-controls (each n=2), E/M/L-CKD and the corresponding Sham/LPi controls (each n=3 mixed equally), E/M-STZ (each n=3 mixed equally), E/M-GBM and the corresponding Sham controls (each n=3 mixed equally), E/M/L-SAMP8 and the corresponding SAMR1 controls (each n=3 mixed equally), Cisplatin-treated (n=2) models were each compared to C57BL/6N Jcl wild type male controls (11 weeks old, n=2). Human skin biopsies from breast cancer (n=8) and lung cancer (n=3) were individually compared to each healthy human skin RNAseq dataset (n=6) at The Human Protein Atlas (https://www.proteinatlas.org). Gene ontology (GO) enrichment analysis was performed using R package "topGO" version 2.30.0. In the GO analyses, differentially expressed genes were defined as the p-value (calculated by Wald test and adjusted by Benjamini & Hochberg method) is less than 0.0001 in DESeq2 results.

Weighted gene co-expression network analysis (WGCNA)

Weighted gene co-expression network analysis was performed with R package "WGCNA" (Langfelder and Horvath, 2008). To construct weighted gene co-expression network, $\log_2$(fold-change) in DESeq2 results of each mouse model compared to C57BL/6N Jcl wild type male controls (11 weeks old, n=2) or C57BL6/N Jcl wild type male treated with saline (15 weeks old, n=2) were used. As the volume of the data is too large for calculations, we used those of which the adjusted p-values by Wald test and Benjamini & Hochberg method is less than 0.0001 at least in one model in each analysis. For example, in the analysis shown in Figure 5A, the genes of which adjusted p-values (as determined by DESeq2) are less than 0.0001 at least in one of the skin samples of E.Sham, E.MI, M.Sham, M.MI, L.Sham and L.MI. The soft thresholding power was determined with the R function "pickSoftThreshold". The relatedness of each mouse model and modules detected from the constructed network was determined by the Pearson's correlation coefficients between summary profiles (named eigengene) in detected modules and 1-of-K representation in each mouse model. The GO enrichment analyses were conducted for each module using R package "topGO" version 2.30.0.

Human-mouse comparisons

To quantify similarities and dissimilarities of RNAseq between our mouse models and published healthy humans for each organ, Spearman's correlation coefficients were calculated from combinations of FPKMs in the mouse models and healthy humans. RNAseq data from The Human Protein Atlas (https://www.proteinatlas.org) were used to compute the FPKMs for the healthy human data. HCOP (https://www.genename.org/cgi-bin/hcop) was used for assigning human-mouse orthologs. The Spearman's correlation calculations were performed by R function "cor(method="s", use="p")". Heat map visualizations of the Spearman's correlation coefficients were performed by using R function "heatmap.2" with default parameters. The comparison of the mouse MI model heart to the human heart of a heart failure patient with ischemic heart disease is conducted using the previously published publicly available RNAseq datasets (GSE57344) (Liu et al., 2015). The human heart datasets (n=3 of the non-failing heart control and n=1 heart failure with ischemic heart disease) were analyzed by DESeq2 and identified the differentially expressed genes as defined by the adjusted p-values < 0.0001 (calculated by Wald test and adjusted by Benjamini & Hochberg method). These human genes are analyzed using R package "topGO" version 2.30.0. The modules of the heart datasets of the MI-models were identified by WGCNA. Genes in each module were subjected to GO enrichment analysis using R package "topGO" version 2.30.0.

Partial least squares discriminant analysis (PLS-DA)
Partial least squares discriminant analysis was performed with R function "splsda" in the package "mixOmics" (Kim-Anh Le Cao, Florian Rohart, Ignacio Gonzalez, Sebastien Dejean with key contributors Benoit Gautier, Francois Bartolo, contributions from Pierre Monget, Jeff Coquery, FangZou Yao and Benoit Liquet. (2017). mixOmics: Omics Data Integration Project. R package version 6.3.0. https://CRAN.R-project.org/package=mixOmics) The input data of "splsda" are $\log_2$(fold-change) in DESeq2 results of mouse model compared to C57BL6/N Jcl wild type male controls (11 weeks old, n=2) or C57BL6/N Jcl wild type male treated with saline (15 weeks old, n=2), and the parameters of "splsda" were determined by using the R function "tune.splsda".

Likelihood computation
The relatedness of the body-wide transcriptome landscapes among mouse models was determined by computing likelihood function using the Spearman's correlation coefficients between all possible organ pairs. The DESeq2 analyses were performed for each organ in each model against the same organ in C57BL6/N Jcl wild type male controls (11 weeks old, n=2) or C57BL6/N Jcl wild type male treated with saline (15 weeks old, n=2). In computing the likelihood, we let i and j be indices of organs (e.g., the brain, the heart, the kidney, etc.), n be index of mouse models (E-MI, M-MI, M-STZ, etc.) and s_{nij} is a Spearman's correlation coefficient between organ i and organ j in a mouse model n, the likelihood function of organ-pair i and j in a mouse model m $L_{mij}(s_{nij})$ can be described as:

$$L_{mij}(s_{nij}) = \frac{1}{\sqrt{2\pi\sigma_{mij}^2}} \exp\left\{-\frac{(s_{nij}-\mu_{mij})^2}{2\sigma_{mij}^2}\right\},$$

where μ_{mij} and σ_{mij}^2 are sample average and variance of the Spearman's correlation coefficients between organ i and organ j in mouse model m, respectively. The body-wide (i.e. all organs) likelihood function in a mouse model m was computed as $L_m(s_n) = \prod_{i,j} L_{mij}(s_{nij})$, assuming statistical independent of Spearman's correlation coefficients among all organ pairs.

RNA extraction, cDNA synthesis, and quantitative RT-PCR (qRT-PCR)
A frozen organ was homogenized in TRIzol reagent (Thermo Fisher Scientific, MA, USA) with PT10-35 GT Polytron homogenizer (KINEMATICA, Luzern, Switzerland) at 15,000 rpm for 10 seconds or Cell Destroyer PS1000 or PS2000 (Bio Medical Science Inc., Tokyo, Japan) using mixture of different sizes of zirconia beads (1.5 mm diameter X 50, 3 mm diameter X 5, 5 mm diameter X 2) at 4,260 rpm for 45 seconds at 4°C. After 5 minutes incubation of the homogenate at room temperature, 0.2 ml of chloroform was added into 1 ml of the homogenate. The sample was vortexed for 15 seconds and incubated at room temperature for 3 minutes. The sample was centrifuged at 12,000 g for 15 minutes at 4°C. Following the centrifugation, the aqueous phase was transferred into a new tube. Equal amount of 70% EtOH was added into the sample and mixed. The sample was loaded on the RNeasy mini column (Qiagen, Venlo, Netherlands) to purify the RNA according to the manufacture's instruction. RNA purity and concentration were measured with Nanodrop 2000 (Thermo Fisher Scientific, MA, USA). cDNAs were synthesized from 1 μg of total RNA using SuperScript III first-strand synthesis system (Thermo Fisher Scientific, MA, USA) according to the manufacture's instruction. The synthesized cDNA was diluted 20 times and used for real-time PCR. Real-time qRT-PCR was performed using LightCycler480 System II and SYBR Green Master Mix (Roche, Basel, Switzerland). All primer sequences were designed with Primer-BLAST and listed in Table S28. The normalized data with reference gene gene (*Maea* for skin genes and mouse *B2m* for human *B2M*) were analyzed using delta-Ct method.

Generation of FGF23 mutant mouse by CRISPR/Cas9 method
Fgf23 (NCBI Gene ID: 64654) mutant mouse was generated by CRISPR/Cas9 system (Sander and Joung, 2014). gRNA sequences for an exon 1 of *Fgf23* gene were designed using Optimized CRISPR design tool (http://crispr.mit.edu/). The gRNAs were individually cloned into the pX330 vector (#42230, Addgene, MA, USA) that expresses Cas9 transgene. The most effective gRNA was selected as described (Mashiko et al., 2013). The sequence of selected gRNA for *Fgf23* is as follows;

GCACGCCCACCAGGAGTCTA. The plasmid including *Fgf23*-gRNA and the single-stranded oligodeoxynuleotides (ssODNs) to insert stop codon after Cas9 incision were co-injected into the pronuclei of the fertilized eggs from C57BL/6NCrSlc mice. The sequence of *Fgf23* stop donor ssODNs is as follows; CGGATAGGCTCTAGCAGTGCCCAAGCTGCAGACAGTGCAGAGCACGCCCACCAGG AGTCTcctcagaagaactcgtcaagaagctaAAGGCAGGTCCCTAGCATTGCACAGCACTGAGT GGCTAATGCTGAGTTTGAAATCTGACA. The injected eggs were transferred into the oviduct of pseudopregnant ICR female mice. The F_0 mice were genotyped by PCR and direct sequence analyses (see Table S28 for the primer sequences). One F_1 mouse line for *Fgf23* mutant was generated by inbreeding of the obtained F_0 mice with C57BL/6NCrSlc mice. F_2 and F_3 mice were generated by *in vitro* fertilization. F_3 and later generation mice were used for further analyses. These genotypes were confirmed by PCR or direct sequence analyses using primers listed in Table S28.

ELISA for FGF23

FGF23 in plasma was measured using FGF-23 ELISA Kit (TCY4000, KAINOS Laboratories, Inc., Tokyo, Japan) according to the manufacture's instruction. In each well, added were 50 μl of assay diluent and 50 μl of FGF23 standards or samples. The plate was incubated at room temperature for 2 hours, and then the plate was washed 4 times with wash buffer. After the washing, 100 μl of enzyme conjugated anti-FGF23 was added into each well. The plate was incubated at room temperature for 1 hour, and then the plate was washed 4 times with wash buffer. After the washing, 100 μl of the substrate was added into each well. The plate was incubated at room temperature for 30 minutes in dark. The reaction was stopped by adding the 100 μl of stop solution into each well. The amount of FGF23 was calculated by measuring the absorbance at 450 nm using Multiskan GO microplate reader (Thermo Fisher Scientific, MA, USA).

Statistical analyses

Mann Whitney U-test was performed. The p-values are shown as * $p < 0.05$, ** $p < 0.01$, and *** $p < 0.001$. The mean is indicated by a horizontal line. The p-values for DESeq2 were calculated by Wald test and were adjusted by the Benjamini & Hochberg method. The p-values for the correlations of WGCNA were calculated by Student's asymptotic t-test. The p-values for GO enrichment analysis were performed by Fisher's exact test.

Data availability statement

All RNAseq data reported herein are available at i-organs.atr.jp.

Supplemental References

Butterfield, D.A., and Poon, H.F. (2005). The senescence-accelerated prone mouse (SAMP8): a model of age-related cognitive decline with relevance to alterations of the gene expression and protein abnormalities in Alzheimer's disease. Experimental gerontology *40*, 774-783.

Langfelder, P., and Horvath, S. (2008). WGCNA: an R package for weighted correlation network analysis. BMC bioinformatics *9*, 559.

Langmead, B., Trapnell, C., Pop, M., and Salzberg, S.L. (2009). Ultrafast and memory-efficient alignment of short DNA sequences to the human genome. Genome biology *10*, R25.

Liu, Y., Morley, M., Brandimarto, J., Hannenhalli, S., Hu, Y., Ashley, E.A., Tang, W.H., Moravec, C.S., Margulies, K.B., Cappola, T.P., *et al.* (2015). RNA-Seq identifies novel myocardial gene expression signatures of heart failure. Genomics *105*, 83-89.

Love, M.I., Huber, W., and Anders, S. (2014). Moderated estimation of fold change and dispersion for RNA-seq data with DESeq2. Genome biology *15*, 550.

Mashiko, D., Fujihara, Y., Satouh, Y., Miyata, H., Isotani, A., and Ikawa, M. (2013). Generation of mutant mice by pronuclear injection of circular plasmid expressing Cas9 and single guided RNA. Scientific reports *3*, 3355.

Murakoshi, M., Saiki, K., Urayama, K., and Sato, T.N. (2013). An anthelmintic drug, pyrvinium pamoate, thwarts fibrosis and ameliorates myocardial contractile dysfunction in a mouse model of myocardial infarction. PloS one *8*, e79374.

Pervouchine, D.D., Djebali, S., Breschi, A., Davis, C.A., Barja, P.P., Dobin, A., Tanzer, A., Lagarde, J., Zaleski, C., See, L.H., *et al.* (2015). Enhanced transcriptome maps from multiple mouse tissues reveal evolutionary constraint in gene expression. Nat Commun *6*, 5903.

Sander, J.D., and Joung, J.K. (2014). CRISPR-Cas systems for editing, regulating and targeting genomes. Nature biotechnology *32*, 347-355.

Trapnell, C., Williams, B.A., Pertea, G., Mortazavi, A., Kwan, G., van Baren, M.J., Salzberg, S.L., Wold, B.J., and Pachter, L. (2010). Transcript assembly and quantification by RNA-Seq reveals unannotated transcripts and isoform switching during cell differentiation. Nature biotechnology *28*, 511-515.